Self Assembly in Gel Systems

by

Azaima Razali

Department of Physics
University of Bristol

A dissertation submitted to the University of Bristol in accordance with the requirements of the degree of Doctor of Philosophy in the Faculty of Science.

September 2017

Word count: 28366

Abstract

In this work we have studied the structural evolution of colloid polymer system reaching equilibrium ordered states. Throughout the work in this thesis, confocal microscopy was primarily used to capture the local structural changes. We employed the depletion mechanism from the addition of nonadsorbing polymer to colloidal dispersion in order to obtain short ranged attractive systems. The changes of local structures towards crystallisation in the colloid polymer systems are analysed using topological cluster classification (TCC), common neighbour analysis (CNA) and bond order parameter ψ_6.

Initial work studies the ageing of gels with different interaction strengths in experiment and simulation. Structural analysis of the gels shows significant similarity between experiment and simulation. In both, we find crystallisation in gels with intermediate interaction strength and formation of five-fold symmetry clusters in gels with higher interaction strengths.

Then we examine the effects of confinement to the sedimentation of colloids and gels. We find that gelation enhances sedimentation of colloids whereas there is no sedimentation in a same system without polymer. The structural analysis of the simulation results show that the local structural changes is not related to sedimentation.

By manipulating the polymer response to temperature, we change the interaction strength in the colloid polymer system in order to obtain better crystallisation. This work is based on the idea from simulation work [1], where tuning the interaction strengths during self assembly leads to better and larger ordered structures. However, contrary to the simulation results, we find that tuning the interaction strengths result to disruption to the crystallisation pathway thus more disordered structures is formed.

Acknowledgements

Alhamdulillahi robbil 'alamin.
Deepest gratitude is owed to my family for their encouragement and support over the years. I would like to thank my supervisor Paddy Royall for his support in this work. I would also like to express appreciation to Christopher Fullerton and Rob Jack for the collaboration work. For the help and advice in the lab and results analysis thanks are owed to Rattachai Pinchaipat, Francesco Turci, James Hallett and Peter Crowther. Last but not least, I am grateful to all the members of the Royall group for their intellectual and moral support.

Author's declaration

I declare that the work in this dissertation was carried out in accordance with the requirements of the University's Regulations and Code of Practice for Research Degree Programmes and that it has not been submitted for any other academic award. Except where indicated by specific reference in the text, the work is the candidate's own work. Work done in collaboration with, or with the assistance of, others, is indicated as such. Any views expressed in the dissertation are those of the author.

SIGNED: ..... DATE: .....

Publications

A. Razali, C. J. Fullerton, F. Turci, J. Hallet, R. L. Jack, and C. P. Royall, "Effects of vertical confinement on gelation and sedimentation of colloids," *Soft Matter*, vol. 13, pp. 3230–3239, 2017

Table of Contents

List of Tables

List of Figures

CHAPTER 1

Introduction

The work described in this thesis explores the structural evolution of non-equilibrium systems: colloid-polymer mixtures, in reaching equilibrium states. In particular, this work focuses on local structures that frustrate the system from reaching equilibrium ordered state and also local structures that represent the equilibrium crystalline arrangements. This chapter introduces the prerequisites for considering this work. First a general introduction to colloidal systems is given, followed by a brief discussion regarding colloid-polymer systems. Then, an introduction to self-assembly process which is the progress of achieving equilibrium ordered state is given. Finally, a thesis outline containing chapters exploring the key points discussed is given.

1.1 Colloids as Model Systems

The study done by Pusey and van Megen in 1986 [3] concluded that suspensions of colloidal particles are similar to simple atomic liquids and solids in terms of interaction due to their rich phase behaviour. Much work has been carried out to study a large number of problems in condensed matter area using colloidal systems as models. Similar to the simple atomic systems the phase behaviour of colloidal particles is determined by the interaction between the particles. Colloidal particles also undergo phase transition: gas, liquid and crystal states, as was observed in the phase diagram of argon atoms. Linked by these similarities, colloids have often been used as atomic model and have been given the term “designer atoms” [4]. Additionally, the size of the colloidal particles are generally larger ($\sim 1\mu$m) than the

size of atoms (which are usually several Å). This factor renders the diffusion of the particles slower; making it possible for observation using modern microscopes. The confocal microscope, for example, developed by Minsky [5] is able to produce crisp and high resolution images in 3-dimensions (3d). Using confocal microscopy, 3d optical sectioning of colloidal suspension samples in order to investigate, reconstruct and compute their structures and dynamics is made possible. For this reason, confocal microcopy has been extensively used for real-time observation of the structures and dynamics of colloidal suspensions [6–9].

The use of colloids as models to study the self-assembly process is advantageous due to the analogy interactions models of their interaction and behaviour with the atomic model has been established [3]. Not only the size range of colloidal particles in the magnitude order of microns is larger than atomic particles, moreover, advanced computational tools have been developed in defining the structures and dynamics of colloidal particles from confocal images. For example, the development of the topological cluster classification (TCC) in identifying the local structures of colloidal suspensions [10–12].

Colloidal systems are well-understood model systems where the interactions between the particles can be controlled by the solvent properties, characteristics and concentration of polymers or salts added. All of these factors allow the manipulation of strength and range interactions in the colloidal suspensions [13, 14]. For example, the addition of polymer to a colloidal system induces attraction in the colloidal system via the depletion mechanism. The magnitude and the range of the attraction is controlled by the size and the concentration of the polymer added. In this work, we rely on this depletion attractive interactions and a brief introduction of the mechanism is given in the next section. Extensive details regarding the model colloid system used throughout this work is given in the next chapters.

1.1.1 Colloid-polymer system

The addition of polymer induces aggregation in colloidal dispersion by creating attractive interaction potential between the colloids. Otherwise, the colloid-colloid interactions are only described by the hard sphere potentials. The colloid-polymer mixture can be considered as one component system where the effective interaction is mediated by the polymer as first proposed by Asakura and Oosawa [15, 16] and later by Vrij [17]. The addition of polymer with low molecular weight leads to the small size ratio between polymer and colloid and resulting to the broadening fluid-crystal coexistence domain [18] of the phase diagram. Also, the polymer addition leads to dynamically arrested networks that appear to be “incompletely equilibrated solid” [18–20]: gels.

The addition of polymer to colloidal suspensions will not only change the viscosity slightly but will also cause the colloidal particles to aggregate at low volume fraction, ϕ [8, 21–23] forming a gel. The arrested behaviour in gels due to the addition of polymer is analogous to quenching colloidal suspensions to low temperature. The most significant characteristic of these quenched colloidal suspensions is their slow relaxation dynamics. This allows the suspension to display wide-range of glassy dynamics effects such as ageing, nonlinear responses, plus spatial and temporal dynamic heterogeneities. These effects were achieved by moving slowly in a complex energy landscape but never reaching the global equilibrium configurations [24].

The short ranged systems with attractive interactions are gaining considerable interest due to the numerous applications such as in determining the structures of proteins [25–27], prolonging the shelf-life for commercial products [28, 29] and suspending agents in drug delivery [30]. Also, understanding gel behaviour is useful in the view of statistical mechanics as well as for industrial applications [31]. It is crucial to note that the term "gels" used in this work refers to physical gels that have reversible bonding unlike chemical gels which made of irreversible covalent bonding. Phase behaviour studies that were not previously feasible in colloidal system due to the purely repulsive interactions in such systems is made possible using colloid-polymer systems. For example, the liquid-gas phase separation [32, 33]. Other phase behaviours that were not observed in the atomic systems such as gelation and glass dynamics at high density [34] are present in this system. The phase diagrams of this model colloid-polymer systems have been investigated systematically and extensively in terms of polymer concentration as well as colloid-polymer size ratio [18, 19, 32–35]. In this work, we have employed a well understood colloid-polymer system in order to investigate the local structural changes in reaching equilibrium ordered state. The next section briefly discusses the self-assembly process. Further details regarding the colloid-polymer system is given in the succeeding chapters.

1.2 Self-assembly

Self-assembly is the organising of blocks into ordered pattern or structure without human intervention. This process is evident in nature and technology; for example in the assembly of viral capsids [36, 37], crystalisation process [27, 38, 39] and application in photonics [40]. To develop new materials understanding this seemingly simple process is important in order to synthesise novel and highly functional materials. To correspond to the technology demands for smaller and lighter components as high and smart functioning materials, understanding the pathway

of nanoscale units in nature organising themselves into ordered structures is the most convenient. This convenient route is not a trivial process. The dynamical process of individual components arranging themselves into ordered structures has been investigated in various fields; nanoengineering [36, 41, 42] and biomaterials research [43, 44]. Of late, rapid advances in the synthesis of self assembling building blocks are contributing to the understanding of self-assembly processes. For example, novel building components enable significant control of assembly to target products [45–47] and the synthesis of particles with controllable interactions [48–50], where an ordered phase of these particles was reported [51–54].

During the dynamical self-assembly process, the formation of disordered aggregates often disrupts the formation of stable ordered phase. However, it is not always clear whether the sources of this disruption is caused by thermodynamics or kinetics [55]. A balance between the thermodynamic stability for assembly of ordered equilibrium state and kinetic accessibility is required in a successful self-assembly. However, the former favours strong attractions between assembling units which generally occur at low temperature. While, the latter requires the self-assembly to take place within experimental timescale which is promoted by high effective temperature and weaker bonds. Moreover, kinetic accessibility does not lead to any aggregation of the units due to weaker attractions. Also, excessive strong interactions may lead to kinetically trapped structures preventing any adjustment to incorrect bonds. Ideally, the attraction must be weak enough to allow reversibility to the incorrect bonds leading to effective self-assembly. Figure 1.1 illustrates this competition. In the classical theories of phase transition [56] limitations are often discussed in terms of topological defects while determining the scaling regimes relative to the transition towards ordered arrangements often overlooked kinetic trappings. These events are often encountered in experiments. For example, in the work reported by Lu *et al.* [57], a stable phase of colloidal clusters fluid was observed where the clusters are diffusing freely without merging or forming a network of connected clusters. The observation of a fluid of clusters phase [57] refuted the expectations that colloidal particles in colloid-polymer mixtures should phase separate based on simulations and theories.

The addition of polymer to colloidal suspension is analogous to quenching the system. This would result to dynamically arrested network called gel. At this far from equilibrium state, we investigated the local structures evolution within the colloid-polymer system.

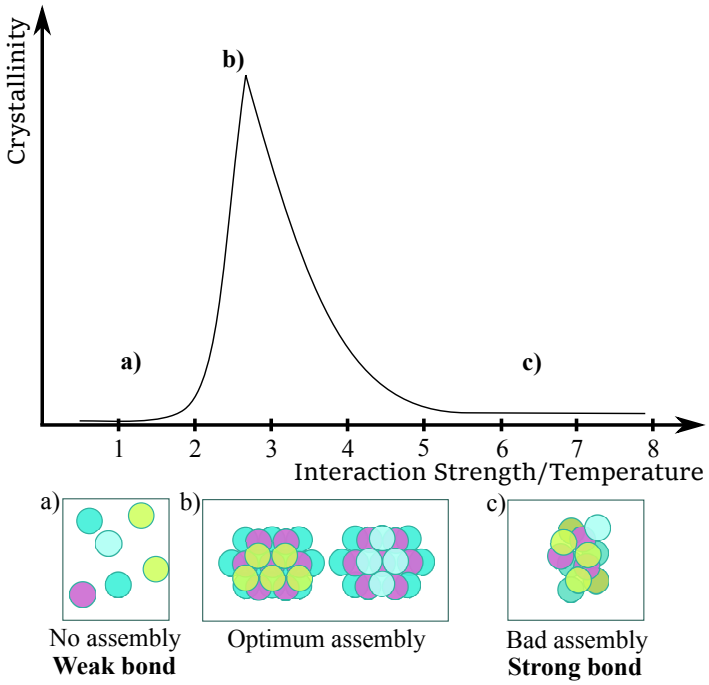

FIGURE 1.1. An illustration of the competition between thermodynamic stability and kinetic accessibility. (a) Lack of assembly at weak interaction strengths and free assembling units, (b) crystalline arrangement signifying optimum self-assembly is achieved at intermediate interaction strength while (c) too strong interaction strengths lead to kinetically trapped structures [39, 58].

1.3 Thesis Outline

We have introduced the prerequisites in order to consider the work described in this thesis. The following chapters give deeper details to the key topics discussed here and further correlate our study. The details of the model systems used in this work, the fundamental interactions and the basic concepts behind their behaviour are introduced in Chapter 2. Also, further discussion on self-assembly, gelation, and an introduction to sedimentation (due to the density difference of the suspending medium and particles) are given. In Chapter 3, the materials and methods used in this work are listed. Details on the type of colloids, polymer and their characterisation are presented. In this work we also included results from simulations where the details of the simulations work are presented in this chapter. The methods employed in our structural analysis are also discussed here. The results are presented in Chapters 4 to 6. In Chapter 4, we study the ageing of colloid-polymer system by analysing the local structural changes in experiments and also simulations. The structural factors in suppressing local structural evolution towards crystallisation

are discussed. In Chapter 5, we investigate the effects of gravity on the gel under confinement. We compare the sedimentation in experiments to that in Brownian dynamics simulations. In Chapter 6, the interaction between the colloids are tuned according to the polymer thermal response in order to obtain improved self-assembly. The effects of tuning the interaction strength are described in this chapter. Finally, an overview of the work and a summary of key conclusions of each result chapter is presented in Chapter 7.

CHAPTER 2

Colloid-Polymer System

This chapter starts with the definition of colloids followed by the descriptions of the fundamental interactions commonly found in colloidal systems. Next, the equilibrium phase behaviour of the systems used in this work is introduced and briefly discussed then followed by the description of non-equilibrium "phase" behaviour of the systems. Lastly, the effects of gravity from dilute to high density suspensions are described.

2.1 Definition of colloids

The colloidal state was introduced by Thomas Graham in 1861. Coupled with the Brownian motion observed by Robert Brown, the studies of colloids played a vital role in the early progress of statistical physics. In recent years, the thermodynamics of colloidal systems have been extensively studied and established to be equivalent to an assembly of atomic systems with similar interatomic potential. One of the advantages of colloidal systems is that the interparticle interaction can be tuned to be repulsive, attractive or similar to hard spheres. This can be easily done by changing the solvent of the system, changing the surface of colloidal particles, adding salt or polymer [3, 6, 32, 59]. Therefore, colloidal systems are good model of atoms since the interaction of colloidal model can be tuned to mimic the interatomic interactions.

An important experiment carried out by Perrin in 1910, using dispersed resin colloids the Brownian motion is verified as indication of thermal motion instigated by Einstein's theoretical result [60, 61]. In the experiment, the equilibrium concen-

tration of the resin colloids in dilute suspension in the field of gravity are established to be exponentially varied with height. The height distribution of the resin colloids follows Boltzmann theory for sedimentation equilibrium. This demonstrates that colloids behave as "macro atoms". In his experiment, Perrin used conventional light microscope to track the diffusing colloidal particles. This observation was possible since the suspension was a dilute suspension where the image of resin colloids are visible on captured film enabling direct tracking. Since the ideal size of colloidal particles is situated close to the visible light spectrum, light scattering has been a popular method in obtaining the structure and dynamic of colloidal suspensions [62, 63]. Rheology is another method in studying colloidal suspensions by measuring the bulk viscoelasticity. This measurement from macroscopic sample is then compared with a theoretical microscopic model [64–67]. Also, individual colloidal particles can be resolved using conventional optical microscopy which has been utilised previously in studying colloidal suspensions [68]. However, there are many disadvantages of the methods listed here. Conventional optical microscopy suffers multiple scattering from dense objects leading to image blurring. While it is possible to measure the fraction of crystallinity within a colloidal sample using the light scattering method, it is not possible to examine its local properties such as the shape of the crystalline domain. Additionally, the structures and dynamics at short length scales obtained from the rheology measurements are only indirect inference from the macroscopic results. Thereafter, direct imaging techniques become the common method in studying the physical world of colloids particularly the use of confocal microscopy. Recent trends in using confocal microscopy for colloidal systems have led to rapid advances in studying colloidal phase behaviours and the formed local structures. Confocal microscopy pioneered by Marvin Minsky in 1957 enable images of 100s of micrometers in depth to be captured and reconstruction of the 3-dimensional (3d) structure from a thick specimen. This direct observation is made possible due to the size of colloidal particle which is in the mesoscopic range; between ~nm-~ μm. In contrast to atoms, the diffusion times of colloidal particles are significantly slower; the order of ms-s, making the observation of the particles in real time possible. Additionally, their diffusion is slow enough that quantitative measurements of their structures and dynamics are possible to be carried out [7].

Sedimentation or overall dynamics of the colloidal suspension is affected by the particle size. In sedimentation, the gravitational force can still play a major role in the colloidal length scale compared to thermal fluctuations. The effects of gravitational force F_g on thermal fluctuations k_BT is expressed in gravitational height, h given as:

$$h = k_B T / F_g \tag{2.1}$$

The gravitational force F_g acting on a colloidal particle with diameter σ is given as:

$$F_g = (\sigma^3 \pi \delta \rho g)/6 \tag{2.2}$$

where $\delta\rho$ is the mass density difference between the colloid and the solvent. Changes to the gravitational height h are possible either by placing the colloidal suspension in a low gravity environment, for example in space, or inducing high gravity in the suspension by using solvent with significantly low density than the colloid [69–72]. For an ideal colloidal system, the gravitational height h needs to be larger than the sample chamber or capillary height so that gravitational effects can be neglected.

Likewise, the diffusion of particles in a colloidal suspension is also affected by the particles' size. Specifically, smaller particles diffuse much faster than larger particles. The diffusion rate of a particle with diameter σ in a solvent of η viscosity is given by the diffusion coefficient D:

$$D = k_B T / 3\pi\eta\sigma \tag{2.3}$$

The time scale for a particle to diffuse its own diameter is called Brownian time, τ_{B}:

$$\tau_{\mathrm{B}} = \sigma^2 / 24D \tag{2.4}$$

Meanwhile, in sedimentation, the time scale is given as τ_{sed}:

$$\tau_{\mathrm{sed}} = \sigma / v_{\mathrm{sed}} \tag{2.5}$$

where v_{sed} describes the motion of the colloid under the influence of gravity g:

$$v_{\mathrm{sed}} = (\delta m g)/3\pi\eta\sigma \tag{2.6}$$

where δm is the buoyant mass which can be determined from the mass density difference between colloids and the solvent times the colloid volume.

The ratio of the diffusive and gravity driven timescales gives us the Peclet number Pe:

$$Pe = \tau_{\mathrm{B}} / \tau_{\mathrm{sed}} \tag{2.7}$$

Therefore, we consider a suspension of particles to be a colloidal suspension when $Pe < 1$ [73].

In the next section, the major types of interparticle force in colloidal systems are described and related to the experiments performed in this work.

2.2 Colloidal interactions

2.2.1 Steric stabilisation

The purpose of steric stabilisation is to protect colloidal particles against coagulation and to produce colloids that are almost perfect hard spheres [74, 75]. To achieve this, the dispersing medium must be a good solvent for the anchored polymers. In good solvents the polymer chains are extended since polymer-solvent interactions are favoured in good solvents. Therefore, as the colloidal particles approach one another to a distance that is less than twice the layer thickness, the concentration of the polymer between the particles' surfaces increases. This results to an increase in osmotic pressure and subsequently causing a repulsive force. The overlapping of the polymer brushes from both surfaces, as illustrated in Fig. 2.1 limits the configurational degrees of freedom for the polymers and as a result leads to loss of entropy. The loss of entropy suppress further approach of the colloids. This repulsion range

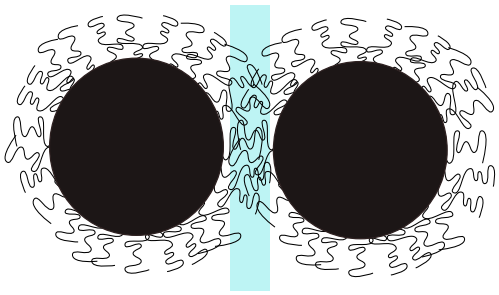

FIGURE 2.1. The interaction between polymer-grafted colloidal particles. The overlapping of anchored polymer brushes as the colloidal particles approach is shown in shadowed box. The loss of entropy due to limited configurational freedom leads to repulsion: steric stabilisation.

must be larger than the van der Waals attraction range in order to avoid aggregation. Alternatively, amphiphiles can also serve the same purpose. The hydrophobic tail covers the colloidal particles while the hydrophilic head protrudes into the water. Therefore, this type of steric stabilisation is most common in aqueous suspensions. In subsequent experimental chapters, all of our particles are sterically stabilised by the attachment of polyhydroxy stearic acid (PHSA) on polymethyl methacrylate (PMMA) particles. The use of PMMA as model colloids is also described in subsection 2.3.2.

2.2.2 Van der Waals interactions

Van der Waals interactions or London forces are ubiquitous in all atoms, molecules and colloidal suspensions regardless of whether the particles are electrically charged or otherwise. This interaction resulted from electrostatic attraction due to the mutual instantaneous fluctuation of electrical dipoles between two atom or molecules. The calculations of van der Waals forces acting on a pair colloidal particles can be integrated giving Equation (Eq.) 2.8 [76]:

$$U_{\mathrm{vdW}} \approx -A\frac{\sigma}{12d} \tag{2.8}$$

where σ is the diameter of the colloidal particles and d is the distance separating their two surfaces, while A is the Hamaker constant. The Hamaker constant is determined by considering the dielectric constants of the colloidal particles' materials and dispersed medium i.e. the liquid medium. Since the Hamaker constant is linked to the dielectric constants; relative measurements of the materials chemical polarity, it also affects the refractive indices of the dispersed phase and medium. Generally, the dielectric constants of the dispersed phase and medium differed greatly inducing the van der Waals attractions between the colloidal particles. Eq. 2.8 shows that $U_{\mathrm{vdW}} \to -\infty$ as $d \to 0$, marking an irreversible aggregation due to the van der Waals attraction forces.

However, in all our work described in Chapters 4, 5 and 6 the particles are sterically stabilised and the solvent system in chapter 4 are modified to have the same refractive index as the colloidal particles. Therefore, the van der Waals interactions are ignored throughout this work.

2.2.3 Electrostatic repulsion

Many surfaces are charged and the same can be expected for the surface of colloidal particles. The charge may be acquired from the dissociation of chemical groups at the particle surface or the adsorption of charged species. Colloidal particles can usually be thought of as being in a continuous medium where dissolved ions are always present thus screening the Coulombic interactions. Consequently, consideration of the ionic strength of the dispersed medium and the ionic distribution on the charged surface are required.

Due to the electrostatic field caused by a charged surface, the ions present in the solvent are not distributed homogeneously. The surface charge neutrality is maintained by a layer of counterions, tightly bound to the surface which is called the Stern layer. This is coupled with a diffuse concentration region of counterion and coions beyond the layer into the solution. Together, the Stern and diffuse layers are known as the electrical double layer and are illustrated in Fig. 2.2. As the charged

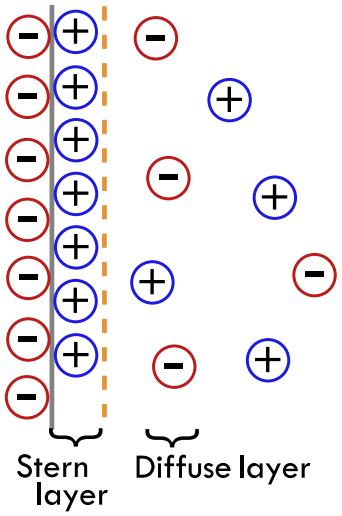

FIGURE 2.2. The electrostatic double layer comprises of Stern layer with counterions bound to a surface and a diffuse layer containing counter- and co-ions [77].

surfaces approach each other, an increase of ionic concentration occurs due to the overlap of the double layer. Then, the osmotic imbalance keeps the two surfaces apart resulting to a repulsive forces between them.

The range of the repulsive domain is represented by the Debye screening length κ^{-1}. For a colloidal suspension this length can be approximated (see Eq. 2.9) by solving the linearised Posison-Boltzmann theory [77].

$$\kappa^{-1} = \sqrt{\frac{1}{8\pi\lambda_B N_A I}} \tag{2.9}$$

where I is the ionic strength in the unit mol/dm and λ_B is the Bjerrum length:

$$\lambda_B = \frac{e^2}{4\epsilon_0\epsilon_r k_B T} \tag{2.10}$$

where e is the species charge, ϵ_0 is the relative permittivity in vacuum while ϵ_r is the dielectric constant of the medium.

In order to describe the interactions in of charged colloidal particles, the Coulombic potential can be modified and the pair potential from this is expressed as a Yukawa potential:

$$U_{Yuk}(r) \propto \frac{\exp(-\kappa r)}{r} \tag{2.11}$$

where r is the distance between two particles. Accordingly, as the κ in Eq. 2.11 becomes large the potential resembles to a Coulombic form.

2.2.4 Charge stabilisation

Without any repulsive forces, colloidal particles in a polar suspension will experience van der Waals attractive forces and fall into the attraction potential minima forming irreversible aggregates. While the double layer surrounding the colloidal particles affectively increases the energy barrier for the system to aggregate as the particles approach each other. Therefore, the linear addition of the van der Waals attraction potential to the electrostatic repulsion potential becomes the foundation of the Derjaguin-Landau-Verwey-Overbeek (DLVO) theory. Combining these two potentials; U_{vdW} and U_{Yuk} as the attraction and repulsion potentials respectively, produces a total potential U_{DLVO} for stabilised colloidal particles as given in Eq. 2.12.

$$U_{\mathrm{DLVO}}(r) = U_{\mathrm{Yuk}} + U_{\mathrm{vdW}} \tag{2.12}$$

For our work in chapter 4, a salt solution is added to screen the strong repulsive particle interactions due to particle charges.

2.2.5 The depletion interaction

The depletion interactions are the results from the presence of particles with sizes that are between the size of suspended colloidal particles and molecules of the suspension. Examples of the cosolutes are surfactant and polymer. When the polymer solution is added to a suspension of colloidal particles, it is assumed that the polymer coils can interpenetrate while the colloidal particles are not and the coils cannot be adsorbed onto the surface of colloidal particles. The polymer molecules are shown in Fig. 2.3 as spherical coils. They are excluded from the colloidal particles in a range of the polymer's radius of gyration, R_{g}. This exclusion region is called the depletion zone. As the two colloidal particles approach, the polymer coils are excluded from the region. Therefore, the number of polymers in between the particles is lower when compared to that of bulk solution. Subsequently, the imbalance of osmotic pressure between the bulk solution and the overlapping depletion zone leads to an attractive interaction in the colloidal suspension. From another perspective, when the depletion zones overlap, there is an increase of free volume for the polymers in the bulk solution and correspondingly an increase of the configurational entropy. Thus, the mechanism for the depletion interaction is purely entropic. A common model representing the depletion mechanism is the Asakura-Oosawa (AO) model [15, 16] and is expressed in Eq. 2.13. The range of the depletion interaction can be controlled by changing the diameters of colloidal particles σ or polymers $2R_{\mathrm{g}}$. The size ratio between the diameter of the colloidal

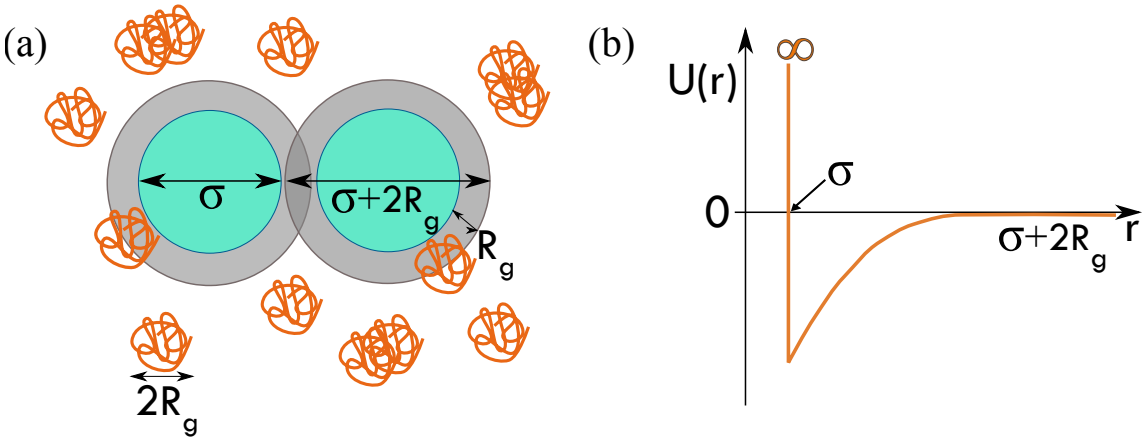

FIGURE 2.3. A schematic sketch of Asakura-Oosawa model of colloid-polymer mixture. The solid green circles represent colloidal particles, and the nonadsorbing polymers (a) are random spherical coils. The boundary of the depletion zone is shown by the gray shaded area around each colloid at a diameter of $\sigma + \sigma_P$. Inset (b) shows the pair potential $U_{\mathrm{AO}}(r)$ for the colloids as given in Eq. 2.13.

particle and polymer is usually expressed as $q = 2R_g/\sigma$. Also, the depletion interaction strength which is always attractive can be tuned by varying the polymer concentration c_p and is in the unit of k_BT.

$$\beta U_{\mathrm{AO}}(r) = \begin{cases} \infty & \text{for } r > \sigma \\ -\frac{\pi\sigma_P^3 z_{\mathrm{p}}}{6}\frac{(1+q)^3}{q^3}\left[1 - \frac{3r}{2(1+q)\sigma} + \frac{r^3}{2(1+q)^3\sigma^3}\right] & \text{for } \sigma < r \le \sigma + \sigma_P \\ 0 & \text{for } r \ge \sigma + \sigma_P \end{cases} \tag{2.13}$$

where β is $1/k_BT$ k_B is the Boltzmann constant and T is temperature. q in equation 2.13 is the polymer-colloid size ratio. The polymer volume fraction ϕ_{p} is represented by $\frac{\pi\sigma_{\mathrm{p}}^3 z_{\mathrm{p}}}{6}$ in equation 2.13. The polymer fugacity z_{p} is the same as the number of density ρ_{p} of ideal polymer in the reservoir. In an Asakura-Oosawa (AO) model the effective temperature is inversely proportional to the polymer reservoir concentration. For the rest of this work, the interaction strengths in colloid-polymer mixtures are expressed as k_BT. The equilibrium phase behaviour of colloid-polymer mixture is detailed in Section 2.3.3.

2.3 Phase behaviour

The interactions of colloidal particles can be tuned depending on the system and the suspension medium constituents, as was discussed in the previous section. This wide range of interactions allows the colloidal suspension to exhibit interesting phase behaviours, essentially the same range as the phase behaviour of matter, with the colloids play the role of the atoms [62]. In this section, the phase behaviour of some colloidal models are discussed, then the phase behaviour of the colloid-polymer system which is used throughout this work is discussed. The free volume theory and the extended law of corresponding states are also described in order to represent the topology of colloid-polymer system phase diagram. The phase behaviour of our colloid-polymer system is not significantly affected by confinement due to the system size $\sim 200\sigma$. However, the effects of gravity on this system is introduced in Section 2.6 are further explored in Chapter 5.

2.3.1 Hard spheres and their phase behaviour

The hard sphere model plays a vital role in statistical physics as a model for simple liquids. In this model, an assembly of perfect spheres has an infinite repulsion when the spheres are in contact and no interactions at separations larger than their radius. In the absent of interparticle attraction the ideal system is considered athermal. Thus, the phase behaviour is determine only by the particle volume fraction, $\phi = (\pi\sigma^3 n)/6$ where σ is the particle diameter and n is the number density. Increasing the ϕ can change the phases of the hard spheres from fluid to solid. A schematic phase diagram of hard spheres is shown in Fig. 2.4. When $\phi \backsimeq 0$ the system is very dilute and the spheres are disordered like gas. The spheres remain in a disordered state with the increasing of ϕ and appear to be in liquid state as the system becomes denser. The freezing transition of hard spheres was predicted quantitatively in early computer simulation work [78, 79]. In their work, there is a coexisting phase of fluid and solid at freezing transition, between freezing at $\phi_f = 0.494$ and melting at $\phi_m = 0.545$. The spheres in this coexisting region, are in crystalline states at $\phi_m = 0.545$ and liquid domains at $\phi_f = 0.494$. This was proven in experiment three decades later [3] using sterically stabilised polymethyl methacrylate (PMMA). They studied the phase behaviours of the colloidal particles and found the same co-existing phase of fluid-crystal as was reported in simulations.

According to Kepler's conjecture, the maximum density or packing fraction ϕ for spheres in a regular close-packed structure is $\phi_{cp} = \pi/\sqrt{18} \backsimeq 0.74$ [80]. Also, if the spheres are packed in a random organisation which is called random close packing, the maximum volume fraction is $\phi_{rcp} \backsimeq 0.64$ [81–83]. The above-mentioned

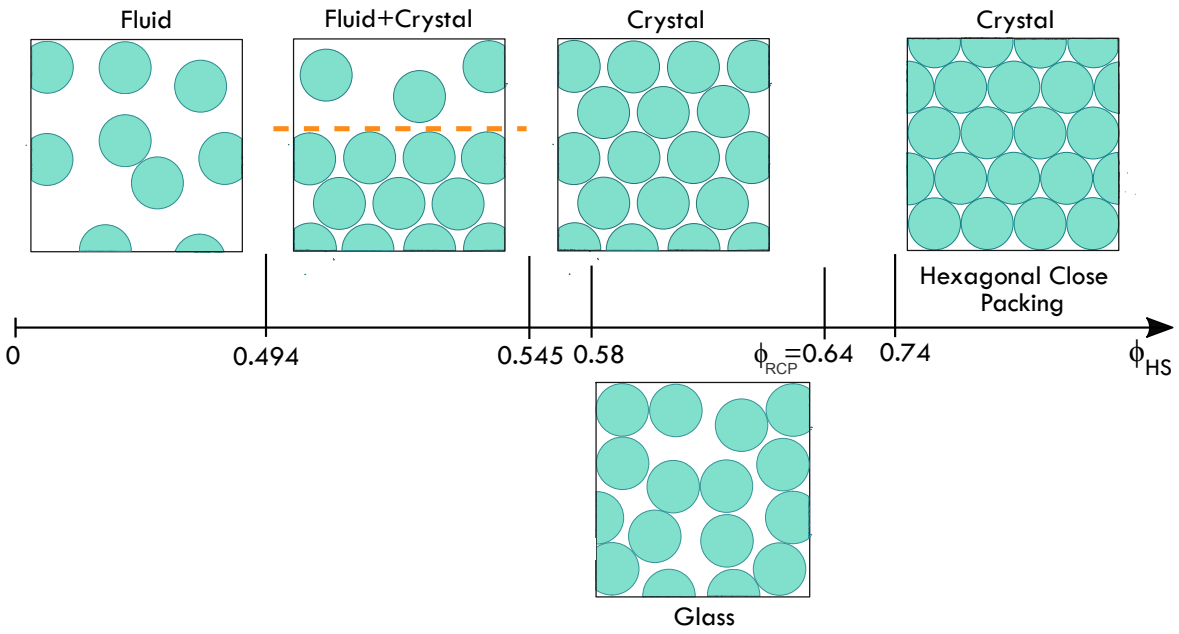

FIGURE 2.4. Phase behaviour of hard spheres with increasing ϕ_{HS}.

experiment and simulation work led to the recognition that the phase transition is purely entropic. In an ordered crystalline structure the configurational entropy is reduced due to the long range order making the disordered structure in fluid favoured. Nonetheless, the disorder in fluid almost always leads to a "jammed" state, as shown in Fig. 2.5. In this state, the movement of a sphere is limited in a volume that is influenced by the fixed surrounding spheres and is greatly reduced. On the other hand, in an ordered crystalline phase each sphere still has significant freedom to move within the space formed by its nearest neighbours. The increased free volume in turn increases the entropy of the crystal making it more favourable than the disordered fluid.

In the hard sphere phase diagram, the crystalline phase remains from $\phi_{\mathrm{m}} = 0.545$ to maximum close packing $\phi_{\mathrm{cp}} \simeq 0.740$. If a system of hard spheres is compressed rapidly, the spheres' crystallisation are bypassed and a metastable and kinetically trapped state: the glass state is formed. This amorphous state has been estimated at $\phi \simeq 0.61$ [84] and remains up to random close packing, $\phi_{\mathrm{rcp}} \simeq 0.64$. The colloidal particles are considered to be in a glassy state because of a significant increase in viscosity without any visible structural changes [75, 85, 86]. This arrested phase transition has been observed in atomic and molecular systems [87] and is called the glass transition.

There are many suspensions of spherical particles that are considered as "model"

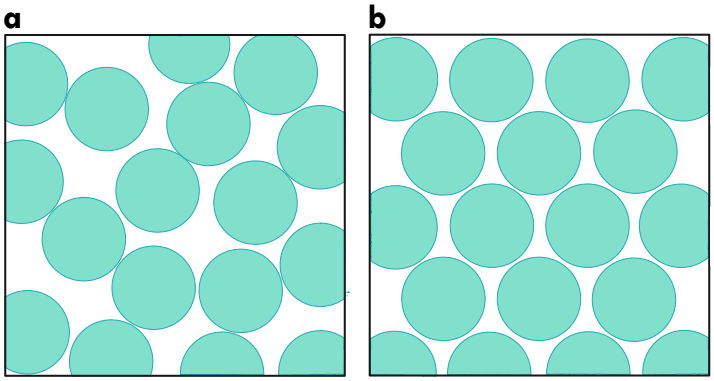

FIGURE 2.5. An illustration comparing the free volume in (a) dense liquid and in (b) crystalline solid at the same density. Clearly, there is more space and less jamming in the crystalline than the disordered configurations.

suspensions of colloids. These suspensions are convenient models due to their accurate spherical shape like polystyrene and compatibility for light-scattering studies like silica [62]. However, each of this example has its own shortcomings. Besides, polymethyl methacrylate (PMMA) phase behaviour been proven to mimic the hard sphere phase diagram [3]. Thus, making PMMA the best and accessible system to be used in experiments as colloidal suspension model. The next section briefly describes the properties PMMA as model system.

2.3.2 Polymethyl methacrylate(PMMA) as model hard spheres

PMMA is one of most common materials used for colloids employed in experiments. These spherical particles are covered with polymer containing a PMMA stem, attached to the particle surface, and the brushes dangling from the stem are polyhydroxy stearic acid (PHSA) [88]. These brushes prevent coagulation by steric stabilisation, as was mentioned previously in subsection 2.2.1. In the case of confocal microscopy studies, fluorophores are used as dyes for these particles [89]. The density of PMMA is 1.19 g cm^{-3} and it has the refractive index of about 1.49. In order to have an index-matched suspension of PMMA, a mixture of solvents are used as a suspension medium. Many of these mixtures consist of two-components: one component with low-refractive index like decalin and another of high-refractive index like cyclohexyl bromide. These mixtures not only match the refractive index of PMMA but also the density, making the particles suspended for a significant length of time.

2.3.3 Colloid-polymer mixture

Based on the theory of Gast *et al.* [35] the topology of colloid-polymer phase diagram can be predicted by the range of the depletion attraction which can be determined from the size ratio between polymer and colloid $q = 2R_g/\sigma_c$. The phase behaviour of colloids without the addition of polymer is previously discussed where crystallisation occurs at ϕ_c=0.494 but the addition of small polymers ($q \sim 0.08$) enlarges the fluid-crystal coexistence region of hard-sphere system [18]. Meanwhile, the addition of larger polymer brings about gas-liquid, gas-crystal and gas-liquid-crystal coexistences and thermodynamically stable colloidal gas and liquid are present in

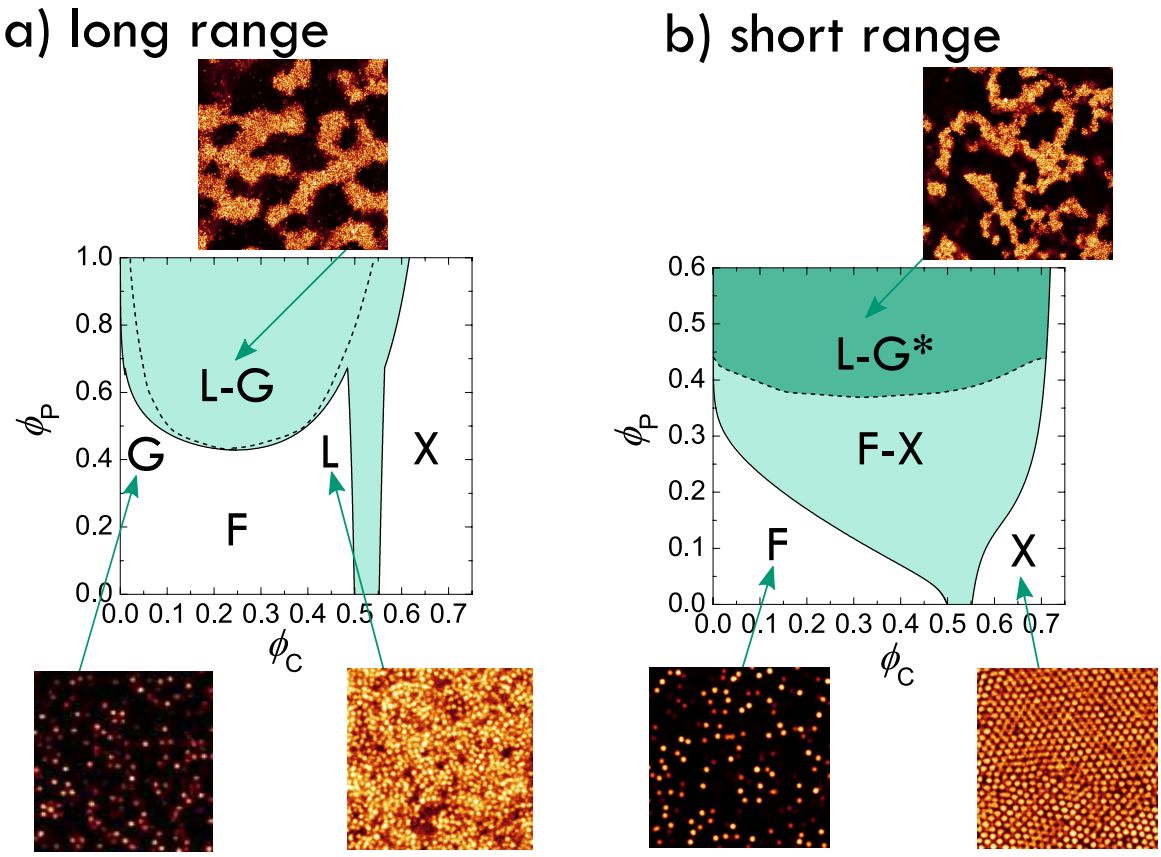

FIGURE 2.6. Figure shows the phase diagram of colloid-polymer mixtures where the interactions are determined from Eq. 2.13. The x-axis is the colloid volume fraction (ϕ_c) and y-axis represents the volume fraction of polymers (ϕ_p). The plot in (a) shows the long-ranged attraction ($q \sim 0.45$) while (b) indicates the plot for short-ranged attraction($q \sim 0.18$). The symbols are as follows: F=fluid, X=crystal, G=gas and L=liquid. This is adapted from [73].

these mixtures [35]. In a colloid-polymer phase diagram, binodal or spinodal line is used to distinguish experimental phase boundaries. A binodal represents the states where two or more discrete phases are in coexistence whereas a spinodal denotes the boundary where complete instability of the system leads it to decomposition (this is discussed further in 2.5). A line connecting two-points on a binodal is called the tie-line. In Fig. 2.6 the binodal and spinodal is shown as solid and dashed lines, respectively. The plot in 2.6 (a) shows that at lower ϕ_c, the fluid phase separates into liquid and gas when it is quenched above the coexistence line (solid line in the plot) while the system crystallise at higher ϕ_c. In the short-ranged attraction plot in 2.6 (b) the metastable liquid-gas phase separation resulted into gel formation which is also discussed in subsection 2.5.

In the early theoretical work, the calculations of phase transitions of systems with depletion interactions were possible by considering the depletion effect as a perturbation on the hard-sphere free energy [35, 90]. However, in this work, the polymer partitioning in the coexisting phases was not taken into consideration. In a system with more than a single phase the polymer is separated from the colloid-rich phase. The partitioning of polymer across the phases is described in a model developed by Lekkerkerker *et al.* called the free volume theory.

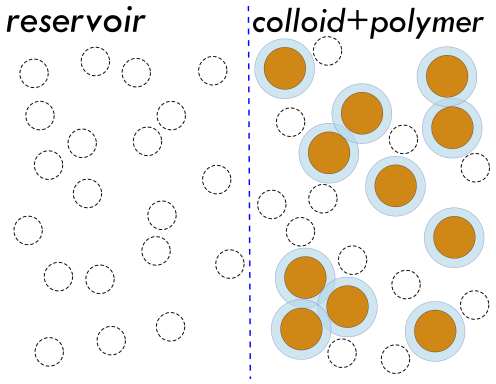

FIGURE 2.7. A sketch showing the colloid-polymer (shown as blue and white circle respectively) system on the right is in osmotic equilibrium with a polymer reservoir. The dashed line is the theoretical membrane that allows the solvent and polymer passing through except the colloids.

Based on the free volume theory the phase diagram can be introduced in two representations which are the experimental and reservoir representations. The experimental representation gives the polymer concentration in the whole system which is obtained from the amount of polymer added into the system. Whereas in the reservoir representation, the polymer concentration is determined based on a hypothetical reservoir of pure polymer solution in equilibrium with the colloid-

polymer system, as is shown in Fig. 2.7. The polymer solution reservoir takes into consideration the different excluded volumes in coexisting phases. The conversion between the two representation is carried out using Widom's insertion method to determine the free volume fraction $\alpha(\phi)$ [33] given by:

$$\alpha(\phi) = (1-\phi)\exp(-A\gamma - B\gamma^2 - 3\gamma^3) \tag{2.14}$$

where $\gamma = \phi/(1-\phi)$, $A = 3q + 3q^2 + q^3$, $B = 9q^2/(2+3q^3)$ and $C = 3q^3$.

The effects of curvature on the phase behaviour of colloid-polymer mixtures when the ideal polymers are replaced with polymers with excluded-volume interactions was examined by extending the free volume theory [91]. The aforementioned effects are small in colloid-polymer mixtures with low size ratios q. However, it was pointed out for colloid-polymer systems with large size ratios, $q = 0.6$ and 1.0, the gas-liquid coexistence domain re-position to higher polymer concentrations due to the effects of curvature and excluded-volume interactions. Further work was also done in [92] where solvent is no longer treated as background in the colloid-polymer system. Again, the numbers reported by the authors are rather similar to the original free volume theory by Lekkerkerker *et al.* [93] for small size ratios q. The authors analysis did however offer an analytical method for obtaining the colloid and polymer critical and triple points.

Here, we employed the Noro and Frenkel extended law of corresponding states in determining the critical point of the colloid-polymer systems and also the effective interaction strengths due to the small size ratio q throughout this work following previous work [94, 95]. The ordinates of phase diagrams throughout our work are represented in the reservoir concentrations or the attractive interaction strength. The determination of the interaction strength is discussed in Chapter 3.

2.4 Self-assembly

Self-assembly is a dynamical process of units coming together without external intervention into ordered organisation. This process is evident in nature in large range of scale; from the assembly of stars into galaxies to the assembly of protons, neutron and electrons into atoms. The natural processes of biological components coming together via self-assembly constructing stable and functional biological systems could be the blue print in synthesising novel materials.

Historically, the study of self-assembly originated from investigating molecular processes. The progress in technology heading towards nanometer- and micrometer-scale structures drives the focus of self-assembly to include matters larger than the molecular size range [96]. Recent developments in synthesising colloidal particles

with controllable interactions [47, 48, 50, 97, 98] and specific shapes have also promoted the theoretical and simulation analyses of the ordered phases formed by the units [1, 51–54, 99]. The use of colloidal particles (micrometer size range) in studying self-assembly offers many advantages that are not possible when using molecular scale components. Molecular systems are formed from a collection of atoms where the characteristics of the atoms regulate the interactions between the molecules. It is not a trivial task to alter the potential between two atoms and then study the self-assembly affected by this change in potential. In contrast, it is possible to adjust the interactions in a colloidal system (as was discussed in Section 2.2) across a various scale of strength, range and selectivity. In addition, colloidal particles are larger than molecular components permitting observation of the self-assembly processes and products formed using colloidal particles [7]. Furthermore, application specificity of an ordered states of matter suggested that self-assembly may be the only route in achieving the ordered arrays [100]. For example, the assembly pathway of ordered arrays of nanospheres for photonic crystals [101].

Self-assembly is a non-equilibrium process where the system starts from disordered phase moving towards a final stable ordered phase. The process is encouraged by the thermodynamics because the assembled structures have lower free energy than in the disordered components. An example of self-assembly is crystallisation [58]. This process is a well-studied transition where the free particles in the fluid state are spontaneously organised into ordered crystalline arrangement with overall lower free energy. Therefore, the nucleation and growth of the ordered crystalline phase become the focus point in the interpretation of self-assembly. A discussion related to colloidal crystal is given in subsection 2.5.2. The change of phases between the disordered and ordered phases requires overcoming of the free energy barrier and the formation of stable bulk phase. The classical nucleation theory (CNT) offers the basic description of the free energy cost and the stable cluster formation. A discussion in regards to the basic theory of nucleation is discussed in subsection 2.4.1.

In the work described here, we employed colloid-polymer mixture to study the self-assembly in non-equilibrium systems. The short-ranged interactions in the system are representative of protein molecules solution used in protein crystallisation [25–27] and similar to the constituents in directing light propagation in photonic applications [40, 102, 103]. However, the study of nucleation in protein solutions are difficult due to the specificity of molecules in proteins preventing the findings from one type of protein applicable to the other [27]. Therefore, studies using short-ranged attractive interaction like in the colloid-polymer system offers

simplicity and general theory for wider application.

The route to self-assembly is not without deviation. It requires a balance between thermodynamics and dynamics. The thermodynamic push towards attaining ordered equilibrium state prefers strong interactions at low temperature. However, attractive interactions that are exceedingly strong may hinder the structure organisation into ordered array by disabling the interaction capability to unbind and reversibility [37, 104]. Plus, ordered organisation requires components to align accurately with one another which may take an excessively long duration causing the slow development of the ordered state. This is highly against kinetic accessibility which demand that self-assembly to occur within a reasonable scale. Additionally, unlike the thermodynamic drive, kinetic accessibility favours weaker interactions at high temperature. During the dynamical self-assembly process, the formation of metastable disordered aggregates (kinetic traps) often disrupts the assembling components pathways to the ordered states [58, 105]. Therefore, microscopic reversibility is required so that the defects can be corrected during self-assembly by bonding and unbonding [37, 58, 96, 105]. The two conditions of ordered structure and reversibility of bonds suggests that spontaneous assembly is successful if the interactions are within a small optimum range [39, 55, 105].

2.4.1 Classical Nucleation Theory

The experimental and simulation studies on crystallisation rates are usually approached using classical nucleation theory (CNT) [27, 106–108]. Cooling water below its freezing point, T_f does not necessarily induce crystallisation, in fact this is also true in most liquids [108]. For example, water can be cooled to −10°C and remained as liquid for an indefinite period of time [109]. This indicates that the liquid is kinetically trapped in a thermodynamically unstable state. Even though the ordered crystalline structure is more favourable thermodynamically, its transition requires an overcoming of a high free energy for the creation of solid-liquid interface [110]. Based on the theory, the formation of a spherical nucleus the total Gibbs free energy cost involves two terms: the bulk and the surface terms as given in Eq. 2.15 and illustrated in Fig. 2.8.

$$\Delta G = \frac{4}{3}\pi R^3 \rho_s \Delta\mu + 4\pi R^2 \gamma \tag{2.15}$$

Here, R is the nucleus radius, ρ_s is the number density of the solid phase, $\Delta\mu$ is the chemical potential difference between the solid and liquid phases and γ is the surface free energy density [106].

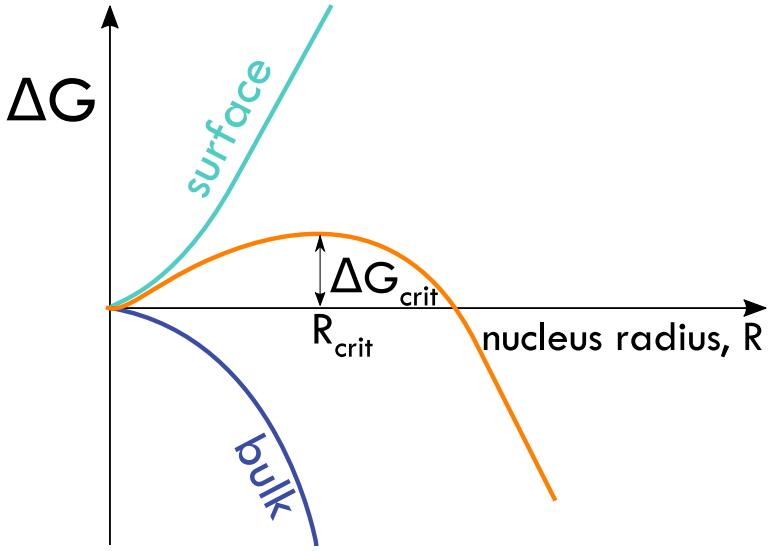

FIGURE 2.8. The free energy cost for the formation of nucleus is the total of the surface (unfavourable) and volume (favourable) terms. The maximum point in the free energy cost corresponds to the radius of the critical nucleus size.

The free energy increases to a maximum where $R_{\text{crit}} = 2\gamma/(\rho_s|\Delta\mu|)^2$ which is the critical nucleus size and the height of the nucleation barrier ΔG_{crit} is given by Eq. 2.16.

$$\Delta G_{\text{crit}} = \frac{16\pi}{3}\gamma^3/(\rho_s|\Delta\mu|)^2 \tag{2.16}$$

The critical nucleus size is a threshold that nuclei must exceed in order to counteract the surface free energy cost and nuclei growth becomes favourable [111]. Failing to reach this threshold the nuclei will dissolve since growth only leads to increase in free energy [108]. As the system moves away from the melting point the barrier of the nucleation lowers while $\Delta\mu$ increases with supersaturation. Using Eq. 2.16, the probability for the formation of critical nucleus P_{crit} can be determined from Eq. 2.17:

$$P_{\text{crit}} = \exp(-\Delta G_{\text{crit}}/k_B T) \tag{2.17}$$

The crystal nucleation rate per unit is expressed as a product of P_{crit} and a kinetic prefactor κ which describes the growth rate of the nucleus given in equation 2.18.

$$I = \kappa\exp(-\Delta G_{\text{crit}}/k_B T) \tag{2.18}$$

The kinetic prefactor κ is a product of $\kappa = \rho Z j$, where ρ is the number density of the liquid, or in a homogeneous nucleation, is the number of possible nucleation sites per unit volume [27, 108]. The term j is the rate of particles attaching to the critical nucleus driving its growth. It is dependent on the number of possible site on at the surface of the nucleus, the distance for the particles must diffuse to reach the nucleus λ and the diffusion constant D for the particles, as given in Eq. 2.19. The term Z is the Zeldovich factor defining the probability for a nucleus to cross the barrier and grow into a crystal after reaching the top of the free energy barrier [27, 108], as given by Eq. 2.20.

$$j = \frac{24 D n_c^{2/3}}{\lambda^2} \tag{2.19}$$

$$Z = \sqrt{\frac{\Delta\mu}{6\pi k_B T n_c^{2/3}}} \tag{2.20}$$

Both in Eq. 2.19 and 2.20, n_c is the number of particles inside the critical nucleus [108]. In Eq. 2.18, the exponential factor changes more rapidly with supersaturation than the prefactor, so the latter is often taken as a constant [27]. The crystal nucleation rate is often expressed using Eq. 2.21 in the analysis of crystal nucleation experiments [108].

$$I = \kappa \exp\Big[\frac{16\pi}{3}\gamma^3/(\rho_s|\Delta\mu|)^2\Big] \tag{2.21}$$

2.5 Gelation

In a colloid-polymer mixture the addition of polymer is equal to quenching the system [112, 113] by inducing attraction between the colloids. Increasing the amount of polymer in a colloidal system increases the attractive interactions which is similar to decreasing temperature in atomic systems. This leads to either cystallised or jammed system. As demonstrated in 2.3.3, the addition of polymer expands the fluid-crystal coexisting region. Also, the gas-liquid binodal line is clearly observed in the phase diagram of larger colloid-polymer size ratio q. However, as q becomes smaller the gas-liquid binodal is "buried" within the equilibrium fluid-crystal coexisting region creating a metastable phase. It is in this region that spinodal decomposition occurs and phase separation between the gas and liquid creates a network of colloid-rich branches and colloid-poor diffusive domains. The combination of branches surrounding diffusive domains is called gel. Therefore, it is

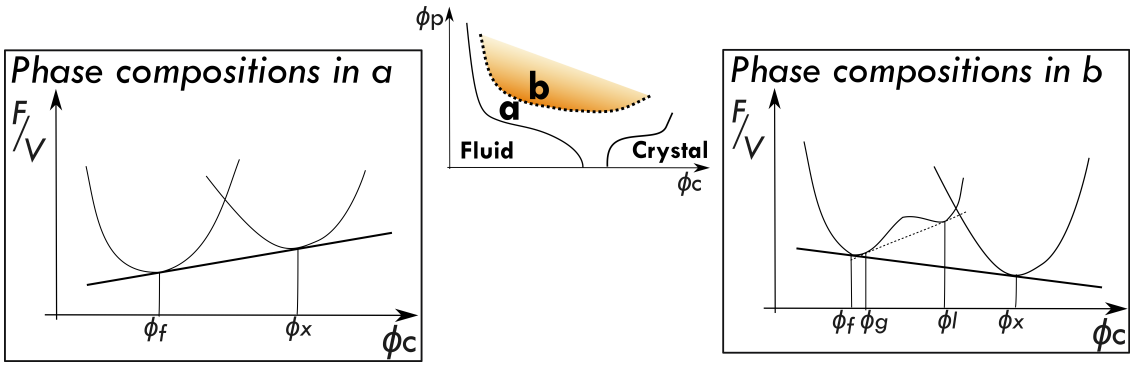

FIGURE 2.9. A sketch showing the phase compositions of a colloid-polymer system with $q \sim 0.1$ above the binodal line. The shaded area is the metastable domain inside the fluid-crystal equilibrium coexistence region. Adapted from [32].

useful to discuss briefly the phase transition occurring in the metastable fluid-fluid coexistence.

Let's consider the occurrence when the size ratio is smaller than the crossover $q_c \sim 0.3$. At this point, the liquid-gas binodal is "concealed" within the equilibrium fluid-crystal coexistence region creating a metastable phase domain represented as the shaded area in Fig. 2.9. The phase behaviour in **a** and **b** can be considered in free energy terms.

Close to the binodal at **a**, the initial mixture of colloid-polymer system phase separates into fluid and crystal phases with ϕ_{f} and ϕ_{x} as the compositions of the phases respectively. The compositions of the phases ϕ_{f} and ϕ_{x} are given by a single line with double tangent connecting the fluid (ϕ_{f}) and crystal (ϕ_{x}) regions. The addition of polymer increases the concentration of polymer in the system to **b** region where a curve is created in the fluid branch of the free energy curvatures. This in turn creates a double minima in the fluid branch and the double tangent connecting these minima provides the composition of the gas ϕ_g and liquid ϕ_l on the metastable phase shown as shaded area in Fig. 2.9. Similarly, a double tangent going across the fluid and crystal branch gives the composition of the coexisting fluid and crystal phase at equilibrium.

The metastable coexisting fluid-fluid phase will eventually reach an equilibrium state where a thermodynamically stable fluid-crystal coexisting phase is expected. Nonetheless, it is expected that gas-liquid phase separation progresses faster than crystallisation since breaking of symmetry is not required. In fact, the phase separation can occur rapidly due to spinodal decomposition. Within the spinodal line any small fluctuation in the unstable system composition is amplified. This will

eventually lead to phase separation in the coexisting domains.

Contrastingly, in the region between the binodal and spinodal shown in Fig. 2.9 as region**a**, phase separation occurs due to the formation of a nucleus that grows and ultimately induce the separation of coexisting phases into a more stable one-phase. The classical approach describing the formation of this nucleus is discussed in subsection 2.4.1. This nucleus where its growth leads to phase transition is called a critical nucleus. Therefore, it is natural to assume that a sample within the metastable gas-liquid will first phase separate to gas and liquid before finally nucleating crystals to attain equilibrium. Additionally, it is expected that a large number of the crystals are nucleated in the metastable liquid phase due to its higher density and closer to that of crystals than the metastable gas counterpart. This two-stepped crystallisation mechanism has been reported in binary hard sphere system, whereby the depletion attraction between larger hard spheres was induced by smaller hard spheres [114].

In the short-ranged attraction of colloid-polymer system, the colloidal liquid increases in density that leads to dynamical arrest; similar to what is observed in hard sphere glass transition. Therefore, above the spinodal line in a such short-ranged system a continuous network with colloid-rich branches is arrested and further phase separation is not possible. This type of network is typical in spinodal decomposition and the dynamically arrested network in colloid-polymer system is called gel.

How are gels made? According to previous work reported in [28, 115–117], gels are formed due to irreversible aggregation of clusters. In this mechanism, colloidal particles collide because of their Brownian motion and irreversible bonds forming rigid clusters. These clusters continue to diffuse and collide into one another, forming larger clusters filling space to form a gel. This type of aggregation is a non-equilibrium kinetic growth where full characterisation of the aggregation process must include the structure and shape of the clusters formed. Also, the time evolution for the cluster mass distribution must be considered in the aggregation process characterisation. This route to gelation holds only at low ϕ [118] while gelation is driven by spinodal decomposition at high ϕ.

Rearrangements in gel is possible in weak gels typically with interaction strength $U \lesssim 10\ k_B T$. In the depletion mechanism, depletant is added to a colloidal suspension of hard spheres which can cause phase separation via the depletion mechanism as described by [16, 17]. The depletants can be nonadsorbing polymers [24, 119] or surfactant micelles [120]. In our work, the nonadsorbing polystyrene is added to the solution to induce an attraction between the colloidal particles. Gel formed from depletion mechanism is one example of weak gels where varying polymer

concentration from low to high enable us to control the interaction strength of the gel. Structural rearrangements in gels are reported in simulations [121] and later in experiments [8]. As a result of rearrangements, the local structures are more compact albeit ramified clusters are expected to fill space inducing gelation. At lower interaction strengths U the local restructuring is too rapid that particles are unable to form compact clusters which are unable to fill space like in gels with higher U. The restructuring in gels continue to progress and some of the changes is motivated by thermal fluctuations. However, in non-density matched samples, solvent flow due to gravity might also contribute to the restructuring. This will be discussed further in 2.6.3.

The extended law of corresponding states is convenient in order to describe the colloidal and protein solutions [27, 122] as long as the potential range is notably smaller than the size of the particle. According to this law, all short-ranged attractive potentials have the same thermodynamics properties when compared at the same reduced density, where the length scale is the effective diameter σ_{eff} and second virial coefficient B_2 [123]. The second virial coefficient is given by:

$$B_2 = 2\pi \int_0^\infty [1 - \exp(\beta U(r))]\, r^2\, dr \tag{2.22}$$

where for colloid-polymer mixture the interaction potential $U(r)$ is the Asakura-Oosawa potential. The critical point of all systems with short-ranged attraction potential occurs at a fixed value of the reduced second virial coefficient B_2^* which is:

$$B_2^* = \frac{B_2}{(2/3)\pi\sigma_{\text{eff}}^3} \simeq -1.5 \tag{2.23}$$

2.5.1 Attractive and repulsive glass

Dynamical arrest in colloidal system with short-ranged attractive interactions leads to gels and glasses via gelation and vitrification, respectively. The colloidal system is considered to be in non-equilibrium state due to gelation and vitrification [3, 32, 34].

When colloidal particles are arrested due to a “caging” effect formed by the surrounding particles localising the particles within the formed “cage??. This is an indicator of the repulsive glass phase. The addition of nonadsorbing polymer induces effective attraction between the colloids which in turn promotes the relaxation process where the system can crystalise. However, increasing the attraction strengths, the particles become more localised due to the bonds between the neighbouring particles. As a result, the system is arrested in an attractive glass at lower ϕ [34].

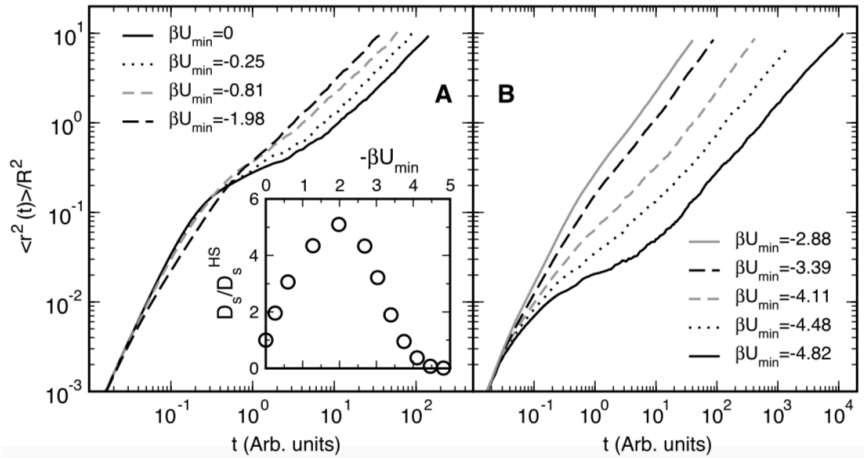

FIGURE 2.10. The plots show the mean-squared displacement (MSD) of colloidal particles with AO attraction at ϕ=0.50 for increasing attraction labeled as βU_{min}. The inset displays the correlation of the single-particle long-time diffusion with attraction strength. Adapted from [34].

The mean-squared displacement (MSD) of repulsive and attractive glasses is shown in Fig. 2.10 adapted from [34]. The plots are simulation results of almost hard spheres with AO attractions at ϕ=0.50 with varying interaction strengths. In the absence of attraction, a drop in mobility at 10^{-1} is displayed indicating a slower dynamics consequential to its proximity to the glass transition. This can be contributed to the localisation of the particles inside the "cage" formed by the surrounding neighbours. However, the mobility started to rise with the increasing short-range attraction signalling particle diffusion and a departure from the glass transition [124, 125]. Noticeably, the MSD for the attractive glass is smaller than that of the repulsive glass. It was suggested that this is due to the long-lived neighbour bonds which lessen the dynamics of attractive glasses [34, 64, 126–128]. Nevertheless, increasing the attraction further, initiated another drop in mobility (at 10^2) suggesting that the system is again approaching a glass boundary due to bonding-dominated arrests [129].

2.5.2 Colloidal crystals

The phase separation that spontaneously occur in the coexisting phase at volume fraction $0.494 < \phi < 0.545$ in the hard sphere model offers significant microscopic

details. These details give light on the dynamics of nucleation and development of solid state crystals by observing the colloids in real space and time. The same observation is unlikely to be performed on atomic systems due to their smaller size and more rapid diffusion.

Observations carried out in 2 dimensions (2d) identify crystalline domains using the local bond orientational parameter ψ_6 [130]. This measurement detects hexagonal ordering. For a specific particle, the nearest neighbours are positioned 60° from one another, giving values ranging from 0 to 1, where ψ_6=1 indicates a perfect hexagonal 2d crystal. For our work in Chapter 6, 2d bond order parameter measurements are performed in order to signify the crystalline domains in our results. Further details regarding ψ_6 is presented in Chapter 3 under subsection 3.7.4. Additionally, bond orientational order parameters can also be used for probing 3d crystalline domains [117]. Here, a pair of particles that have the same orientation as their neighbours are categorised as ordered neighbours. As a result, particles that have ordered neighbours of 8 or more are considered as being crystal-like [131].

The observation of nucleation and growth during the crystallisation of colloids in a bulk system was done in real time [7]. Similar to what has been discussed in the previous section (see Classical Nucleation Theory Section 2.4.1), the free energy that determines the growth rates has two competing factors which are the chemical potential and surface tension. The surface tension that lies between the crystal and liquid phases increases the free energy. Meanwhile the difference in chemical potential in the crystal phase compared to the liquid phase lowers free energy. Therefore, the surface tension dominates in small crystalline domains reducing the size of the ordered regions. However, above a critical size the chemical potential term takes over and oppress the surface tension term. These were evident from observations using confocal microscopy [7]. In their work, a critical size consists of around 60-100 particles were measured.

The structures of crystals after the critical point were also investigated, and the nuclei were discovered to be in random hexagonal closed packed (rhcp). This discovery is consistent with crystal nuclei found in computer simulations and light scattering measurements [74]. The crystalline domains were discovered to have rather non-spherical shape and uneven interfaces with the fluid phase. It was suggested that this is due to the decreased surface tension. This conclusion is further supported by the slight difference in free energy between the fluid and crystal phase. It was found that the crystal growth rate was reduced because of the presence of contaminants in 3d bulk systems [132]. This decrease was more prominent closer to the contaminants due to the disproportionate nature of the contaminants to a crystalline structure and evident by the presence of fluid layer

around the contaminants.

The low interfacial tension between the crystal and fluid phases makes the thermal fluctuations become significant and affects the distinguishable features of the interface. Carrying out the study of these effects is important to other systems with low surface tension evident in biological lipid interfaces. The effect of gravity at the fluid-crystal interfaces was investigated by regulating the buoyancy and then detecting the width of the interface [133]. What they observed was, the interface of the fluid-crystal broaden as they increased the density difference between the particles and the solvent. They suggested that the interface became more rough due to the increase transfer of particles to the interface due to the density difference which induces the non-equilibrium feature of the interface. Therefore, the local number density and the fluctuations at the interface are also increased. Similar outcomes are expected to be observed in other interfacial systems like the gas-fluid interface and in systems influenced by external forces.

Other than experiments of non-equilibrium nature of colloidal crystals, the equilibrium structures of colloidal crystals are also widely studied. These studies addressed the defects and grain boundaries, generally observed in atomic and molecular crystals [134, 135]. In these work, face-centred cubic (fcc) crystals were developed on patterned surface from colloidal sedimentation [134, 136]. Dislocations of the crystal were possible by controlling the particle size according to the lattice parameter of the surface [134]. At the defects, the closest particles configurations were found to be hexagonal close packed (hcp) and that the order of the planes change due to the defects. They also showed that the defects led to a partial dislocation called Shockley fault which has also been reported in fcc metals. As a conclusion, these colloidal crystals were able to demonstrate similar features that are observed in other ordered systems like atomic crystals.

2.6 Sedimentation

A gravitational force proportional to the density difference between a particle and the suspending medium acts upon the particle when there is a density difference between the particle and the suspension medium. The gravitational effects on a singular particle are comparable to the effect of random thermal motion at colloidal length scale. However, in attractive systems sedimentation becomes significant even in systems where the particles are too small to sediment in the laboratory time scale. Sedimentation kinetics are rather straight forward in dilute suspensions while a number of complexities arise for aggregated and dense suspensions.

2.6.1 Sedimentation profiles

For a dilute solution of monodispersed particles with mass m, it has similar density profile as ideal gas described by barometric law under the influence of gravity at equilibrium. The barometric law is given by

$$\rho(z) = A\exp(-\frac{z}{l_g}) \tag{2.24}$$

where A is a constant, z is number density of the particle and l_g is the gravitational length and given by $l_g = k_B T/mg$. In colloidal suspensions, m is the buoyant mass m_b where the density difference $\Delta\rho$ between the colloids and their solvent: $m_b = \Delta\rho\pi\sigma^3/6$ where σ is the colloid's diameter [137, 138].

The osmotic pressure for such sedimenting colloids can be determined. Assuming there is a slab with Δz height and A as area. When the colloid is not sedimenting or falling in the solution, according to hydrostatic equilibrium the forces from below and above the slab must be equal and opposite; making the force for the buoyancy of the colloids in the slab as:

$$F_{\text{down}} + (\Delta z A\rho m_b g) - F_{\text{up}} = 0 \tag{2.25}$$

where $F_{\text{down}} = \Pi_{\text{down}}/A$ where Π is osmotic pressure. By letting $\Delta z \to 0$ so that it becomes dz, we can integrate equation 2.25 to obtain the osmotic pressure for the sedimenting colloids:

$$\beta\Pi(z) = \frac{1}{l_g}\int_z^h \rho(z)dz \tag{2.26}$$

The barometric law is only valid for dilute solution. For higher density solutions, the osmotic pressure of the the system can be obtained by integrating the sedimentation profile [139, 140].

The sedimenting profiles of colloidal dispersions with hard sphere like interactions confined horizontally is compared using results from experiments, dynamical density functional theory (DDFT) and Brownian dynamics computer simulations [137]. This study reported the first measurements of sedimenting model colloidal dispersion where the gravitational length and particle diameter are in the same magnitude. In this work, the good agreement between the simulation and theoretical results indicated the accuracy of DDFT in describing the sedimentation of non-equilibrium hard sphere system in Brownian dynamics simulation. Additionally, other than the time scales mismatching between the theoretical and experimental results, the sedimentation profiles are similar. Strong layering at the bottom of the capillary was also found at longer time evolution where these layers were discovered to maintain structures similar in liquid state without any crystalline ordering.

The crystal-fluid interface resulting from the sedimentation of hard sphere colloids are reported in [133]. The sedimentation of the hard sphere colloids were achieved by slight density differences between the colloids and the solvents, and are away from sedimentation equilibrium. However, at the smallest density difference the interface is almost stationary so it was considered to be indicative of interface at equilibrium. The interfacial velocity (the speed of the interfacial moving upwards) appeared to be increasing as the solvent density difference increases. Presumably, this velocity is directly proportional to the sedimentation velocity, however, this was only observed in near-equilibrium system, where the density difference is the smallest. Furthermore, crystal-fluid interfaces broadens with increasing density mismatch while the crystal-fluid interface at close-to-equilibrium corresponds to simulation results where interfacial width of 7-8 particle diameters was yield in the simulation results. The crystal-fluid broadening observed when gravity is present was attributed to increasing number of crystallites nucleated in the fluid above the crystal surface. The work we present here are examples of sedimentation studies using hard sphere systems. In the following section, we will be discussing sedimentations in short-range attractive systems.

2.6.2 Sedimentation in attractive systems: Transient clusters

Attractive interparticle potential between particles can lead to aggregation of clusters. Deposition of the clusters then occurs at a length scale determined by the cluster size rather than the single particle size. The larger the cluster the faster the settling. The cluster size increases continuously as the clusters settle, and the rapid settling clusters"sweep up" the slower and smaller clusters as they sediment [115].

In [141], the sedimentation of a cluster increases linearly with the number of particles inside the cluster. The friction also increases with the expanding radius of gyration of the cluster where we could assume that sedimentation is rendered slow due to this reason but the influence of gravitational forces on the expanding cluster increases quicker than the effects of friction. Therefore, large clusters sediment more rapidly than smaller clusters. These effects contribute to the reasoning why at a constant ϕ , stronger attractive interactions increases the sedimentation velocity.

When the attractive interaction and the volume fraction are increased, a space filling network is formed leading to slower sedimentation velocity. In contrast to low ϕ where transient clusters formations are enhanced due to large voids between particles and increases the sedimentation velocity, sedimentation velocity is decreased due to smaller gaps for fluid flow at high ϕ. However, the ϕ range studied in this work is less than 10% where transient clusters are more likely to be formed than dynamically arrested branch networks.

2.6.3 Sedimentation in transient networks

It is worth to point out that we use the term “transient network” instead of “gel” which is broadly used in literature considering the various ways the term “gel” are defined in the literature. Often this is due to the various indirect ways the gel boundary is determined in experimental systems [119, 142, 143]. Thus, the discussion here mainly focuses on arrested networks. The colloid-rich solid-like network branches and the diffusive domains in a gel combined with the gravitational field acting on the gel contribute to the out of equilibrium state of sedimenting gels. Therefore, the only issue related to sedimenting of gels is the competing timescale between the two-factors.

In the early work describing the sedimentation of gels, a model based on poroelastic approach is used to explain the sedimentation of gel under gravity [115, 144]. The appearance of solvent channels which act as viscous shear forces due to the solvent flow leads to the deformation of the network. This was preceded by a latent period where the gradient of the collapse profile is near or almost zero. This initial stage is detailed due to the solvent flowing through the aggregated colloidal network at a very slow rate. Meanwhile, the onset of the collapse at the appearance of the channels are due to the increase of sedimentation velocity after the channels have “straightened up” [144]. In their work, Derec *et al.* proposed a model connecting the fracture caused by the channel appearance and the settling velocity of the arrested network [143].

The sedimentation of arrested network can be described by two well-established mechanisms: delayed or “accelerated” collapse, as described above, and creep sedimentation. Creep sedimentation is when the network compacts under its own weight. The factors differentiating these two mechanisms are the interparticle attractive strength and colloidal volume fraction [115, 119]. In addition, the same system may undergoes a period of creep before delayed collapse [119]. It has also been proposed that the sample size determines whether the system subjected to creep or delayed sedimentation [145].

Creep sedimentations mechanism is well described using poroelastic flow models [28, 146, 147]. At first, the compression of the network under gravitational stress works against fluid pressure from solvent inside the porous networks. Therefore, the rate of the compression is limited by the slow rate of the solvent flowing out of the network. After some time, the gravitational compression is limited by increasing elastic stress because of the network collapse. Previously, the two concepts were connected based on rheological concepts where accelerated collapse is related to failure and disruption of the gel network due to the compressional stress (applied or gravitational) is greater than the yield stress of the network. Apparently, when

the network is subject to stress larger than its yield stress there was a significant delay before it finally yield. But, the mechanism for the yielding was not discussed.

Stronger gels can be considered to be time independent but thermal rearrangement is faster in transient network where particle dynamic role in the delayed collapse needs to be addressed. Thermal activated rearrangements of the particles were identified as the cause to network ageing and ensuing collapse [148].

CHAPTER 3

Materials and Methods

This chapter starts by describing the materials used in the experiments and discusses the experiment techniques employed. Confocal microscopy plays a primary role as the imaging method for this project and this is put into detail in Section 3.2. Under this section, methods for obtaining optimum images are also discussed. Next, details about scanning electron microscopy are presented in Section 3.3 and sample preparations for imaging are detailed in the next Section 3.4. In order to attain structural information from the experimental samples, the location of the particles are required and this is explained in Section 3.5. Once the coordinates of the particles are achieved the structures are then analysed with several methods described in the last section of the chapter; Section 3.7.

3.1 Model systems

3.1.1 Polymethyl methacrylate particles in apolar solvents

The use of well-characterised colloidal particles in colloid physics is important for simple correlations and connections with theory and simulations. Some examples of well-defined colloidal models are polystyrene (PS), silica and polymethyl methacrylate (PMMA). In the study of the phase behaviour of hard-sphere colloids using PMMA particles by Pusey *et al.* [3, 149], the observed phase behaviour was similar to that expected for hard spheres which catalysed the development of the field. Additionally, the mixtures of PMMA and non adsorbing polystyrene polymer have been extensively investigated [18, 32, 91, 119, 150] and the phase behaviour is well-characterised as detailed previously in subsection 2.3.3.

For the work in this thesis, PMMA particles from more than one synthesis are used. Polyhydroxy stearic acid (PHSA) brushes are attached to the surface of the PMMA to stabilise the particles against aggregation. The particles are selected based on polydispersity and fluorescent dye. The particles were synthesised using methods in [88, 89] and cleaned using centrifugation and washing in hexane.

In Chapters 5 and 6, the PMMA particles are suspended only in cis decalin without adding another solvent for density matching. Meanwhile, in chapter 4 PMMA particles are suspended in a 76.5/23.5% w/w mixture of cyclohexyl bromide (CHB) and cis decalin with density of $\rho = 1.196\,\mathrm{g cm^{-3}}$. In order to screen charges and then obtain a similar interactions like in the hard sphere system, 4 mM tetrabutylammonium bromide (TBAB) is added to the CHB. This solvent mixture sufficiently matches the refractive index of PMMA to minimise the van der Waals interactions. For density matching, the solvent mass fractions are determined by repeatedly centrifuging the particles and adding drops of the solvent until there is no sedimentation observed after 15 mins centrifugation at 11 000 rpm.

3.1.2 Polystyrene as depletant

Linear polystyrene (PS) is used as the nonadsorbing polymer to induce the attractive interaction in the PMMA solution. The radius of gyration R_g and molecular weights M_w of each polymer used in this work is listed in Table 3.1. The radii of gyration R_g are initially estimated based on theta values from [151]. Since the solvent mixture for density and refractive index matching are good solvents for PS, the polymer coils are therefore in a swollen state. Determining the R_g of PS has been proven to be difficult with measurement errors typically around 10%. Therefore, we estimated our R_g by mapping it to the reduced second virial coefficient $B_2^* = -1.5$ at criticality which has been shown to be a more accurate way to determine R_g [94, 95]. The details of this mapping is given in the next subsection 3.1.3.

TABLE 3.1. A table of listing the details of polymethyl methacryate (PMMA), polystyrene (PS) polymers and solvents used in this work.

Chapters	PMMA diameter σ	Solvents	PS molecular weight M_w and radius of gyration R_g
Chap.4	1.4 μm ±4.0%	cis decalin + cyclohexyl bromide (CHB)	M_w= 30×10^6 g mol^{-1} and R_g = 203 nm
Chap.5	0.46 μm ±4.0%	cis decalin	$M_w = 3.46 \times 10^6$ g mol^{-1} and R_g = 67 nm
Chap. 6	1.0 μm ±4.6%	cis decalin	$M_w = 8.5 \times 10^6$ g mol^{-1} and R_g = 128 nm

3.1.3 Determination of radius of gyration and interaction potentials

We first constructed a phase diagram of the colloid-polymer systems using the polymer volume fractions in reservoir as ordinates and the colloid volume fractions as the x-axis. This was done by preparing colloid-polymer mixtures with various amount of polymer added to colloidal suspensions of about 20% volume fractions. A number of colloid-polymer mixture are prepared by adding more polymer to 20% of colloidal suspensions. A series of data point with increasing amount of polymer are observed using confocal microscope. As the amount of polymer increased, fluid diffusivity started to slow down and eventually formed a gel. A spinodal line is then sketched separating the fluid and gel phases. The criticality is determined by varying the R_g so that the reduced second virial coefficient B_2^* is equal to -1.5 at criticality (based on the extended law of corresponding states). In this case, the R_g values are found to be within 10% range compared to R_g obtained from the literature [151].

Based on the estimated R_g, the interaction potentials are then calculated using the Asakura-Oosawa equation, given as:

$$u_{\mathrm{AO}}(r) = \begin{cases} \infty & \text{for } r < \sigma \\ -\frac{k_{\mathrm{B}}T\pi(2R_{\mathrm{g}})^3 z_{\mathrm{p}}}{6}\frac{(1+q)^3}{q^3} & \\ \times\left[1 - \frac{3r}{2(1+q)\sigma} + \frac{r^3}{2(1+q)^3\sigma^3}\right] & \text{for } \sigma \le r < \sigma + \sigma_{\mathrm{p}} \\ 0 & \text{for } r \ge \sigma + \sigma_{\mathrm{p}} \end{cases} \tag{3.1}$$

where the fugacity z_{p} is equal to the number density ρ_p of ideal polymers in a reservoir at the same chemical potential as the colloid-polymer mixture. The result is an effective interaction between the colloids of range $q\sigma$ and well-depth $u_{\mathrm{AO}}^{\mathrm{min}}$. For our parameters, Eq. 3.1 is expected to be highly accurate. The interaction strength of the effective colloid-colloid is expressed using the well depth:

$$u_{\mathrm{AO}}(\sigma) = u_{\mathrm{AO}}^{\mathrm{min}} = q^2 k_{\mathrm{B}} T \rho_{\mathrm{p}} \sigma^3 \frac{\pi(3+2q)}{12} \tag{3.2}$$

3.1.4 Preparing colloid-polymer samples

Experimental samples are mixed from either dry or wet colloids. Starting from wet colloids immersed in cis decalin centrifugation results on a sediment pellet consisting of PMMA colloids with cis decalin as supernatant. The supernatant is then removed. The resulting sediment is assumed to be at a volume fraction ϕ_{sed} $\approx$ 0.64; the volume fraction at random close packing, ϕ_{rcp} and this sediment can

then be diluted to make colloid-polymer mixture samples of known volume fraction. The validity of $\phi_{\mathrm{rcp}} \approx 0.64$ remains debatable due to the inconsistencies of ϕ_{rcp} from different protocols [152]. Also, it was shown in a silica colloid system that different areas of the centrifuged sediment have different concentrations varying between 0.60 and 0.64 [153]. However, the centrifuge method is convenient and is a consistent protocol that generate a series of sample with concentrations normalised by the same volume fraction of sediment ϕ_{sed} [154]. For samples using dry PMMA colloids, the mass of dry PMMA is weighed and cis decalin is added to a pre-calculated mass in order to obtain the desired ϕ before adding PS solution. In the case of density matched colloid-polymer samples like our work in Chapter 4, a solvent mixture of cis decalin and cyclo hexyl bromide (CHB) containing 4mM TBAB salt is used instead of cis decalin solvent.

Colloid-polymer samples are prepared as followed. Firstly, a stock solution of PS in cis decalin is made by adding PS into the solvent and left to dissolve on rollers at 40 rpm for at least 24 hours. Then, the required ϕ is obtained by adding solvent to the wet or weighed dry PMMA particles. The sample is vortexed throughly before adding PS solution to prevent PS branches from breaking in the vortex process. The details of PMMA particles, PS polymers and solvents used in this work are listed in Table 3.1.

3.2 Confocal microscopy

The confocal microscope principle was invented by Marvin Minsky in 1957. The motivation behind this was the need to obtain images from thick samples while reducing obscured information from the surrounding focal point. Light is focused onto a specific level of the sample through a small aperture at one time, avoiding undesired scattered light when the whole sample is illuminated all at once. The radiation property of fluorescent substance is presented in the next section followed by a brief discussion of the principle of confocal microscopy.

3.2.1 Fluoresence

Fluorophore dyes are added into the PMMA particles used in this work, which can produce fluorescence when stimulated. When a fluorescent molecule is excited its electron jumps to a higher energy level. This generally occurs when the molecule absorbs a photon of high energy with the correct wavelength. The electron then drops to a lower energy level when the fluorescent molecule loses some of the absorbed energy from collisions with other surrounding molecules. Then, the electron relaxes further and returns to the ground state releasing a photon with lower energy

than the above-mentioned absorbed energy. The electronic states of a fluorescent molecule is illustrated in Fig. 3.1. The exact colour of emitted light is independent of the absorbed light and dependent of the vibrational levels of the molecules. In this work we employed PMMA particles dyed with rhodamine in chaper 4 and 1,1 dioctyadecyl-3,3,3,3-tetra methyl indocarbocyanine ($DILC_{18}$) as fluorophores for PMMA particles in Chapters 5 and 6.

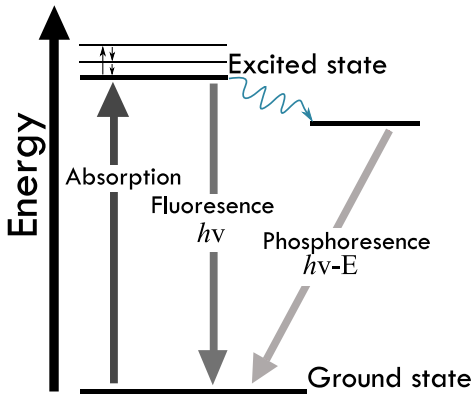

FIGURE 3.1. A Jablonski diagram showing the electronic states of a fluorescent molecule.

3.2.2 The confocal microscopy principle

Specific point illumination on the sample and rejection out of focus light are the two primary ideas behind laser scanning confocal microscope (LSCM) [156, 157]. The basic optical path of confocal microscopy is illustrated in Fig. 3.2. The illumination source is focussed on a point on the specimen plane through a pinhole, shown in the figure as P1 and an objective lens. A second objective similar to the first, projects an image of the spot illuminated area onto another pinhole, P2 in the figure, which is in the conjugate plane as the illuminated spot. The term confocal originated from the conjugate focal planes of P1, point spot on the sample and P2. The second pinhole rejects out of focus light preventing it from reaching the detector. A detector behind the second pinhole recognises the intensity of light passing through the pinhole converts it to an electrical signal.

For a single point on the sample specimen to be in focus, it needs to be scanned in order to produce an image. Also, since only a single point is illuminated to produce an image at a time, the resulting total intensity is very low. This can be overcome by using a laser light source to increase the intensity of each illuminated point (an in turn the rate of scanning as well) like in confocal laser scanning microscope (CLSM).

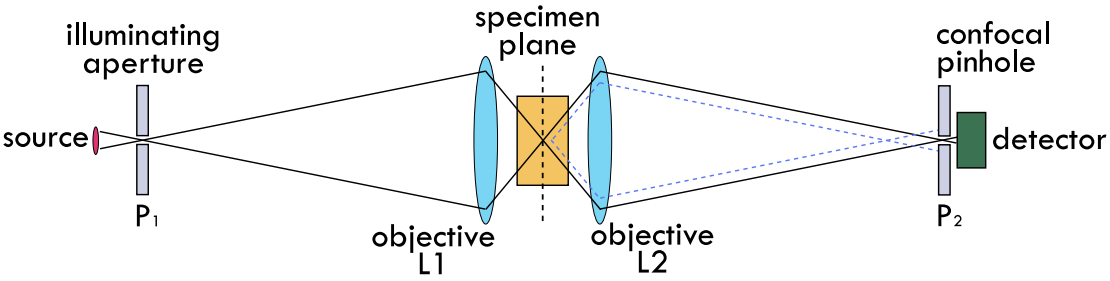

FIGURE 3.2. The basic principle of confocal microscopy is shown here. Point focused light is illuminated onto the sample by the condenser lens. All out of focus light is rejected at the confocal pinhole shown as dotted lines. Adapted from [155].

In its implementation, it is rare that the confocal microscopy setup is as shown in figure 3.2. In contrast, *epi*-illumination as described in Fig. 3.3 is used instead. In this Fig. 3.3 setup, the two objective lenses in Fig. 3.2 are replaced by a single objective lens. A dichroic mirror guides the laser light (blue line) to the direction of a pair of mirrors. These mirrors scan the light in the x and y directions. The light excites the sample (which contains fluorescent dye) after passing through the microscope objective. The red line represents the fluoresced light of the sample which goes back to the objective and is descanned by the same pair of mirrors that scanned the sample. Then, the longer wavelength light goes through the dichroic mirror through a pinhole that is in the conjugate focal plane of the sample. Here, at the pinhole light from outside the confocal plane of the sample is rejected. Finally, the light from the pinhole is measured and converted into a voltage by a detector: e.g. a photomultiplier tube. A series of images recorded at different depths along the z-axis of the microscope construct a "stack" of images within the computer memory. The image stack can be combined using image processing software to produce a 3-dimensional (3d) image of the specimen. This feature is utilised in the cluster analysis in chapter 4.

3.2.3 Resolution

Resolution is the ability to discern two-close together objects in an image. Similar to conventional microscopy, the resolution of confocal microscopy is limited due to diffraction. A so-called Airy disk is produced when a small amount of light produced from a small point source on the specimen collected by the objective and then focused at a relative point in the image plane. Instead of the objective lens focusing the produced light to a very small point in the image plane, the merging light

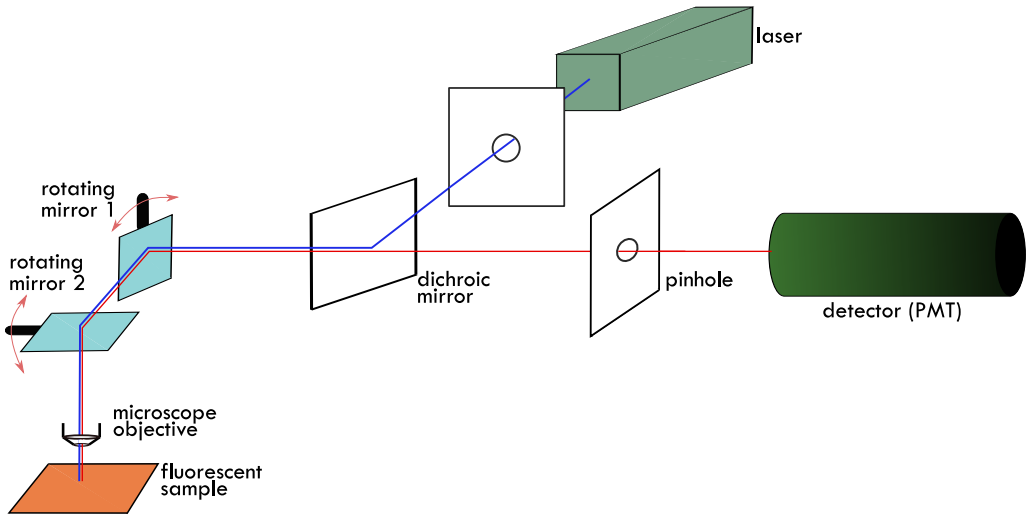

FIGURE 3.3. A schematic diagram of the inner mechanism of laser scanning confocal microscope (LSCM). The diagram is adapted from [6].

waves interfere at the focal point forming a diffraction pattern. This is the Airy disk; a diffraction pattern resulted from light passing through perfect lens with a bright circular disk in the middle and less intense circular rings surrounding it when observed in x and y. An image of Airy disk is shown in Fig. 3.4. However, the diameter of the Airy disk is determined by the numerical aperture of the objective lens as well as the wavelength of the laser source [155, 157, 158].

The maximum resolution of the microscope is restricted by the Airy disk based on the Rayleigh criterion. Based on this criterion, two objects are considered resolved when it is separated in by their Airy disk radius. For most confocal microscope this limit is around 200 nm.

The point spread function (PSF) is a 3d diffraction pattern of a point object under the microscope from light emission. The intensity pattern for the point spread function (PSF) on the image plane is similar to the intensity pattern for an Airy disk where it abates away from the centre in x and y and the intensity also drops in the z-axial direction. Ascribing to the limitation in the optics, the decrease of intensity is slower in the z direction causing the z resolution to be poorer than in x or y where the maximum is reported to be around 500 nm [155, 157, 158].

Deconvolution

The process for image formation in confocal microscopy follows the assumption that it is linear and shift invariant. Linearity is met when the sum of images of two distinct objects is the same to the images of the combined objects. The image of a point object is the same from anywhere in the field of view when the process is shift invariant. The optical image of a specimen is connected to the specimen

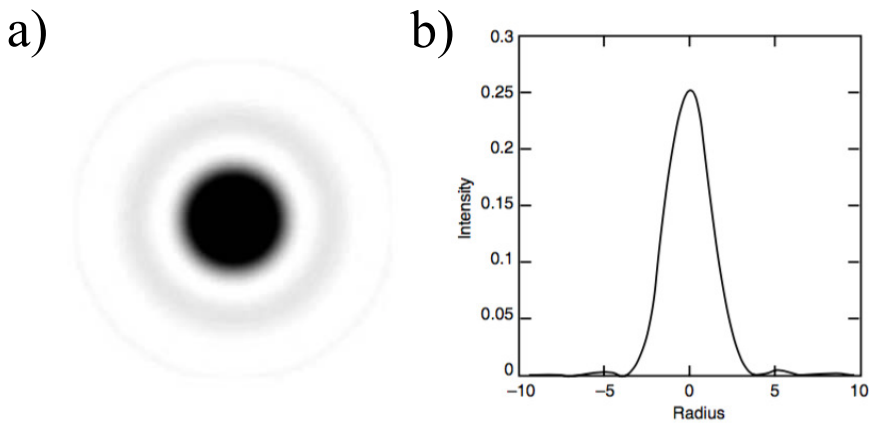

FIGURE 3.4. Figure shows a) an image Airy disk with the black and white inverted to emphasis on the secondary peak seen as the outer ring and b) a curved graph showing the change intensity with radius. Figure reproduced from [159].

mathematically by convolution where in the image plane a blurred image of the object corresponds to each point of the specimen. Thus, an optical image, g is made of the sum of each PSF h multiplied by a function of light intensity emitted from corresponding point object f which can be given as:

$$g(r) = f(r) \bigotimes h(r) = \int_{-\infty}^{\infty} f(s)h(r-s)ds \tag{3.3}$$

where the image g, object f and PSF h are represented as functions of position (r). Based on the convolution theorem, the Fourier transform (FT) of a convolution of two functions is the product of the individual FT of the functions:

$$G(S) = F(S)H(S) \tag{3.4}$$

where $G(S)$, $F(S)$ and $H(S)$ are the FT of $g(r)$, $f(r)$ and $h(r)$ respectively. Although it seems like undegraded object function F can be obtained by just dividing G/H in reality it is not straightforward as that. There are regions of in which $H(S)$ becomes very small or zero and there is noise component which needs to be considered. Dividing by a small component will amplify the noise further resulting to errors in the final reconstruction. So the equation that describes the blurred image in real space needs to include the noise component ϵ where the blurred image is now called k and given as:

$$k(r) = f(r) \bigotimes h(r) + \epsilon \tag{3.5}$$

The deconvolution process inverts the effect of the PSF on the specimen whereby the blurring due to PSF can be removed notably deeper in z direction where worst

blurring usually occurs. There are different deconvolution algorithms and different ways to calculate the noise term in Eq. 3.5. In the work described in chapter 4, the confocal images were deconvolved using the commercial software, Huygens (SVI, Netherlands) which carries several different deconvolution algorithms. The PSFs were theoretically calculated by Huygens software.

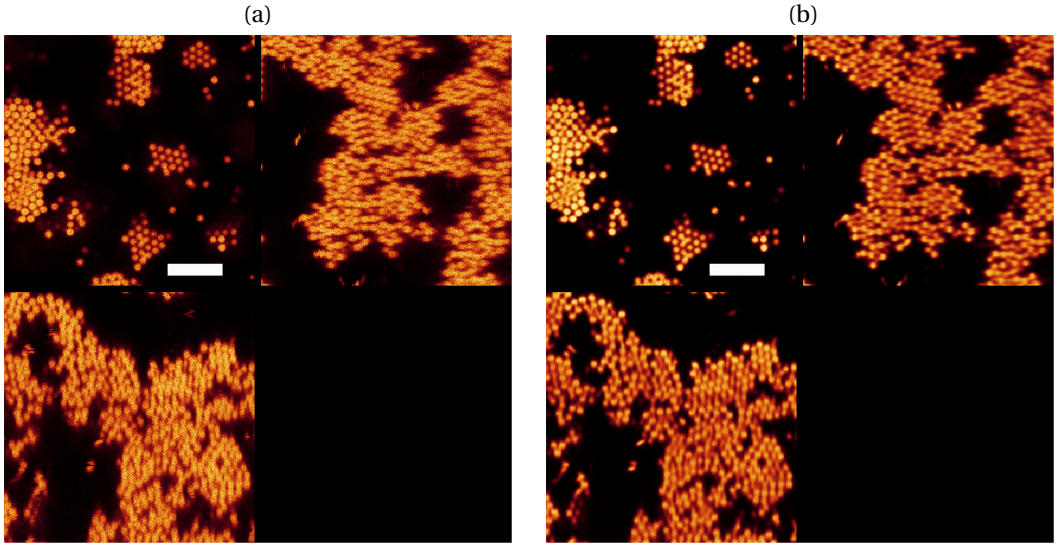

FIGURE 3.5. (a) Figure showing a xyz of $344 \times 344 \times$ image before deconvolution (b) the same xyz image after deconvolution. Scale bars represent 10 μm.

3.3 Scanning electron microscopy

In scanning electron microscope (SEM) the specimen surface is irradiated with a focused electron beam. The accelerated electron probe is scanned across the surface sample inducing secondary electron emission from the surface. The topography of the specimen surface is observed by two-dimensional scanning probe and the image is obtained from secondary electrons [160].

3.3.1 The SEM microscope

For our work, we used a JEOL JSM 5600 LV electron microscope to determine the diameter and polydispersity of PMMA colloids for our experiments. The microscope is operational either in high or partial vacuum mode ($10 - 10^{-4}$ Pa), in accelerating voltage of $1 - 30$ keV. The working distance has the range between 5 mm and 40 mm; adjusted according to the resolution required where a short working distance gives

higher resolution. The emitted electrons are detected with a Everhart-Thornley scintillator.

3.4 Sample preparation for observation using microscopes

3.4.1 SEM Sample

A small amount of dilute PMMA in hexane solution is deposited on the surface of a metal stub that fits into an SEM sample holder. This drop of solution is left to dry by allowing the hexane solvent to evaporate completely. Preferably, the dried sample forms a single layer of particles on the metal stub as is shown in Fig. 3.6 (a). Then, 15 nm of conducting layer of silver or gold is sputtered onto the sample to avoid accumulation of charge on the non-conducting sample. However, the stabilising hairs of PMMA particles collapse in when particles are in dry condition. Therefore the diameter size measured using this method is taken to be the core diameter [154]. The size distribution of the PMMA particles used in Chapter 4 and 6 is shown in Fig. 3.6 (b).

3.4.2 Confocal Sample

There are two ways in which we prepared our samples for the confocal microscopes. The first method, adapted for our work in Chapter 5, the PMMA+PS sample is placed into borosilicate glass rectangular capillaries. The internal dimensions of this capillaries are $0.10 \times 1.00 \times 50$ mm with glass thickness 0.10 mm. After loading

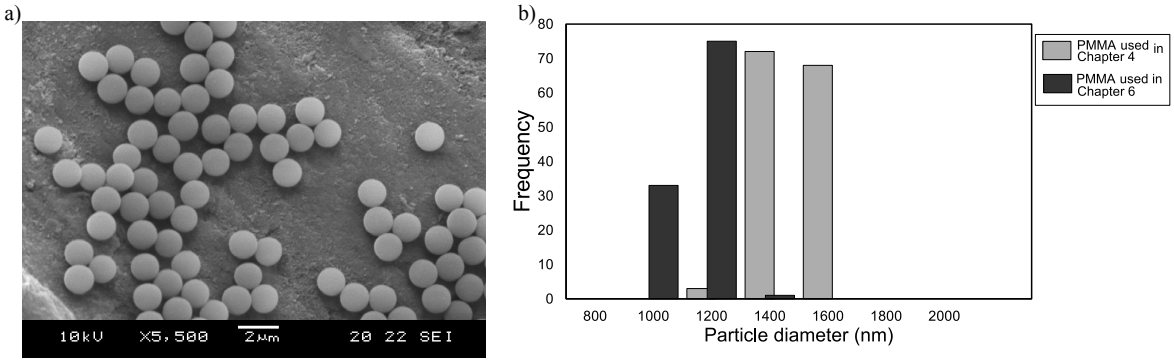

FIGURE 3.6. (a) An image of PMMA particles (used in Chapter 4) taken using scanning electron microscope (SEM) and (b) the size distribution of the PMMA particles used in Chapters 4 and 6.

the sample, the capillary is sealed at both ends using epoxy glue in order to prevent evaporation. This is illustrated in Fig. 3.7(a). The second method is creating cells using microscope coverslips as was done for experiments in Chapters 4 and 6. For this purpose, thin microscope coverslips are mounted side-by-side on a standard microscope glass slide forming a 8 – 10 mm space between the coverslips. Next, the space is then closed by placing another coverslip on it and the left and right edges are glued on the previously fixed coverslips. This creates a cell for the sample as is shown in Fig. 3.7(b). Finally, the cell is sealed with epoxy glue once the sample is pipetted into it.

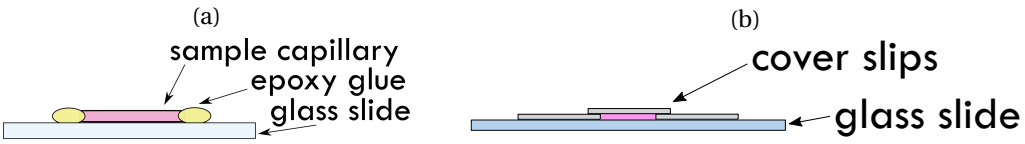

FIGURE 3.7. A sketch of the 2 types of capillary used in this work (a) Borosilicate capillary with inner dimension of $0.1 \times 1 \times 50$mm and (b) custom made cell where the pink shaded areas represent the colloid-polymer sample in the cells.

3.5 Particle tracking

The information obtained from the confocal images is characterised by analysing the images using algorithms which have been previously discussed in detail [9, 161, 162]. A modified version of IDL routines written by Weeks, Crocker and Grier are used for particle tracking in this work. The details of the algorithm are given below. Although the algorithm was written for optical microscopy originally, it has been improved for speed, precision and for tracking dense and dynamically heterogenous systems [9, 161, 163].

The basic assumptions of the algorithm are the particles are spherical and that the maximum local brightness represents the centre of the particle. The algorithm detects the local intensity maxima within the image of the particle that is comparable to the size of the particle. This is taken as the trial centre; a possible location for the particle. A trial centre is chosen when there is no brighter pixel within a set distance. This way of choosing the trial centre is continued to the pixel's immediate surrounding area, eliminating overlapping spheres and reduces the possibility of duplicate candidate sites. This trial centre is presumed to be close to the spherical geometric centres particle based on the preliminary steps given. Ideally, the brightest local maxima would be the pixel that is in the middle of the particle image as

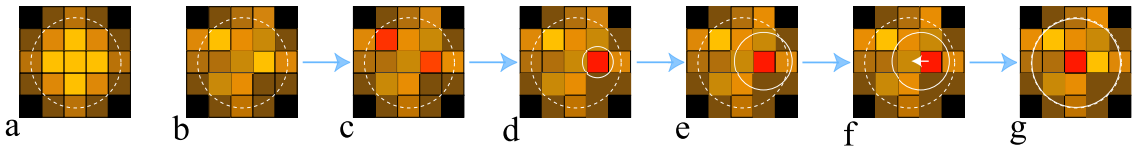

FIGURE 3.8. A series of images showing the range of pixel intensity usually obtained from confocal microscopy. Starting from an ideal image in (a) with the highest intensity in the centre. Considering the centroid of an increasing cell repeatedly lead to the identified centre moved to the centre of the object. Adapted from [73].

shown in Fig.3.8(a). The circle with dashed white line represent the set distance of the trial centre which corresponds to the size of the particle. However, multiple local maxima could occur within the image of a particle that are not in the centre. This is illustrated in Fig.3.8(b) and highlighted in Fig. 3.8(c). The brightest pixel was found like in Fig. 3.8(d) and was taken as the initial point to decide the next centroid of the nearest pixels which gives another estimation for the geometric centre of the particle. This process was perform repeatedly until it reaches the radius of the particle where in this work the minimum pixels for a radius are 5 xy pixels, as is illustrated in Fig.3.8(d-g). Finally, after a number of iterations, the geometric centre of the particle is determined Fig. 3.8(g). Iteratively measuring the pixel intensities within the dashed circle allows better estimation for the particle coordinates, R as given by Crocker and Grier (1995) [162]:

$$R = \frac{\sum_i I_i r_i}{\sum_i I_i} \tag{3.6}$$

where r_i is the coordinate and I_i is the intensity of the ith pixel.

Pre-processing of the raw microscope image was also carried out in order to improve accuracy. Single-pixel detector noise can sometimes be misinterpret as the particle centre. Therefore, noise need to be filtered out from the confocal images before using the algorithm for particle tracking. For example, deconvolution process was carried out for the confocal images in Chapter 4. This process has been explained in Section 3.2.3.

3.6 Simulation

In Chapters 4 and 5, we compare our experimental work with results from simulation. Simulation in the chapters were done by Dr. Francesco Turci (Chapter 4) and Dr. Christopher Fullerton (Chapter 5).

In both chapters, the motion of the particles in the solvent is described using Brownian dynamics or overdamped Langevin dynamics using LAMMPS package [164]. Langevin dynamics mimic the Brownian motion of a mesoscopic particles diffusing in a solvent, replacing the molecules of the solvent as stochastic force. The movement of the colloidal particle in a solvent is given the Newton equation of motion for the particle:

$$m\frac{\mathrm{d}v(t)}{\mathrm{d}t} = F(t) \tag{3.7}$$

where $F(t)$ is the total force at time t and is given as:

$$F(t) = -\nabla_i V - \gamma v_i + \sqrt{2\gamma k_B T \xi_i} \tag{3.8}$$

where $-\gamma v_i$ is the frictional force of the particle moving through the solvent, $\sqrt{2\gamma k_B T \xi_i}$ is the random force (or the Brownian force) resulting from random collisions of the particle and solvent and $-\nabla_i V$ is the force from interparticle interaction potentials. Therefore, the evolution of velocities in time can be expressed as below where the position of particles and velocities are considered as r_i and v_i respectively:

$$m\frac{\mathrm{d}}{\mathrm{d}t}v_i = -\nabla_i V - \gamma v_i + \sqrt{2\gamma k_B T \xi_i} \tag{3.9}$$

where V is the total potential energy while γ is a friction constant and ξ a random noise force. The natural time unit is considered as τ_0. The damping time for Langevin dynamics is given as $\tau_0 = 0.1$. The integration time steps = 0.001 τ_0 where 420 steps corresponding to a single Brownian time.

3.6.1 Mapping interaction strengths between experiment and simulation

The Morse potential, shown in Eq. 3.10 was used to substitute the AO potential between the colloids. It was previously shown that this potential accurately replicate the behaviour of the AO system, including its higher-order local structure [12]. The continuous form of the Morse potential; unlike the AO potential, makes it convenient for simulation.

$$u_{\mathrm{mor}}(r) = \varepsilon_{\mathrm{mor}} \mathrm{e}^{-2\rho_0(r-\sigma_{ij})} - 2\mathrm{e}^{-\rho_0(r-\sigma_{ij})} \tag{3.10}$$

where $\varepsilon_{\mathrm{mor}}$ is the potential well-depth, ρ_0 is the attraction range and σ_{ij} is the minimum of the interaction between particles of i and j species. According to previous study [12] ρ_0 can be taken as $\rho_0 = 25.0/\bar{\sigma}$.

The state points between the Morse potential used in simulation and the (approximate) Asakura-Oosawa interactions within the experiment were matched

based on the extended law of corresponding states introduced by Noro and Frenkel [123], as was described in Chapter 2 Section 2.5. To map the state points between simulations and experiments, identical well-depths and reduced second virial coefficients B_2^* are required. B_2^* is defined in Eq. 3.11.

$$B_2^* = \frac{B_2}{\frac{2}{3}\pi\sigma_{\text{eff}}^3}. \tag{3.11}$$

Here $B_2 = 2\pi\int_0^\infty [1-\exp(-\beta U(r))]r^2\,\mathrm{d}r$ is the second virial coefficient and σ_{eff} is the effective diameter of a particle [165].

For the AO potential, σ_{eff} is equal to σ. While for the Morse potential (as given in Eq. 3.10), the effective diameter is fractionally smaller than σ, but this effect is very small for our parameters (around 1% of the diameter) therefore is neglected.

For the simulation results reported in this work, the value of B_2^* that is associated with the relevant Morse potential is calculated. Then, we calculated the well-depth that would give the same value of B_2^* for an AO potential with corresponding size ratios of polymer-colloid radii q. In the following chapters, simulation results are labeled by these effective AO well-depths, which are indicated by u_{AO}^{min}. These effective well-depths are different from the well-depths ϵ_{mor} of the Morse potential but are comparable based on the aforementioned method.

3.7 Structural analysis

To start our structural analysis, we first consider a two-point correlation using pair correlation function $g(r)$. Next, we conducted a higher order analysis for the full changes occurring in the colloidal gel system. The higher order analysis techniques are given following the description of two-point correlation method.

3.7.1 Pair correlation function

The pair correlation function or radial distribution function $g(r)$ in a system of particles is a method quantifying the density changes from a reference particle in terms of distance r. It can be used as a measure of the probability of finding a particle at distance r from the reference particle. Pair correlation function can be calculated using the distance between all the particles and represent the calculation into a histogram. The histogram is then normalised with respect to an ideal gas in which the particle histograms are uncorrelated.

For the calculation of the pair correlation function from real-space particle coordinate as in our work described in Chapter 4, a concentric shell of δr thickness is taken around each particle. The number of particle centres $n(r)$ that are present

in this shell is determined. The particle density in the shell can then be calculated by considering the volume of the shell $4\pi r^2\delta r$. The density (a function of r) , is then normalised using the equivalent density for an ideal gas ρ, resulting to the pair correlation function $g(r)$, given as:

$$g(r) = (1/\rho)n(r)4\pi r^2\delta r \tag{3.12}$$

This method is shown in Fig. 3.9 is used to consider $g(r)$. In the figure, a suspension of hard spheres particles of σ diameter is illustrated. Hard sphere cannot overlap therefore there is zero probability of finding a particle at distance r<σ. Then, there is a jump at $r = \sigma$ signalling the first peak occurs at σ and this peak corresponds to the first layer of particles surrounding a reference particles, and the same interpretation continues in the next peaks. The peaks decrease as r increases due to the lack of long range order. In the dilute limit, the relationship between $g(r)$ and the interaction potential $u(r)$ can be given as:

$$g(r) = \exp(-\beta u(r)) \tag{3.13}$$

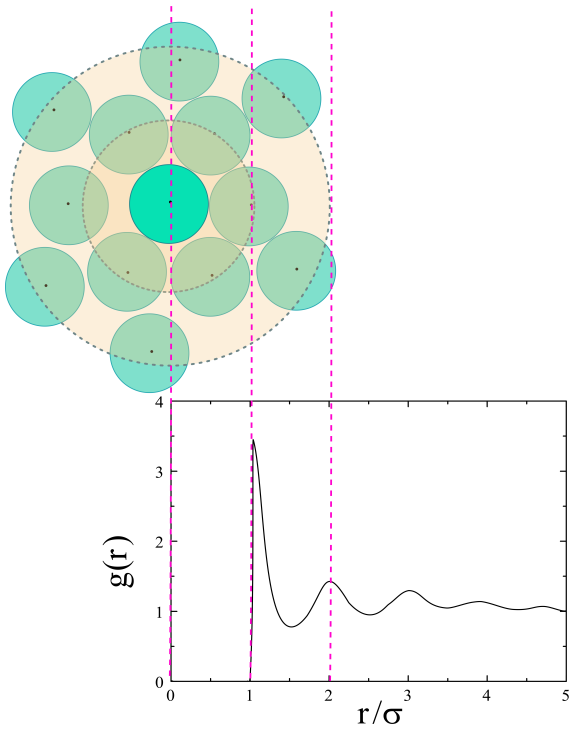

FIGURE 3.9. A suspension of hard spheres with corresponding $g(r)$. Here r is the distance from the centre of a reference particle shown in the illustration as the central particle.

where $\beta = 1/k_B T$ [71, 94]. This has been used previously to measure colloidal interaction directly using real-space analysis in several studies and has been shown to work well at modest volume fraction $\phi \sim 0.05$ [94, 166].

3.7.2 Topological cluster classification (TCC)

The topological cluster classification (TCC) algorithm is an analysis method for identification of local structures. The basic concept of TCC is built on an idea proposed by Frank in 1952 [167]. In the seminal paper, it was proposed that a liquid system undergoing cooling to below its melting temperature, the atomic level arrangements of atoms within the liquid determine its ability to freeze when supercooled.

In order to demonstrate this, 13 particles in isolation forming minimum energy clusters were used as an example. When the particles are arranged into a regular icosahedron, a cluster with lower free energy as compared to compact FCC or HCP crystal clusters formed from the 13 particles. Therefore, it was concluded that icosahedral formations would be more likely than the FCC and HCP arrangements in supercooled liquid [168].

The TCC algorithm follows the consideration made in 1952 where minimum clusters of 13 particles are used as an example, extending the idea to minimum energy clusters of other numbers of particles and different interaction potentials [169]. The algorithm locates clusters of n particles which are topologically equivalent to the minimum energy structure for n particles which are considered in isolation. The TCC are able to locate the structure based on a database of candidate structures which includes the clusters in the ground state for the Morse potential for all values of the interaction range ρ_0. In the database there are also the previously mentioned clusters of 13 particle packings consisting of a central particle and 12 nearest neighbours which correspond to the pieces of FCC and HCP bulk crystal structures.

The initial stage of the TCC analysis is identification of the first nearest neighbours of each particle using the modified Voronoi decomposition method. The system is divided into regions comprising of a single particle and all the closest points to it in space. Two particles are considered as neighbours only when their Voronoi regions share a face *and* a line that connect the particles' centres. The line would intersect the face which is illustrated in Fig. 3.10. These two particles must also be separated by a distance shorter than some threshold or cut-off r_c which we set to be 1.4σ. It has been shown that this cut-off value is large enough to record any significant bond network [10]. It was only when these conditions are fulfilled that these particles are assigned as nearest neighbours, or bonded.

In the next stage, three, four and five-membered shortest-path rings in the bond network are located. The shortest-path ring is determined from the shortest possible path connecting the particles inside the ring-bonds without a possibility of a shortcut to shorten the ring [170]. The detection of four-membered rings are often hindered due to thermal fluctuations inherent in the system. These four-membered rings are substructures in detecting octahedra and crystal packings. A perfectly square arrangement drifted to a rhomboid arrangement can prompt formation of an additional bond formed across the centre of the four-membered ring connecting two opposite vertices. Therefore, a modification that allows a certain amount of asymmetry in a four-membered ring before a further bond is identified across the ring, dividing it into two three-membered rings is introduced as was proposed in [171]. In our work, a dimensionless parameter f_c with the value of 0.85 is used to address this issue. The choice of $f_c = 0.85$ value is based on previous work that used similar colloid-polymer model [10].

In the final step, a hierarchical approach is adopted by the algorithm in identifying clusters that corresponds to those in the database. A number of basic clusters are located first. These basic clusters are made of a shortest-path ring where all the ring's particles share up to two common nearest neighbours. Spindle particles are

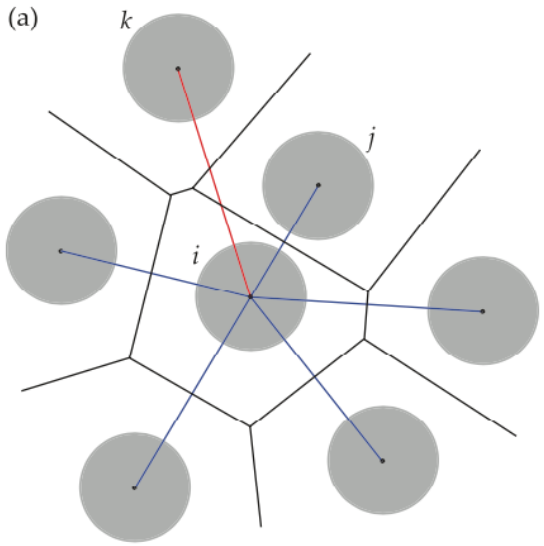

FIGURE 3.10. Particles are considered neighbour when their Voronoi regions share a face and a line connecting the particles' centres intersects the shared face. The intersecting lines are shown in blue line. However, the red line demonstrates the eliminating neighbours condition that while particle i and k shares a face, the line connecting their centres does not intersect with the shared face. Figure is adapted from [10].

not required to be bonded to one another but are otherwise bonded to all particles in the ring. These basic structures are compatible to pieces of larger cluster struc-

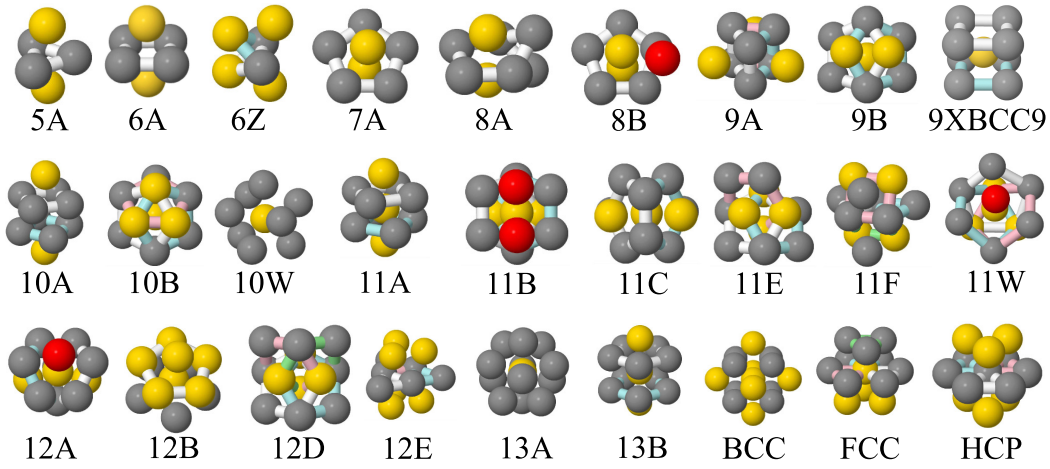

FIGURE 3.11. A diagram of clusters identified using the topological cluster classification (TCC). Adapted from [172].

tures and also correspond to smaller local favoured structures. Therefore, a series of detection routines are carried out in order to classify the larger compound clusters from the basic clusters. The ensuing result of identifying the local structures using the TCC is that each particle belongs to multiple structures. Here, a particle is linked with only the largest structure from among the multiple structures it belongs to. This is shown in the form of fraction, N_c/N where N_c is the number of clusters and N is the total number of particles detected using the particle tracking. TCC results are presented in Chapters 4 and 5.

In our work, we focused on specific clusters shown in Fig. 3.11. These clusters are identified as ground state clusters formed by systems with short-ranged Morse potential [169] which are applicable to colloid-polymer mixtures. The basic principle of comparing these structures originated from the Noro and Frenkel work [123] then further studied by Lu *et al.* [173] where the structures in the attractive systems are not dictated by their potentials.

3.7.3 Common neighbour analysis (CNA)

Common neighbour analysis (CNA) was first introduced to analyse the melting and freezing of Lennard-Jones clusters [174]. This method recognises particles shared by a pair of particles called the root-pair. The root-pair might or might not be bonded to one another. Four integers are used to characterise the common neighbour analysis where the first integer indicates whether the root-pair is bonded or not.

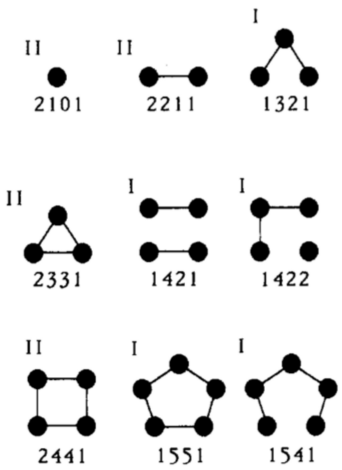

FIGURE 3.12. A diagram of common neighbour analysis showing clusters typically seen in dense atomic systems. Black circles are representative of common neighbours shared by a pair of particles (not shown in the diagram). Figure is adapted from [174].

The number 1 is used if the root-pair particles are bonded and number 2 is used if they are not. Then, the second integer is the number of particles shared by the root-pair. The third integer represents the number of bonds between the neighbouring particles and lastly, the fourth integer indicates specific diagram when the first three integers are insufficient in characterising the particles. An example of these four integers are shown in Fig. 3.12, where the shared particle are represented in black circles and the root-pair is not shown. This analysis is carried out in Chapter 5 to identify crystallinity in local structures of the sedimenting gel.

3.7.4 Bond order parameter ψ_6

This was first introduced to study the local orientational symmetry in simulations of supercooled liquids and models of metallic glasses [131, 175], bond order parameters have been widely used to study various types of systems. Other than the original application that is to study the structural ordering in supercooled liquids bond order parameters have been used to examine structure at interfaces [176] and in model atomic clusters [177]. Most strikingly, bond order parameters can be applied in the crystallisation research for structural analysis [25, 106, 107]. It has been shown that bond order parameters are useful for detecting the crystallinity of a system, although not sensitive to possible different types of crystalline ordering [107].

In Chapter 6, bond order parameters are used to represent the degree of crystallinity in the system. This was carried out by considering the local crystallinity

bond orientational order parameter ψ_6 for particle j using the following equation.

$$\psi_6^j = \left| \frac{1}{z_j} \sum_{m=1}^{z_j} \exp(i6\theta_m^j) \right| \tag{3.14}$$

where z_j is the number of neighbouring particles for particle j, m is used to label the neighbours and θ_m^j is the angle formed between the bond connecting particles j and m and a reference axis. The average of ψ_6^j over all frames of images acquired gives the ψ_6 of internal structures and this is given as:

$$\psi_6 = \langle \frac{1}{N} \sum_{j=1}^{N} \psi_6^j \rangle \tag{3.15}$$

where $\langle \cdots \rangle$ represents the time average. The ψ_6^j value ranges between 0-1 where 1 represents perfect crystalline ordering around particle j, while lower values represent weaker magnitude of local crystalline ordering. This is used to evaluate the degree of crystallisation after the colloid-polymer gel samples are put under temperature cycling in Chapter 6.

3.8 Summary

The preparation of colloid-polymer mixtures, starting with the determination of the radius of gyration of the polymers used is presented and discussed. We have also described the principles of confocal microscopy and size characterisation using scanning electron microscopy. Using the information from particle tracking, we then described the structural analysis methods. The pair correlation function is the most common way of describing the density distribution of the system. However, this result lacks some structural information at particle level. To address this, we consider higher order structural analysis, the topological cluster classification and common neighbour analysis both gives local favourite structural information. The topological cluster classification is based on complete crystalline cluster whereas common neighbour analysis could detect a crystalline precursor. Finally, bond order parameter measurement is used in the analysis of 2d data shown in Chapter 6.

CHAPTER 4

Crystallisation in colloidal gels: a particle-resolved analysis

In this work, I describe experiments on the 3d structural evolution of colloid polymer system. The goal of the experiments is to understand the assembly processes leading to crystallisation using a higher-order method of detecting the structural changes as function of time.

The motivation of this work is due to the self-assembly puzzle that has long been the interest of the scientific community. Self assembly is the organising of components into a predetermined pattern or structure without human intervention. This process is evident in nature and technology; for example in the assembly of viral capsids [36, 37], crystalisation [27, 38, 39] and has potential in a range of applications like photonics [40]. In recent years, there have been developments in the synthesis of particles with controllable interactions [48, 50, 98], where an ordered phase of these particles were reported [51–54].

During the dynamical self assembly process, the formation of disordered aggregates often disrupts the formation of a stable ordered phase. However, it is not always clear whether the source of this disruption is caused by thermodynamics or kinetics [55]. Although kinetic traps are not reported in the the classical theories of phase transition [56] these traps are often encountered in experiments on colloids [32, 57, 58, 95, 117, 178–182]. For a short range attractive interaction system undergoing crystallisation, it was discussed that in order to avoid the ineffective self assembly, a small optimum range of attractive interaction is required where bond reversibility is possible to remove any defects during assembly [37, 39, 58, 96, 105]. This led to the idea that further optimisation could be achieved by changing the degree of attraction during self assembly process. This optimisation work has been

done in simulation [1, 183] and realised in experiments by careful parameterised to the square well [95]. In this work, we follow the structural evolution of instantaneous quenched system for later comparison to controlled quenching in the temperature controlled colloid polymer system in Chapter 6. Quenching is the most efficient when it is done on a time scale shorter than the colloidal relaxation so that phase separation does not occur. Instantaneous quenches are impossible in molecular systems. The dynamics of such systems are usually too fast that obtaining a quench rate that avoid phase separation can be challenging [117]. Meanwhile, for gel systems where the interactions are mediated by the addition of non-adsorbing polymer, instantaneous quench is considered to be the route to gelation [180].

Therefore we used depletion mechanism, introduced in subsection 2.2.5, as the driving force to promote the assembly of colloidal particles into clusters. The advantages of using such systems are the interparticle attractive forces can be tuned and controlled unlike in molecular systems and that it is possible to study the structure of the suspension at the single-particle level, using optical or confocal microscopy. This has been previously discussed in Section 2.1.

Although the full understanding of gelation remains a challenge, in the case of the colloidal gels in this work, the dynamically arrested network passes through its energy landscape towards an equilibrium state of crystal-gas phase coexistence at a very slow rate [32, 184]. The gelation process begins with demixing of the particles into a (colloidal) "gas" and "liquid". Spinodal decomposition leads to a network of particles [22, 28, 173, 185, 186]. Here the "liquid" has a sufficiently high density ($\phi \gtrsim 0.58$) to exhibit slow dynamics [59, 117, 173]. The network can remain for years [187]. However, if the self-generated or gravitational stress is weaker than the yield stress [188], for monodispersed colloidal particles, crystallisation may eventually occur [32]. The resulting crystallisation from such /ARa dynamically arrested network has been seen in simulation [39, 180, 189] and experiment [181].

In our work, demixing is driven by effective attractions between the colloidal particles induced by the addition of non-absorbing polymer. In the case of short range attractions, the behaviour of the system is insensitive to the precise nature of the interaction [127] so the square-well model studied in simulation [39] can be taken as a reasonable model of the experimental colloid-polymer mixture. The simulation work reported in this chapter was carried out by Dr. Francesco Turci.

Previously, it has been shown that gels can self assemble to the ordered array characteristic of a crystal both in experiments [181] and simulations [180]. On the way to crystallisation, more subtle structural changes may also occur. Similar to vitrification[190], gelation is accompanied by changes in local structure. The local structural changes are not clearly shown in pair correlation function $g(r)$

[117, 191, 192]. Therefore, a higher-order correlation is needed in detecting the changes in the local structures. This chapter focuses on the structural analysis of the process by which a gel transforms from its initial state of locally rigid amorphous structure [117] to being locally crystalline. On the following sections the sample preparation and techniques used to analyse the system will be detailed.

4.1 Methods

4.1.1 Model and interaction potential

For this work, the colloid polymer system is taken to follow the Asakura-Oosawa (AO) model [15–17, 193], where colloids are treated as hard-spheres and polymers are assumed to be interpenetrating spheres with a hard interaction with the colloids. The details of this model is given in Chapter 2 subsection 2.2.5. The effective pair potential between the colloidal particles in the AO model shown in the above mentioned subsection in Fig. 2.3 [17, 112, 113], which is rather accurate for our parameters [12, 94].

The details of mapping the AO and Morse potentials are discussed in Chapter 3 Section 3.6.1 based on the second virial coefficients B_2^* values. In the following sections, simulation results are labeled by these effective AO well-depths, which are indicated by $u_{\mathrm{AO}}^{\mathrm{min}}$.

4.1.2 Experimental setup

For this work, sterically stabilised polymethyl methacrylate (PMMA) particles labelled with rhodamine as the fluorescent dye are mixed with non-adsorbing polystyrene (PS) polymer. The diameter and the polydispersity of the PMMA is σ=1.4μm and 4%, respectively, determined using scanning electron microscopy. Fig. 4.1 shows the image obtained from scanning electron microscopy. The polymer molecular weight is $M_w = 30 \times 10^6$ g/mol, leading to a polymer-colloid size ratio of q =$2R_{\mathrm{g}}/\sigma$=0.3, where R_{g} is the polymer radius. We estimated the polymer radius of gyration as R_{g}=203 nm in ideal solvent based on method previously detailed in Chapter 3 subsection 3.1.2. The overlap concentration is c_p = 2.49g/L.

Our colloid-polymer system is suspended in a mixture of cis-decalin and cyclohexane bromide (CHB) in order to obtain a density and refractive index matched suspension. Any residual electrostatic interactions were screened by adding 4 mM tetrabutylammonium bromide (TBAB) salt to the solvent mixture. Density matching between the particles and solvent mixtures is achieved by centrifuging the sample

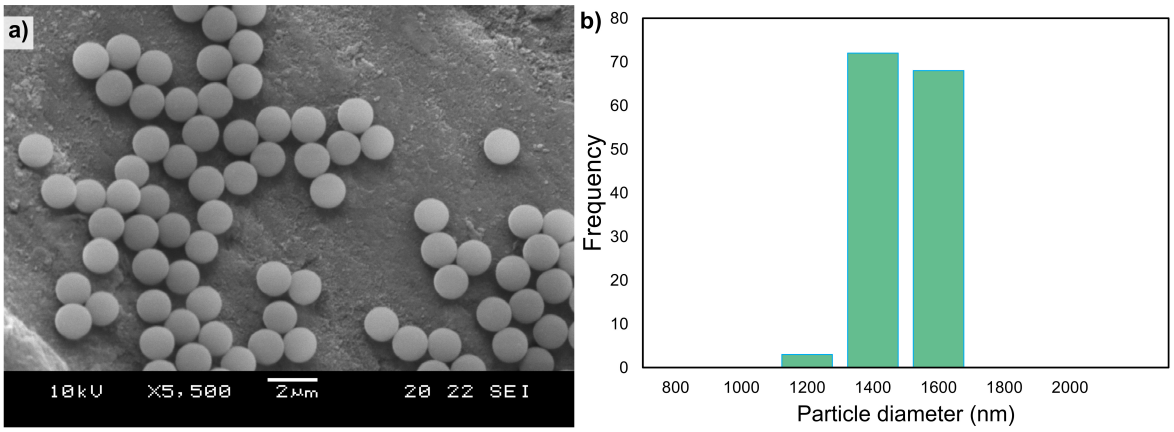

FIGURE 4.1. Figure is showing a) an image of PMMA used in this work taken using scanning electron microscope (SEM). The scale bars represent 2 μm and b) size distribution of the PMMA.

for 15 mins at 11 000 rpm. The interaction potential between the PMMA particles is controlled by the concentration of polymer added as described in section 4.1.1.

The sample is then transferred into custom made cells as described in Chapter 3 subsection 3.4.2. Once the sample is in the cell, the openings are sealed with epoxy resin. The height of the capillary is estimated to be between100-150μm. This determination was carried out by taking the z-stack images of the whole capillary using confocal microscopy (Leica SP8). The temporal changes of the colloidal gel were attained in cubic images of xyz volume of $48 \times 48 \times 48$ μm. The first image was taken after 10^3 τ_{B} sample added into the cell and further structural changes is observed up to 4 days. To delay the sedimentation in the z axis, the capillaries were kept so that the longest axis was in an upright position. Based from the images taken, the coordinates of the particles were obtained with a 3d particle tracking algorithm adapted from [194].

As our unit of time, we use the Brownian time which we define as the typical time for a free colloidal particle to diffuse a distance comparable with its radius:

$$\tau_B = \frac{\sigma^2}{24D} = 0.575\mathrm{s}, \tag{4.1}$$

where

$$D = \frac{k_{\mathrm{B}}T}{3\pi\eta\sigma} \tag{4.2}$$

is the Stokes-Einstein diffusion constant, in which η is the solvent viscosity.

4.1.3 Simulation

The experimental polydispersity was mimicked by using several particles of different sizes. A total of $N = 10000$ particles in a cubic simulation box of size $L \times L \times L$ with $L = 29.2\bar{\sigma}$, where $\bar{\sigma}$ is the average sigma of the particles (setting the units). We use a mixture of 7 components approximating a polydispersity of 4% with a Gaussian probability distribution of mean $\bar{\sigma}$ and standard deviation $\Delta = 0.04\bar{\sigma}$. The particles have $\sigma_i = 0.88, 0.92, 0.96, 1.0, 1.04, 1.08$ and 1.12. The volume fraction is ϕ 0.2 (matching the range of volume fractions used in experiment). All particles have the same mass of m. The Morse potential, as given in Eq. 4.3 was used to substitute the AO potential between the colloids in the simulation. In Chapter 3 we presented the details of the Morse potential and previous work which shown this potential accurately replicate the behaviour of the AO system [12].

$$u_{\text{mor}}(r) = \varepsilon_{\text{mor}} \mathrm{e}^{-2\rho_0(r-\sigma_{ij})} - 2\mathrm{e}^{-\rho_0(r-\sigma_{ij})} \tag{4.3}$$

where ε_{mor} is the potential well-depth, ρ_0 is the attraction range and σ_{ij} is the minimum of the interaction between particles of i and j species. Following previous study, ρ_0 is taken as $\rho_0 = 25.0/\bar{\sigma}$ [12].

The motion of particles in the solvent is described using Langevin (or Brownian) dynamics using LAMMPS package[164] as given in Chapter 3 Section 3.6. The system started at random configuration corresponding to a liquid at high temperature then quenched to final interaction potential of u_{AO}^{min}=4 k_BT and 5 k_BT.

4.1.4 Structural analysis

As was previously discussed in the introduction of this chapter, subtle changes in local structure due to gelation are not clearly shown in structural analysis using pair correlation function $g(r)$, we therefore probe the local structure in our gels with two methods. First, we consider the 2-point correlation function $g(r)$. By comparison, we expect [117, 190], that higher-order methods may yield more insight into the local structure. For this purpose we use the topological cluster classification (TCC) [10]. The TCC identifies regions of the system whose bond network is topologically equivalent to isolated clusters which minimise the energy of the Morse potential. For the parameters we consider here, the Morse interaction is a very accurate representation of a colloid polymer system [12].

More specifically, the Morse clusters identified correspond to a relatively short range, with range parameter $\rho_0 = 25.0$ (in the notation of Doye and Wales [169]). Due to the large number of structures identified by the TCC we chose to narrow down our analysis to structures interacting via the range parameter mentioned above

and represent the minimum energy structure for an isolated group of n particles where $5 \leqslant n \leqslant 13$. The 13 particle clusters which represent face centred cubic (FCC) and hexagonal close-packed (HCP) are also identified. Figure 4.2 illustrates several of the clusters we focused on this work.

4.2 Results and discussion

We present our results by first discussing the phase behaviour of the experimental system. Then, discussion of the analysis begins by considering the snapshots of the raw image data. Next, the widely used pair correlation function $g(r)$ as descriptor of local structures for gels at different times is discussed. It has been reported that significant structural changes accompany the gelation process, moreover, to ageing colloidal gels [117]. Therefore, the changes to the local structure of our colloidal gels as time progresses were analysed using the Topological Cluster Classification (TCC) [10]. The pair correlation functions and cluster identification were performed by employing the 3d coordinates from particle tracking.

4.2.1 Phase behaviour

Summary of the states observed in the experimental colloid polymer mixture is shown in Fig. 4.3. The axes of the phase diagram give the colloid volume fraction ϕ

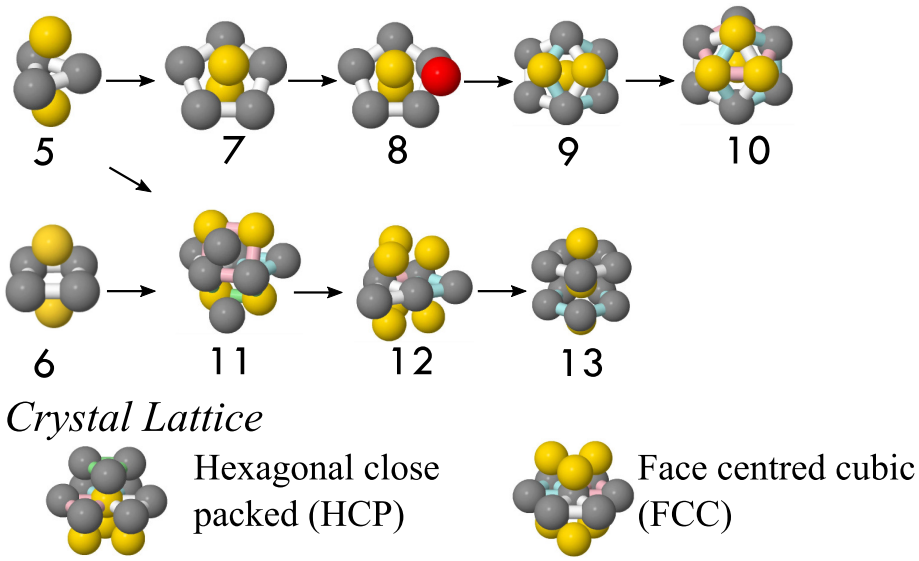

FIGURE 4.2. The chosen clusters identified by Topological Cluster Classification (TCC). The arrows are relating the substructures to superstructures. [10].

and interaction strength $u(\sigma)$ of the colloid polymer system. The critical point of a system was estimated based on the extended law of corresponding states [123] at $B_2^* = -1.5$, as was discussed previously in Chapter 2. In the experiments, the critical point is ϕ_c=0.31 with interaction strength $u(r) = 2.64\ k_BT$ estimated from [95, 195, 196]. The spinodal line is represented by the dashed line and its flat shape is typical for colloid-polymer mixture with $q \approx 0.3$ interaction range as our system.

The physical attributes of the phases are also shown in Fig. 4.3. Minimal addition of polymer resulted in weak attraction and the colloidal particles are still diffusing freely in the fluid phase. However, increasing the addition of the polymer, elevated the interaction strength leading to particle aggregation and the eventual arrested phase. Due to the high monodispersity of the particles, emergence of crystalline structures were visible almost instantly, when the interaction potential of the system is close to the spinodal line.

4.2.2 Time evolution

We begin the analysis by considering the raw image data as shown in Fig. 4.4. Here we see the increasing crystallinity of colloidal gel of 3 k_BT with time. Due to the high monodispersity of the particle, crystallisation can be observed almost

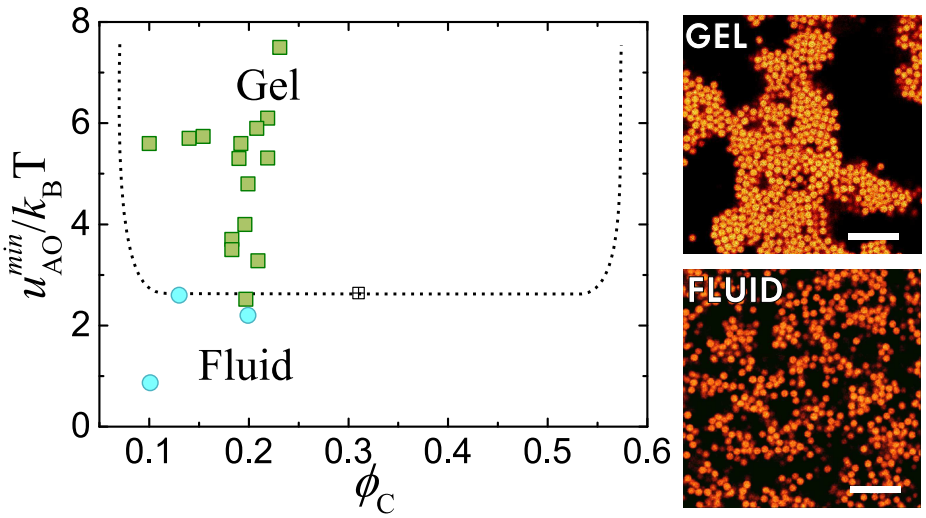

FIGURE 4.3. Phase diagram of the experimental colloid-polymer mixture with $q = 0.3$, as a function of colloid volume fraction ϕ_c and attractive interaction strength u_{AO}^{min}. Green squares indicate gels while the blue circles indicate homogeneous fluids. The ⊠ is the critical point determined based on the reduced second virial coefficient B_2^* and critical isochore estimated from the literature [95, 195, 196]. The scale bars represent 10 μm.

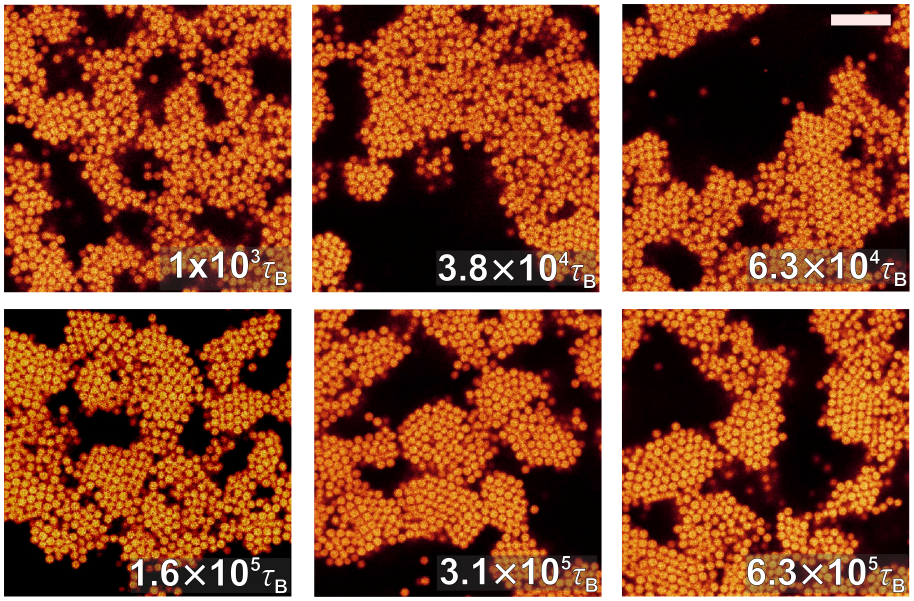

FIGURE 4.4. The formation of crystalline clusters with time for 3 k_BT colloidal gel. The scale bars represent 10μm.

instantaneously for 3 k_BT gels. Starting from a typical coarse gel branch network, some ordering in the network is evident starting from $\tau_B \sim 3.8 \times 10^4$. Then, breakage of the network “arm" leads to the formation of crystalline clusters as the time progresses.

4.2.3 Two-point structural analysis

The pair correlation function $g(r)$ results of the experimental system are shown in Fig. 4.5. All of the graphs displayed a common feature for quenched systems with arrested phase, the presence of a split second peak in each colloidal gel. The overall shape of the pair correlation is unaffected with the increasing interparticle attractions. Additionally, the 3 colloidal gels demonstrated long-range density fluctuations based on the longer oscillation decay to unity [197].

For a colloidal gel with interaction strength of 3 k_BT, the two-point structural analysis changes rather little as a function of time, although there is some further enhancement of the second peak. In Fig. 4.5 (a), a subtle second peak appeared with the progress with time. The emergence of a short-range order of sixfold symmetry in a crystalline structure can be its contributing factor. The changes in the second peak is often associated with the liquid approaching crystallisation[198]. Meanwhile, the $g(r)$ of 4 k_BT and 5 k_BT colloidal gels also show very little changes with time. Although there is a slight decrease in separations, colloidal gels between 4 k_BT and 5 k_BT reflecting the increasing interaction strength. The emergence of additional

peaks are expected in two-point structural correlations upon full crystallisation, as was observed in 3 k_BT colloidal gel. However, changes in amorphous structure and partial crystallisation can be harder to detect [117, 190]. Based on the figure, the two-point analysis definitely displayed some structural changes both with time and increasing interaction strengths but it does not offer any information on the local structures at particle level. For this we used topological cluster classification for higher-order structural analysis.

4.2.4 Higher-order structural analysis

The structure of the gel network is formed of connected clusters of minimum energy ($m < 14$) [117, 180] which are illustrated in Fig. 4.2. These are identified using the topological cluster classification (TCC) along with the face centred cubic (FCC) and hexagonal close-packed (HCP). In all the graphs, N_C is the number of particles in a particular cluster and N is total number of particles detected.

Figure 4.6 shows experimental results of the changes in local structure during the crystallisation process for gels with $u(\sigma) = 3\,k_BT$, $4\,k_BT$ and $5\,k_BT$. In the experiment, the first image was captured around $10^3\ \tau_B$ after the sample was prepared.

As it is presented in Fig. 4.6, initially all of the dynamically arrested networks are dominated with 8, 9 and 10 particle clusters. These clusters are made of single, double and triple five-membered rings respectively, and are not compatible with the crystalline phase. It has been shown in simulation five-fold symmetrical clusters suppress crystallisation [75, 199–201] and the same clusters are common in dense fluids [11]. The five-fold symmetrical clusters are frequently found in colloidal gels like the systems reported here [180, 202] and in molecular gels [203]. However, as time progressed a significant decrease of the five-fold symmetrical clusters are clearly visible in 3 k_BT gel, demonstrated in Fig. 4.6 (a). For example, clusters with 10 particles showed a 10-fold decrease by the end of experiment. In contrast, the population of crystalline clusters; face-centred cubic (FCC) and hexagonal close packed (HCP) increased 10-fold at $4 \times 10^4 \tau_B$; about at the same time when the five-membered rings showed a decrease. This suggests that in the $u(\sigma) = 3\ k_BT$ gel, structural rearrangement occurs in the crystalline frustrating five-fold clusters where the particles detached and formed favourable crystal forming clusters. The rapid formation of crystalline structures is in the expense of five-fold symmetrical clusters reached a plateau once the bulk of the system has crystallised.

On the other hand, in Fig. 4.6 (b) the numbers of FCC and HCP remained somewhat constant with some fluctuation throughout the experiment. Meanwhile the five-membered ring clusters showed a gradual increase as time progress. The fluctuation of the crystalline structure numbers suggests that the creation and melting

of local ordered organisation in the network. Overall, all of the clusters in 4 k_BT gel maintained a constant fraction number the entire experiment.

For a gel with $u(\sigma)$ = 5 k_BT shown in in Fig. 4.6 (c) the population of clusters with 8, 9 and 10 particles displayed a steady increase until the end of observation. Interestingly, the number of FCC and HCP clusters also showed a slight increase with some fluctuations by the end of observation but these numbers are significantly less compared to the number of five-membered ring clusters present. Both in (a) 3 and (c) 5 k_BT the growth of higher numbered clusters are accompanied with the decrease number of smaller clusters, for example five particle clusters. This is due to the smaller structures are incorporated into the larger clusters creating compound clusters.

Figure 4.7 shows the local structural changes for gels with $u_{\mathrm{AO}}^{\mathrm{min}}$ = 4 k_BT and 5 k_BT interaction strengths from simulations. The number of clusters detected are clearly more than that of in experiments based on the higher fraction number in Fig. 4.7 (a) and (b). At certain times some clusters were detected as zero by the TCC resulting to the absent points in the logarithmic y-axis graphs on the left panel.

For $u_{\mathrm{AO}}^{\mathrm{min}}$ = 4 k_BT gel shown in Fig. 4.7 (a), clusters with 10 particles decrease significantly with time while drastic growth of FCC and HCP clusters is apparent. The trend that is observed in $u_{\mathrm{AO}}^{\mathrm{min}}$ = 4 k_BT simulation result is comparable with $u(\sigma)$ =3 k_BT gel from experiment whereby both systems are considered as shallow quenched systems. That is to say, the number of crystalline clusters increased at the expense of depleting five-membered ring clusters indicating the same structural rearrangement of the five-membered ring clusters to form a network of ordered clusters. However, there is a slight difference in the type of six-fold symmetrical clusters significantly formed in each system. The highest number of six-fold symmetrical clusters formed in the experimental system is the HCP while it is the FCC in the simulation system. In the shallow quenched systems, reversibility is possible for the clusters to correct its bonding to promote stable crystalline ordering.

For $u_{\mathrm{AO}}^{\mathrm{min}}$ = 5 k_BT gel, the initially decreasing population of clusters with 8 and 9 particles showed an increase by the end of the simulation. Meanwhile, a drastic decrease is observed for clusters with 10 particles but this decrease was not accompanied by an increase of crystalline clusters like FCC and HCP. Looking at $u(\sigma)$ =4 and 5 k_BT gels from experiment, and $u_{\mathrm{AO}}^{\mathrm{min}}$ = 5 k_BT gel from simulations, for a deeply quenched system, the initial five-fold symmetrical clusters only increase with time. Particularly, larger five-fold symmetrical clusters such as the 8, 9 and 10 particles clusters. The colloidal particles in these deeply quenched systems, are irreversibly bonded, corrections are not possible. Furthermore, both in the experiments and simulations, the fraction of 8 membered clusters shows an increase. This is an

indication that, deep quenched systems are kinetically trapped in the local minima and if there are any rearrangement occurring within the systems, it is not accessible within the experiment duration. In both $u_{\mathrm{AO}}^{\mathrm{min}} = 4\ k_BT$ and $5\ k_BT$ gels, cluster with 12 particles show a significant presence unlike the results from experiments. The absence of hydrodynamic interaction in the simulations are the main contributing factor in promoting the growth of larger clusters in the simulated gels. This could also be attributed to the higher number of FCC crystalline clusters in the $u_{\mathrm{AO}}^{\mathrm{min}} = 4\ k_BT$ gel than in the $3\ k_BT$ experimental gel.

In both experiment and simulation, systems with weak interaction strength or less quenching shows a higher degree of crystallisation as time progress. This is in agreemen with previous report [1]. Nevertheless, the lack of crystallisation in deeper quenched systems is emblematic to kinetically trapped systems [1, 117, 180].

4.3 Summary

Here, temporal studies of crystallisation in dynamically arrested networks have been carried out in experiments and simulation. The interaction strengths of the simulations are mapped to that of experimental systems using Morse potentials. This potential has been shown to accurately replicate the behaviour of the AO including its higher-order local structures [12]. Comparisons of cluster populations reveal strong structural similarity between experiment and fitted simulation. These are taken as indicators that the state points of the systems are rather similar.

Measuring the development of the six-fold clusters, HCP and FCC, allows comparison of crystallisation kinetics between experiment and simulation. Both are seen to have drastic crystallisation growth in the shallow quenched systems. While there is a discrepancy in the types of six-fold symmetrical clusters observed in each system, the overall trend of depleting numbers of five-fold symmetrical clusters in both shallow quenched systems are evident. The higher number of HCP in the experimental system is due to its larger system size as compared to that of the simulations. The experimental system is four orders of magnitude larger than the simulations. The finite system size in the simulations, might restricts crystallisation in the percolating network to the ground structure of crystals that is the FCC.

Using the topological cluster classification, the effective self-assembly is analysed in terms of the local structures evolved. In parallel to a number of studies on similar colloid-polymer system, crystallisation is observed in shallow quenched systems [1, 39, 183]. The reversibility of the system enables the clusters to correct any ineffective aggregation. On the other hand, in the deeply quenched system the

significant number of five-fold symmetrical clusters is in agreement with a number of studies [86, 201]. These clusters are important motif in the kinetically trapped systems and are reported to suppress crystallisation [75, 199–201].

Examining the local structures temporal evolution in the colloid polymer system using two-point structural analysis; the pair correlation function, gives very little detail when compared to the topological cluster classification method. Here, we have shown that to capture the structural evolution of an ageing colloid polymer systems, a higher-order structural analysis method are required.

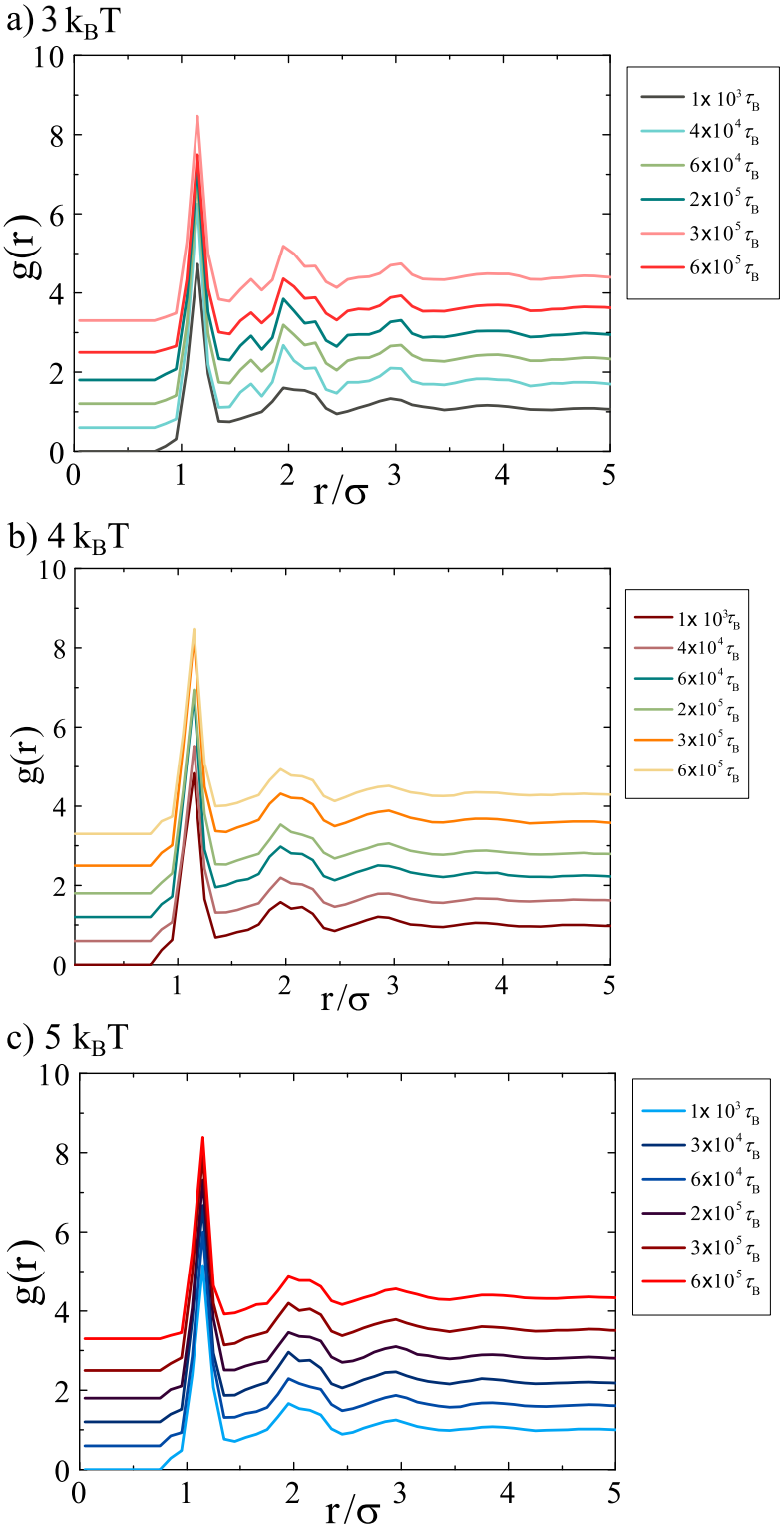

FIGURE 4.5. The temporal progress of pair correlation functions of (a) 3, (b) 4 and (c) 5 k_BT experimental systems. The changes in time are off-set in the y-axis for clarity.

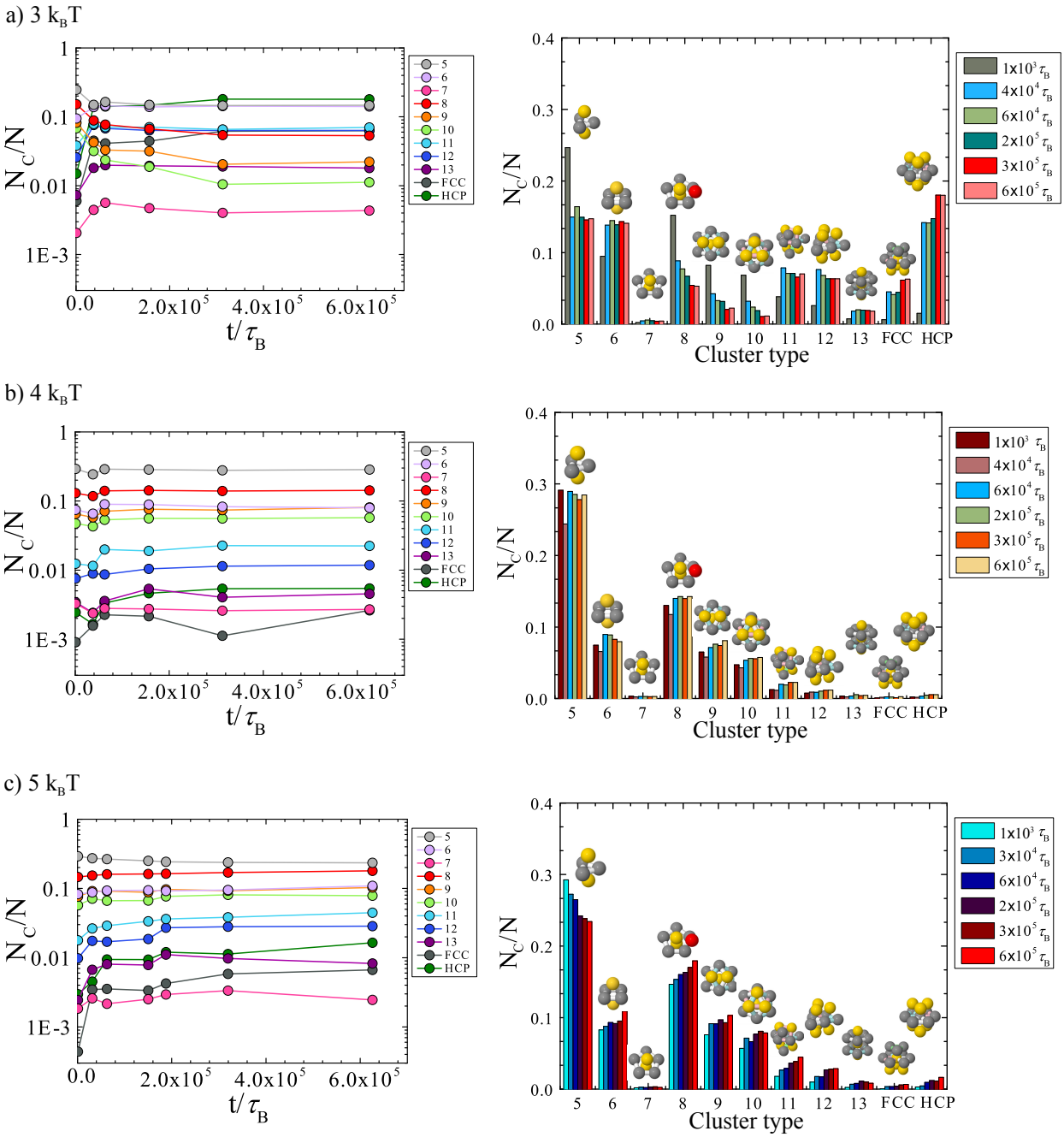

FIGURE 4.6. Results from experiments showing the particles population with time evolution for $u(\sigma)$ (a) 3 k_BT, (b) 4 k_BT and (c) 5 k_BT colloidal gels. Logarithmic ordinate has been used in left panel to better show the cluster populations changes. The temporal population of corresponding $u(\sigma)$ is shown on the right panel in bar-graph representations. N_c is the number of particles in a particular cluster, N total number of particles.

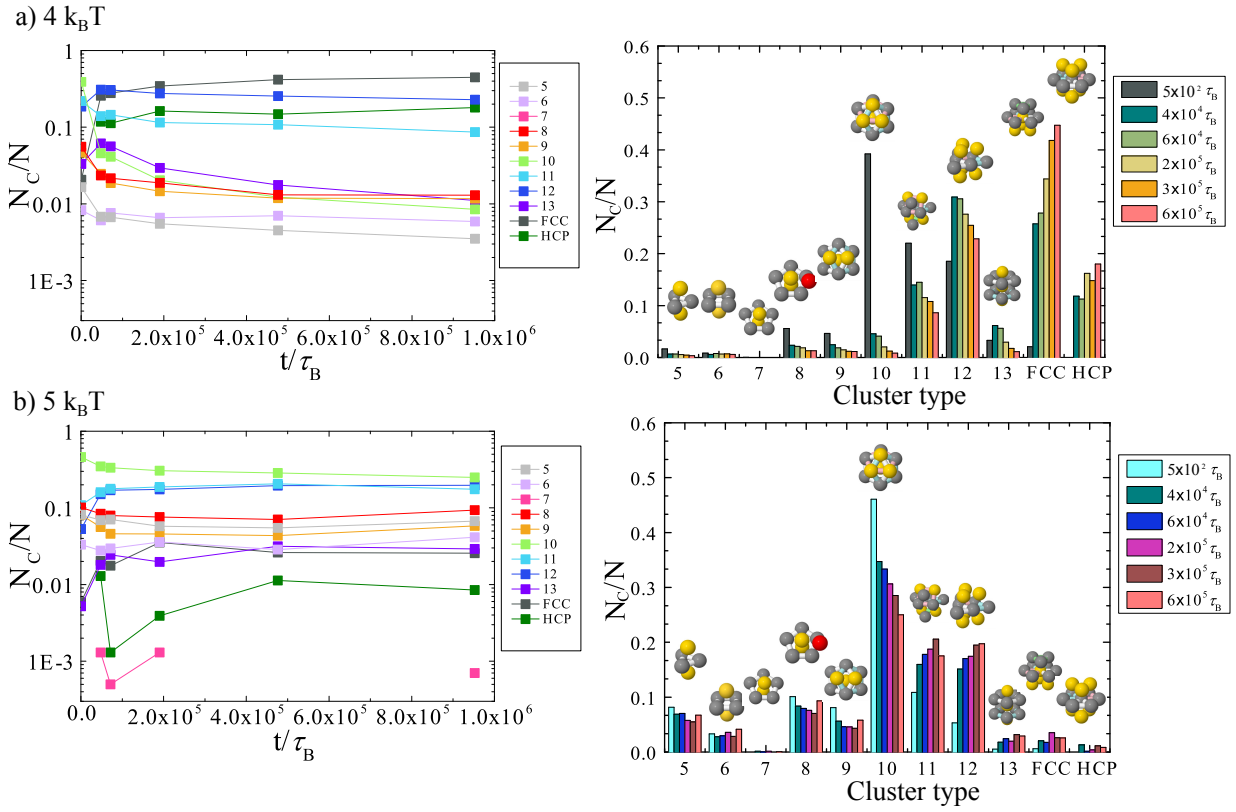

FIGURE 4.7. Results from simulation showing the particles population with time evolution for $u_{\mathrm{AO}}^{\mathrm{min}}$ (a) 4 k_BT and (b) 5 k_BT colloidal gels. Logarithmic ordinate has been used in left panel for clarity. Disjointed temporal progress to some clusters indicates zero number of clusters were detected as is evident in the right panel bar-graph representations. N_c is the number of particles in a particular cluster, N total number of particles.

CHAPTER 5

Effects of vertical confinement on gelation and sedimentation of colloids

This chapter has been published as: A. Razali, C. J. Fullerton, F. Turci, J. Hallet, R. L. Jack, and C. P. Royall, "Effects of vertical confinement on gelation and sedimentation of colloids," *Soft Matter*, vol. 13, pp. 3230–3239, 2017

A rich behaviour is displayed in non-equilibrium colloidal systems due to gravity [204]. This is contributed to the coupling between gravity, chemical potential [71, 139, 205, 206] and hydrodynamic interactions between particles [141, 207–211]. In addition, the addition of attractive interactions between the colloidal particles results to rich behaviour in stable systems without a gravitational field [32, 204]. Specifically, a network of particles induced by spinodal decomposition [22, 173, 186, 212, 213] can proceed to undergo dynamical arrest and network: form a gel [214, 215]. The addition of non-absorbing polymer induces effective attractions in these colloidal systems where the equilibrium properties can be derived from an effective one-component system of colloids. The interaction strength is determined by the polymer concentration [113, 216].

It was previously discussed that novel structure-dynamical correlations can occur from phase separation and sedimentation [32, 204–206, 217]. In the bulk colloidal systems, sedimentation is usually prevented by gelation due the presence of a finite yield stress in the network of arrested colloidal particles in gels [32, 59, 184, 218]. The arrested network is able to support its own weight while preventing sedimentation. Therefore, gels are often used to stabilise various commercial products by overcoming sedimentation [28, 29]. If the innate or gravita-

tional stress is weaker than the yield stress gels can remain for a long time [219]; up to years [187]. However, sedimentation often occurs in gels [119, 140, 220]. The onset of gel collapse can be sudden [24] and as was previously discussed in Chapter 2 section 2.6.3 this phenomenon remains poorly understood. In this delayed collapse, very small changes in the macroscopic properties are observed in the same timescales considered in this work. However, the system begins to sediment initiated by a change on a timescale of 10^5 particle diffusion times or more [24].

Previously, in large experimental systems where the particles are at least 10^5 times smaller than any linear dimension of the system, there may be at least 10^{15} particles in the system [24, 32]. Plus, the associated experimental timescales for sedimentation are at least of the order of 10^5 diffusion times. At present, in order to theoretically consider such large systems, only approximate approaches such as imposing one-dimensional solution to the height profile such as "batch settling" [31] and dynamic density functional theory [94, 221] has been performed. To the best of our knowledge such theoretical approaches have not been extended to consider systems which undergo gelation. This leaves computer simulation as a means to treat the problem of sedimenting gels, but the timescales (up to years) and the macroscopic system sizes are not accessible to direct simulation.

In this chapter we show that it is possible to conduct experiments in much smaller systems by using glass capillaries. Figure 5.1 shows the difference between bulk systems (as reported previously [24, 32]) and the system size used in this work. Here the relevant linear dimension (the height) is of order 100 particle diameters which is manageable in computer simulation. Therefore, such small systems offer a way where the simulation can be compared with experiment. Brownian dynamics simulations were employed by Dr. Christopher Fullerton where solvent-mediated hydrodynamic effects are included only at the one-body level (that is Stokes drag), and hydrodynamic interactions between the particles are neglected. Such interactions can have significant effects in sedimentation [31, 141, 210, 211, 222] and in gelation [223, 224]. However, in order to consider these interactions in simulations would limit the accessible time scales and system sizes. Furthermore it can be expected that the effects of hydrodynamic interactions are reduced due to the small Peclet numbers in these experiments.

The sedimentation behaviour of bulk gels has been previously extensively studied [24, 225] and it is known to be characterised by an initial delayed collapse followed by a slow settling that can take 60 hours [24]. It has also been widely accepted that thermal ageing contributes to the fragility of gel, until it reached a critical time when gel cannot support its own weight and collapse. Large-scale fractures and heterogeneities in the form of 'volcanoes' and solvent channels have

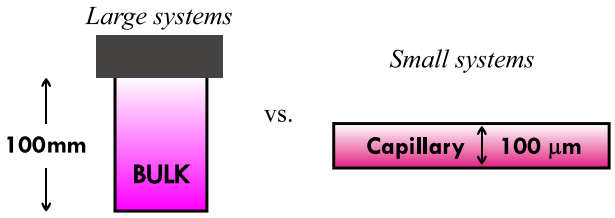

FIGURE 5.1. A sketch showing the size difference between experimental systems in previous work [24, 32], and the system described in this work.

been observed before collapse in experiments of the bulk systems [119, 143]. In this chapter, we focus on the observation of sedimentation in vertically confined gels and measure the effects of interaction strength to the time evolution in experiments. The effects to the time evolution is reproduced in simulations. Local structural information was also obtained from the simulations, which helps to explain the different sedimentation behaviour for different interaction strengths.

5.1 Methods

5.1.1 Model and interaction potential

As was previously elucidated in Chapter 2 subsection 2.2.5, the colloid-polymer mixtures used throughout this work can be described based on Asakura-Oosawa (AO) model. Details of the interaction potential can be referred in the above mentioned subsection. We also employ the same effective interaction by the well-depth as previous chapter:

$$u_{\mathrm{AO}}(\sigma) = u_{AO}^{min} = q^2 k_{\mathrm{B}} T \rho_{\mathrm{p}} \sigma^3 \frac{\pi(3+2q)}{12} \tag{5.1}$$

where the fugacity z_{p} is equal to the number density ρ_p of ideal polymers in a reservoir at the same chemical potential as the colloid-polymer mixture.

5.1.2 Experiment

In the experimental setup, sterically stabilised polymethylmethacrylate (PMMA) with a diameter $\sigma = 460$ nm is suspended in cis-decalin. The colloidal polydispersity is approximately 4% as determined with static light scattering. In spite of the fact that crystallisation occurs in hard spheres with a polydispersity of 4%, in attractive systems crystals are formed at higher volume fraction as reported in [33]. This demonstrates that there is more sensitivity to polydispersity. Therefore, 4% can be

sufficient to reduce crystallisation [180]. A colloidal gel was obtained by adding nonadsorbing polystyrene polymer with molecular weight $M_w = 3.46 \times 10^6$, resulting in a polymer-colloid size ratio of $q = 2R_g/\sigma = 0.3$. The polymer radius of gyration $R_g = 67$ nm is from estimation that is previously discussed in Chapter 3 subsection 3.1.2. This corresponds to a polymer overlap concentration of $4.56\,\mathrm{gL}^{-1}$.

The gravitational length λ_g is determined to be $\lambda_g = 6k_BT/(g\delta\rho\sigma^3) = 27.1\mu$m where $\delta\rho$ is the density difference between the PMMA and the solvent. Hence, λ_g is the height associated with a change of k_BT in gravitational potential energy of a colloidal particle. The Péclet number for sedimentation is then $Pe = \sigma/(2\lambda_g) = 8.51 \times 10^{-3}$.

As for the unit of time, the Brownian time τ_B is employed which was defined previously as the time scale for a particle to diffuse its own diameter. For the parameters in this work the Brownian time is $\tau_B = \sigma^2/24D = 0.0317$s, where $D = k_BT/(3\pi\eta\sigma)$ is the Stokes-Einsten diffusion constant where η is the solvent viscosity.

Each sample was transferred into a 100 μm capillary and sealed with epoxy resin. The manufacturing tolerance of these capillaries is around 10%. The resin was allowed to set prior to imaging and data was taken after 5 minutes. The imaging of a z-stack of the entire capillary height was done using time-resolved confocal microscopy (Leica SP5). For each data set, the z-stack images were taken at intervals of approximately 8 minutes, for a duration of 20 hours. The height of the capillaries were determined from the sample images in xy and yz planes. The top of the capillary is determined from the particles visibly stuck to the glass capillary walls, which are evident in our work as shown in Fig.5.3a. Then, this observation is continued in z-axis before the appearance of complete dark space to be the bottom of the capillary. When reporting experimental data, we use the polymer reservoir representation where the polymer concentration in the reservoir is related to that in the experiment by Widom particle insertion [33], previously discussed in Chapter 2. The colloid volume fraction for each sample is extracted from the intensity measurements of the images obtained using the confocal microscope following [206]. These measurements were calibrated against homogeneous samples of known volume fraction, where there is a linear dependence of the measured intensity against colloid volume fraction.

In order to determine the phase diagram of the model, data is collected in the range of 0.1-0.35 colloid volume fractions ϕ_c. In describing the sedimentation behaviour of the system as a function of the different interaction strengths induced by the different polymer concentrations, volume fraction $\phi_c = 0.2$ is used throughout the work described in this chapter.

5.1.3 Simulation

Details of the Morse potential used in all simulation carried out for this work has been described in Chapter 3 subsection 3.6. The potential is used to simulate the AO potential between colloids which has been shown to accurately reproduces the behaviour of the AO system [12]. The simulation work reported in this chapter was done by Dr. Christopher Fullerton. Similar to previous chapters, the Morse potential is given as:

$$u_{\mathrm{mor}}(r) = \varepsilon_{\mathrm{mor}} \mathrm{e}^{-2\rho_0(r-\sigma_{ij})} - 2\mathrm{e}^{-\rho_0(r-\sigma_{ij})} \tag{5.2}$$

where $\varepsilon_{\mathrm{mor}}$ is the potential well-depth, ρ_0 is the attraction range and σ_{ij} is the minimum of the interaction between particles of i and j species. The attraction range is taken as $\rho_0 = 25.0\sigma^{-1}$ following [12]. Also, an additive mixing rule $\sigma_{\mathrm{AB}} = (\sigma_{\mathrm{AA}} + \sigma_{\mathrm{BB}})/2 = \sigma$ was used. The reduced well-depth ε_{mor}/k_BT is varied between 1.0 and 30.0.

In order to easily mimic the experimental polydispersity, a binary mixture of particles was used in the simulation, with equal numbers of each species. The diameters of the two species are $\sigma_{AA} = 1.04\sigma$ and $\sigma_{BB} = 0.96\sigma$. A total of $N = 60{,}000$ particles in a simulation box of size $L \times L \times L_z$ with $L = 28.025\sigma$ and $L_z = 200\sigma$ was considered. Thus, the resulting volume fraction is $\phi_{\mathrm{c}} = 0.2$, the same as in the experiment. All particles have the mass of m. The boundary conditions are periodic in the x and y directions while there are walls at $z = 0$ and $z = L_z$ that are described in detail below. The sample height L_z and lateral dimension L are analogous with the dimension of the capillary used in the experiment and the range over which experimental data was taken, respectively.

Here, the dynamics of the particles includes the gravitational field effects together with the confinement effects of the capillary. The gravitational potential energy of a particle at height z is $E_{\mathrm{g}}(z) = zk_{\mathrm{B}}T/\lambda_{\mathrm{g}}$ with $\lambda_{\mathrm{g}} = 60\sigma$, which is the same as the experiment. For simplicity, truncated and shifted Lennard-Jones potentials were used to simulate the walls creating vertical confinement. This is represented as $u_{\mathrm{wp}}(\Delta z) = 4\epsilon_{\mathrm{wp}}[(\sigma_{\mathrm{wp}}/\Delta z)^{12} - (\sigma_{\mathrm{wp}}/\Delta z)^6]$ where Δz is the distance of the particle from the wall. The range of the potential is $\sigma_{\mathrm{wp}} = 0.125\sigma$, comparable with the range of the Morse potential and the well-depth is $\varepsilon_{\mathrm{wp}} = 2\varepsilon_{mor}$. Since the potential is truncated and shifted at its minimum, the top wall (at $z = L_z$) is purely repulsive. The bottom wall (at $z = 0$) accounts for depletion interactions between colloids and the wall, and is truncated and shifted at $r = 2.4\sigma_{\mathrm{w}p}$.

Preparation of initial conditions. — To copy the experimental conditions as far as possible, the system is set to be in a well-mixed state at the start of simulation. For

this, both the interparticle interactions and the interactions with the wall are fixed to be purely repulsive. In the beginning, the particles are in random positions while overlapping particles are removed using a conjugate gradient minimisation. Then, the system is evolved for $50\tau_0$ to reach equilibrium resulting to a homogeneous fluid configuration. Then, for the main simulations these configurations are used as initial conditions by including gravity and attractive interactions. The simulation results shown here are the average of 3 independent trajectories. The fluctuations between trajectories are small due to the fairly large systems.

Mapping between experiment and simulation.— Details of mapping the AO and Morse potentials are discussed in Chapter 3 section 3.6.1 based on the second virial coefficients B_2^* values. Similar to Chapter 4, in the following sections, simulation results are labeled by these effective AO well-depths, which are indicated by u_{AO}^{min}.

5.2 Results

5.2.1 Phase behaviour of experimental system

The phase diagram of the experimental system, as a function of well depth and polymer concentration c_p and colloid volume fraction, ϕ_c is summarised in Figure 5.2. This diagram is representative of colloid-polymer mixtures with size ratio $q = 0.3$. A liquid-vapor critical point in this system can be estimated from the extended law of corresponding states [123], shown here at $B_2^* = -1.5$ as presented before in Chapter 2. In the experiments, the criticality was observed to occur at polymer volume fraction (in the so-called experimental representation) 0.56 gL^{-1}.

The critical point is estimated from the literature [95, 195, 196]. The dashed line is an indicative spinodal line. As illustrated in the snapshots in Fig. 5.2 the system explores cluster phases (point **b**) or gel phases (points **a**,**c**,**d**) of different nature depending on the concentration of polymers and the colloid volume fraction: thin networks at low ϕ_c (**a**) or close to the spinodal (**d**); much coarser networks at high ϕ_c and high polymer concentration (**c**).

In the experimental samples, we see dynamically arrested gels for polymer concentrations higher than that is required for criticality. There is no sign of colloidal liquid-gas phase separation (either stable or metastable). This might due to the short range of the interaction results in dynamical arrest before phase separation can be completed. Crystallisation of the system is avoided on these time scales due to the polydispersity [226].

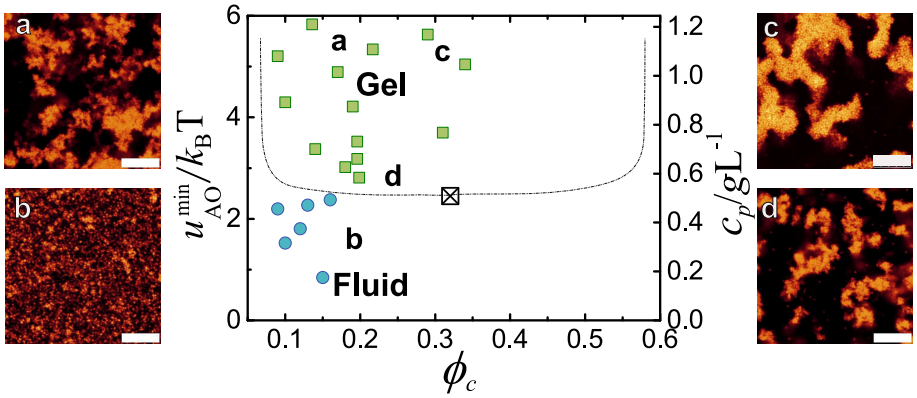

FIGURE 5.2. Summary of the states observed in the experimental colloid-polymer mixture with $q = 0.3$, where the ordinates are the functions of colloid volume fraction ϕ_c and attractive interaction strength u_{AO}^{min}, and polymer concentration. The green squares indicate gels and blue circles indicate homogeneous fluids. The ⊠ is the critical point determined based on the reduced second virial coefficient B_2^* and critical isochore estimated from the literature [95, 195, 196]. The approximate position of the spinodal is indicated by the dashed line. The images show the phase behaviour observed at different points in the phase diagram: (a) low density gel at low ϕ_c and high polymer density; (b) low polymer concentration leading to a non-percolating cluster phase; (c) high ϕ_c and polymer concentration resulting in a coarse gel network; (d) phase coexistence between fluid and gel close to the spinodal line. Scale bars represent 10 μm.

5.2.2 Global sedimentation dynamics

In order to analyse the time-evolution of the colloid-polymer mixture, we first consider the sedimentation of the system as a whole for both simulation and experiment (see Fig. 5.3). At early times, gelation was observed as the formation of a percolating network of particles. At later times, particles can detach from the arms of the gel and diffuse through the solvent or move along the "surface" region between the "arms" of the gel and the solvent [117, 150]. The restructuring of the gel network and eventual collapse is induced by this detachment effect [14, 24, 150, 220, 227]. Figure 5.3(a) shows a sequence of such confocal images as time progresses for a system with $u_{AO}^{min} = 7.0 k_B T$. From the confocal images, it is evident that the gel network is initially distributed throughout the whole capillary before falling under gravity at later times. The same qualitative behaviour is shown in the simulation data in Fig. 5.3(b).

The time evolution of the height of the collapsing gel was determined by plotting the local colloid volume fraction $\phi_c(z)$ as a function of height z, as shown in Fig.

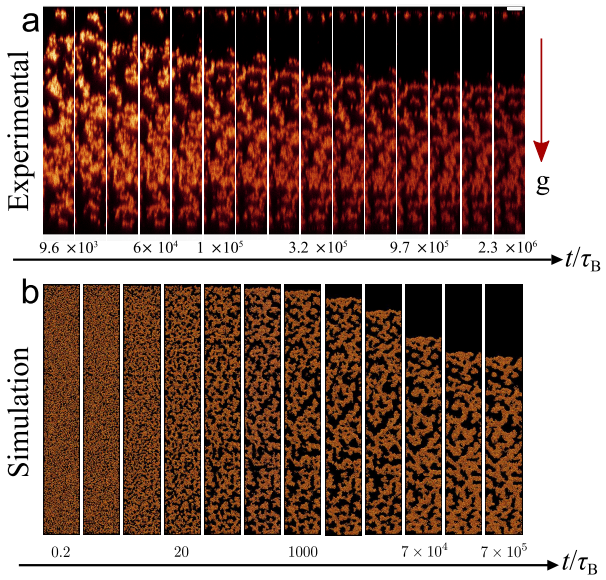

FIGURE 5.3. Time-sequence of sedimenting gels captured from (a) experiment with $u_{\mathrm{AO}}^{\mathrm{min}} = 7.0 k_B T$ and (b) simulation corresponding to $u_{\mathrm{AO}}^{\mathrm{min}} = 7.1\, k_B T$. The scale bar in (a) corresponds to 7.5 μm. The snapshots of the experimental and simulation systems show regions of comparable size (measured in units of the colloid particle diameter σ).

5.4. From the histogram, the gel-gas "interface" is obtained by fitting a hyperbolic tangent to $\phi_c(z)$, given as

$$\phi_c(z) = \phi_0 + \delta\phi \tanh\left(\frac{h-z}{\xi}\right). \tag{5.3}$$

Here ϕ_0 is the mean volume fraction in the regime we are fitting and $\delta\phi$ controls the change in volume fraction across the interface. The two fitting parameters are the height of the gel h and the interfacial width ξ. The fitting parameter h which is the height of the gel-vapour interface was normalised by the total height of the system, H, as the tolerance of the capillaries used in the experiments leads to small changes (less than 5% in the value of H) and given in as plot in Fig. 5.5.

In the case where the system does not form a gel because there are no attractive interactions, sedimentation is negligible for our parameters, as shown in Fig. 5.6. Batch sedimentation [31] of hard spheres for the same capillary height and a Péclet number $Pe = 0.01$ (similar to our experimental system) was considered in order to reach this result. There is little or no significant sedimentation in a colloidal system without any polymer shown by the relatively small change in height. This was also verified using simulation when the attractions between particles of the system are too weak to observe gelation.

The time evolution of the interface height was fitted with an exponential decay, shown in Eq.5.4 in order to estimate a timescale for the sedimentation τ_{sed}.

$$h(t) = h_{t\to\infty} + h_{\text{drop}} e^{-t/\tau_{\text{sed}}} \tag{5.4}$$

where $h_{t\to\infty}$ is the interface height at long times and $h_{\text{drop}} = h(t=0) - h_{t\to\infty}$ is the amount by which the gel-vapour interface is estimated to fall at long times.

Fits according to Eq. 5.4 are shown in Fig. 5.5. The choice of fit is heuristic and we note that the time-dependence of $h(t)$ is more complex than this simple exponential form, particularly for long times. In the case of further sedimentation in timescales beyond those we access here [204], we expect that $h_{t\to\infty}$ may overestimate the interface height at long times. Notably, Eq. 5.4 fits the simulations better than the experiments, suggesting some difference in the mechanism of sedimentation between experiment and simulation. Also, the exponential fits are more accurate when the attractive interactions are stronger and the amount of sedimentation is less. Gels with stronger interactions show rapid initial sedimentation compared to weaker gels because the condensation is faster while the coarsening is slower. The sedimentation profile of the simulations appear to be sedimenting faster than the experiments. However, despite the absence of hydrodynamic interactions in the simulations the sedimentation profile agreement between experiment and simulation is noteworthy.

The sedimentation timescale τ_{sed} was extracted from the fits and is shown in Fig. 5.7. In Fig. 5.7, the dashed line through the simulation data is a straight line fit and the solid line through the experimental data has the same slope as the fit to the simulation data, however its intercept is fitted to the experimental data. We note

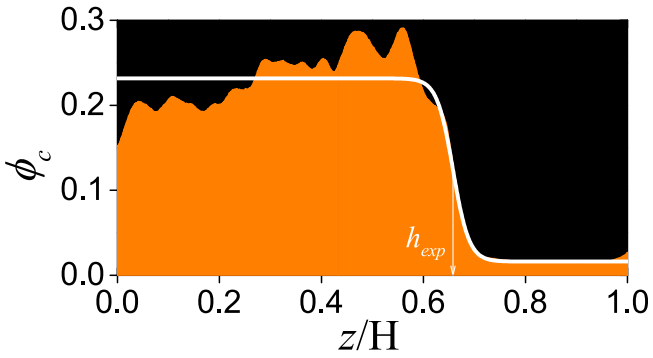

FIGURE 5.4. Sedimentation profile $\phi_c(z)$ for an experimental system with $u_{\text{AO}}^{\text{min}} = 3.2\ k_{\text{B}}\text{T}$ at time $t = 2.2 \times 10^5\ \tau_{\text{B}}$. The orange area represents the average lateral packing fraction as estimated from the intensity in the xz-direction of the sample. The white line is a fit according to Eq. 5.3.

that the τ_{sed} of the experiments is approximately three times longer compared to the simulations. This discrepancy can be attributed to several possible factors. One of the factors is the effect of hydrodynamic interactions which have been shown to affect the time evolution of gels without sedimentation [223, 224]. Also, there is a possibility that the initial conditions of the simulation do not match the state of the colloidal system of the experiments in the early stage. Another possibility in the simulations a finite periodic system is considered whereas in the experiments we focused on a small part of a much larger system. Attempts to match the vast system like in the experiments is not practical due to the high computational cost.

Figure 5.7 also shows that the sedimentation timescales undergo a small increase as the interaction strength is increased. However, the interaction strength impose a significant impact on the sedimentation timescale in the bulk systems; the system height is significantly larger than the gravitational length, particularly in the case of delayed collapse [24]. The different sedimentation characteristics shown in confined and bulk systems suggest a fundamental difference in the mechanism between the systems.

5.2.3 Structural behaviour upon coarsening

The structure within the gel is analysed by two methods. First, the network which coarsens as time progress is considered. The thickening of the network is also observed in systems where sedimentation is absent [150, 217, 228]. The analysis is done by determining the chord length [214]. Then, a particle resolved local structural analysis was done on the simulation data using the topological cluster

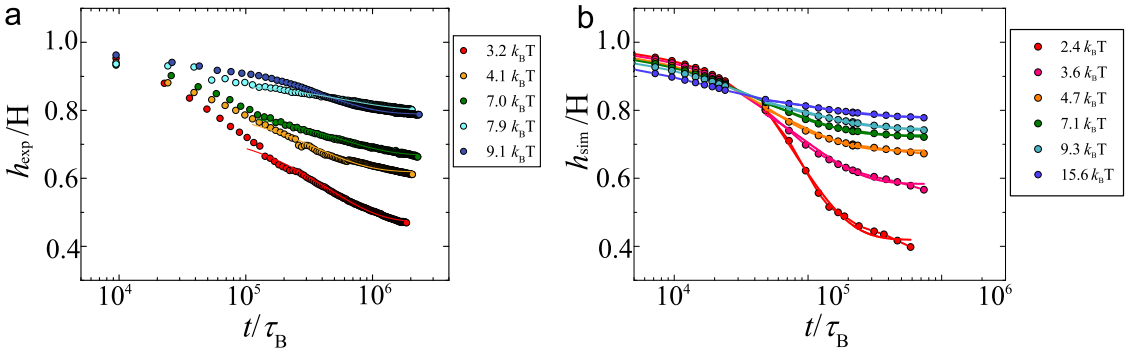

FIGURE 5.5. Figure shows the interface height normalised to the height of the system. Gel/vapour "interface" height plotted as a function of time. This height is estimated by fitting the function in (5.3) to a histogram of colloid density against height. Results from experiments are shown in (a); simulation results are shown in (b).

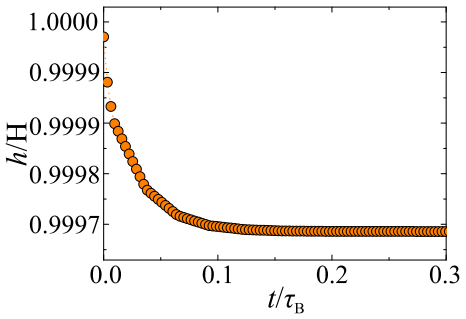

FIGURE 5.6. Sedimentation of the colloidal system in the absence of polymer. Here the Péclet number $Pe = 0.01$. Data determined from batch sedimentation [31].

classification [10] and common neighbour analysis [174]. The analysis from here on was carried out by Dr. Christopher Fullerton.

Chord length. — The typical size of the arms of the gel (Fig. 5.2) can be estimated by measuring the chord length, following [214]. First, to determine the arms of the gel, it is useful to measure the local density in the system. For a given point $\boldsymbol{R}_\alpha$, we define a (non-normalised) measure of local density as $n_\alpha = \sum_i f(|\boldsymbol{r}_i - \boldsymbol{R}_\alpha|)$. Here $f(r) = \mathrm{e}^{-r^2/\ell^2}$ is a (non-normalised) Gaussian smoothing function, with $\ell = 0.25\sigma$. A threshold $n = 0.3$ is taken, so R_α is in the gel if $n_\alpha > 0.3$ and in the sol if $n_\alpha < 0.3$ (The distribution of n is bimodal so results depend weakly on this threshold). This analysis was carried out for a 3d cubic grid of points with spacing 0.5σ. A chord is a straight line that cuts through an arm of the gel. Since chords may have any direction, as a representative sample, we identify chords that run along the x, y, and z directions. We achieve this by running through the cubic grid (along the lattice

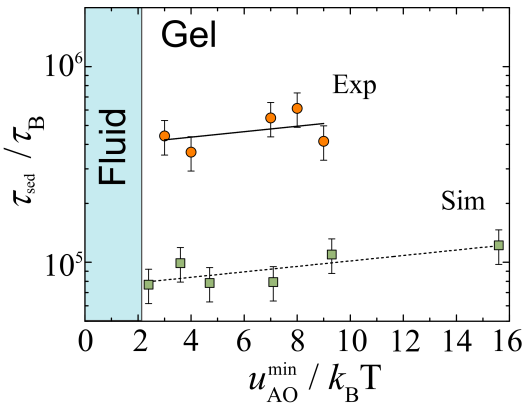

FIGURE 5.7. The sedimentation timescale from experimental and simulation data τ_{sed} as a function of interaction strength.

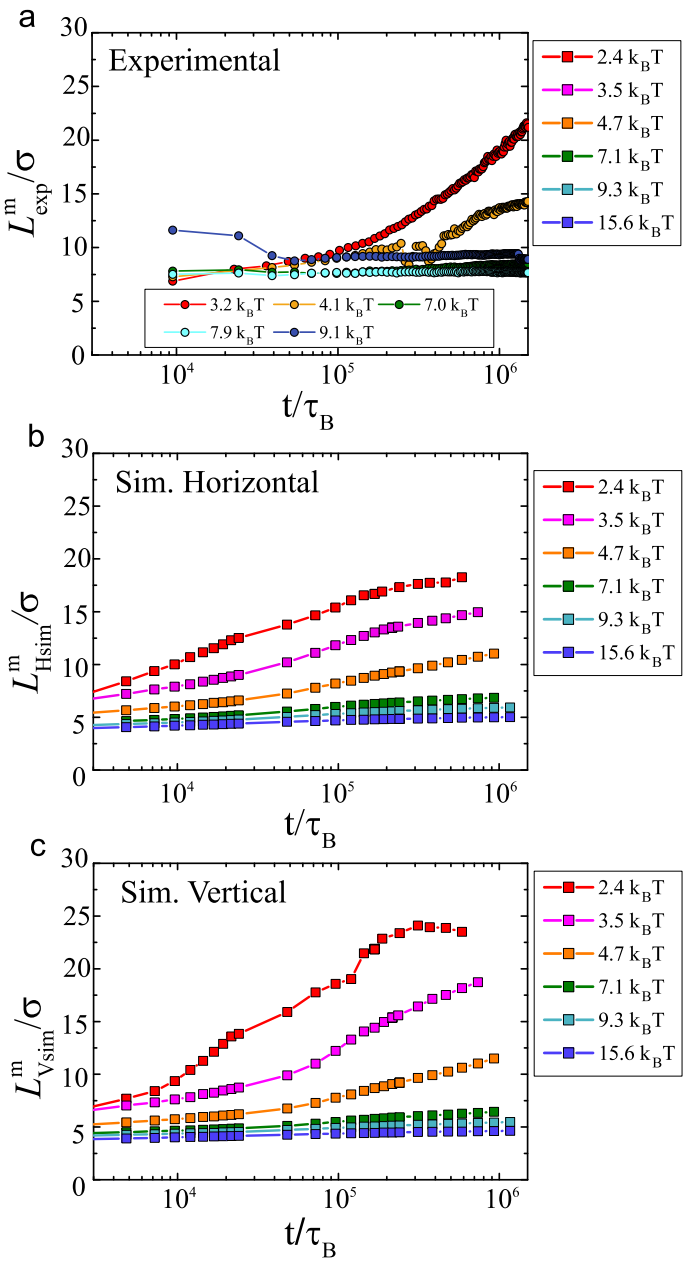

FIGURE 5.8. The average chord length (mass weighted) was measured (a) in the horizontal direction in the experimental system at the same state points in Fig. 5.5. (b) in the horizontal direction (perpendicular to the direction of gravity) (simulation), (c) in the vertical direction (the direction in which gravity acts) (simulation). Legend on right pertains to (b) and (c).

axes) and identifying all sets of contiguous cells for which $n > 0.3$. We record the length of each chord.

Chords measured in the x and y directions are the same (as gravity acts in the z direction only), but we separate horizontal chords (aligned along the x and y directions) and vertical chords (aligned long z). To estimate the typical size of a horizontal chord, imagine choosing a particle at random and measuring the chord containing that particle. If the length of the jth horizontal chord is H_j then the average length of a horizontal chord chosen in this way is

$$L_{\mathrm{H}}^{\mathrm{m}} = \frac{\sum_j H_j^2}{\sum_j H_j} \tag{5.5}$$

where the superscript 'm' indicates that the average is mass-weighted. (That is, this average could equivalently be estimated by choosing particles at random and measuring the associated chords. On the other hand, averaging the length of a randomly chosen chord would give a different result. The mass-weighted average focuses attention on the chords which contain the majority of the particles and avoids numerical artefacts associated with large numbers of small chords.)

This typical chord length is shown in Fig. 5.8 for both experimental and simulation data. At long times the chord lengths for the experimental systems are significantly larger than those in the simulations. However, except for this difference in overall scale, the time-evolution in both experiment and simulation appears similar.

There are several possibilities for this observation. Previously mentioned, the difference between the experiments and simulation might due to the effects of hydrodynamic interactions [223, 224]. Another possible factor is the lateral size of the simulation box which could influence the size of the networks formed. Previous simulation studies have reported the need for large systems in order to avoid finite size effects on the gel structure [214, 228]. However, that the lateral system size $L \approx 28\sigma$ is comparable with the range over which experimental data was taken. Notably, in the gel regime, increasing attraction strength appears to lead to a suppression of domain growth in both experiments and simulations, as was previously reported [150, 228, 229].

5.2.4 Local structural analysis

It has been reported that changes in the local structures occur due to gelation [117]. Therefore, the local structure changes in the simulations of sedimenting gels are considered using two methods of analysis: the Topological Cluster Classification (TCC) [10] and the second is a common neighbour analysis (CNA)[174]. Details of this method have been discussed in Chapter 3. This analysis was carried out by Dr. Christopher Fullerton. Despite the density difference in the sedimentation profiles

very little vertical variation was found in the population of local structures when the analyses were performed as a function of the height within the gel. Thus, the following result shows the population of local structures averaged across the whole system.

The proportions of particles that participate in clusters of each type and the clusters identified using the TCC are illustrated in Fig. 5.9. The populations of selected local structures that have been deemed important in gelation [117, 180, 191]. Using the TCC, particles may be identified in more than one type of structure, so the total across different types may exceed one. Also, in Fig. 5.9 shows the average number of 142 bonds that a particle participates in for different well depths. Here, a particle participates in a 142 bond if it is one of the two particles forming the central bonded pair. The 142 bonds are found in large numbers in both the HCP and FCC crystals. Thus, are interpreted as a crystal precursor.

In Fig. 5.9 all state points show the same behaviour. At the beginning there are few structures and then upon condensation, local structures start to form started with the 5-membered particles cluster; the bitetrahedron. This also has been seen previously in study of systems with the absence of sedimentation [180]. The proportion of the 10 particles cluster (defective icosahedron) shows an increase after some time, as was previously reported in [180, 224].

A significant degree of crystallisation at longer times is found in the system after a weak quenching. This was observed previously in similar systems [39]. The crystalline order measured by the TCC shows an order of magnitude later in time compared to the appearance of crystalline pre-cursor 142 bonds measured by the CNA. This is due to the fact that 142 bonds has a lower degree of local order than the 13 particles clusters identified in the TCC analysis as FCC or HCP. Upon deeper quenching, suppression of crystallisation is observed within the timescales considered here which is consistent with previous work [39, 95, 117, 180, 191]. Considering the varied state points, the temporal changes of local structures of the sedimenting gels show some resemblance to that of quiescent gels [180].

We have shown that in a vertically confined system without the addition of polymers, it displayed a strikingly different behaviour than a bulk system. In a bulk system with similar conditions, batch settling would definitely occur and the addition of polymer would stabilise it form sedimenting for a period of time. However, here in a system that was vertically confined, the addition of polymer induced the sedimentation behaviour. While the rate of sedimentation was observed to decrease as the attractive forces increased in the confined system, it did not display the accompanying delayed collapse commonly observed in the bulk system.

In Chapter 2, the possible mechanisms for sedimentation of arrested network

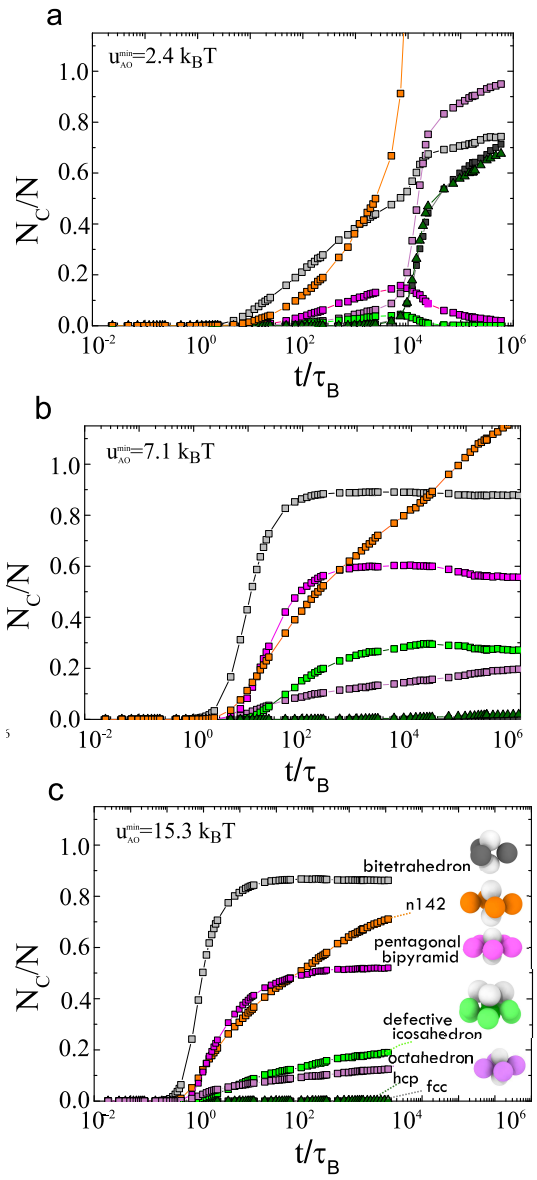

FIGURE 5.9. The local structural changes in simulations as time progress are shown. Three state points were considered where the effective AO interaction strengths are $u_{\mathrm{AO}}^{\mathrm{min}} = 2.4, 7.1$ and $15.3\, k_BT$. The '142' clusters are detected using the common neighbour analysis, while other structures are identified with the topological cluster classification (TCC). For TCC clusters, the fraction of particles that participate in at least one cluster of the relevant type is shown using (N_C/N) (therefore, one can have $N_C/N \leq 1$). As for the 142 clusters, N_C/N is the average number of 142-bonds in which a particle participates (there is possibilities of $N_C/N > 1$ where for a perfect fcc crystal one would have $N_C/N = 12$).

in a bulk system were discussed. The appearance of solvent channels in the arrested network has been suggested to be one of the mechanism process [115, 143]. These channels appear, allowing solvent to flow out of the network and inducing arrested network deformation. After a latent period, the various solvent channels meet and started to straightening up, increasing the sedimentation velocity [144]. Another outlined mechanism was creep sedimentation. This is similar to the above-mentioned mechanism where the solvent is flowing out of the network. However, instead of forming channels, it is induced by the gravitational stress compressing on the network, compacting it and then undergoes delayed collapse as was also mentioned in the previous mechanism.

For our system, the vertical confinement may have accelerated the mechanisms processes leading to the rapid sedimentation passing the delayed collapse phase unlike in the bulk systems. At this point of work, to suggest that one mechanism plays a major role over the other is precipitous due to lack of detailed investigation in that regard. Here, the role of vertical confinement has enable us to carry out simulation studies comparable to experimental systems. In order to translate the size of the usual bulk size into simulation accompanied together with the effect of gravity would require a higher and expensive computational cost.

5.3 Summary

We have carried out a combined experimental and simulation study of colloidal gels undergoing sedimentation. The vertical confinement of these systems profoundly affects their sedimentation behaviour. For confined colloidal systems which do not sediment in the absence of gelation the addition of polymers and the resulting gelation induced sedimentation. Also, unlike in bulk systems, delayed collapse was not observed here.

The Brownian dynamics simulations provided a reasonable description of the time-evolution of the system given that the simulations do not feature hydrodynamic interactions. The major differences in behaviour between simulation and experiment are that the simulations appear to sediment rather faster than the experiments. In the previous chapter, the structural changes of an ageing quiescent colloid-polymer system were studied. Here, the structural analysis on the dimensions of the gel network suggests that the networks in experiments are rather coarser at long times. This may be related to some intrinsic difference in the dynamics, or to a finite size effect in the simulations, or to incomplete homogenisation of the experimental system prior to gelation.

We note that the development of coarse-grained theoretical models is possible

based on the simulation studies as presented in this work. This could potentially become the solution to macroscopic phenomena which are not accessible in these confined systems such as delayed gel collapse [24] and are therefore beyond the reach of direct simulation. For this reason, development of such coarse-grained models would form a major step forward in the understanding and modelling of these important materials.

Finally, the local structure of the simulated gels was also considered and marked similarity to the structural evolution found in non-sedimenting gel systems. Based on Fig. 5.3(b), the simulated system condenses into a percolating network before any significant sedimentation occurred. It can be suggested that the local structural changes of the system occurring in short timescales were disconnected from sedimentation. Results shown in Fig. 5.9 and also in Chapter 4 section 4.2.4 are also consistent with this interpretation. The local structural changes that occurred shown similar pattern, regardless of the sedimentation.

CHAPTER 6

Temperature effects on colloid-polymer mixtures

The addition of nonadsorbing polymer to a colloidal suspension with hard sphere interactions introduce effective attractive interactions between the colloids. The strength and range of the attractive interaction can be controlled by changing the polymer concentration and molecular weight [32, 33, 90, 93]. In this system, increasing the amount or polymer concentration will in turn increases the attractive interactions strength. This attractive interaction strength brings about effects similar to quenching. Thus, the effective temperature of the colloid polymer system is inversely proportional to the attractive interaction strength and as we have also demonstrated in previous Chapters(Chapters 4 and 5), the effective temperature was varied by changing the polymer concentrations (i.e. changing the interaction strengths).

The polymer fugacity z_p as presented in Chapter 2 is equal to the number density of ideal polymers in the reservoir. This sets the effective temperature for the system as was previously reported in experiments [94]. Hence, the predominant reaction of the system to the change of temperature is set to the response of the polymers because of hard sphere interactions between the colloids are athermal i.e. independent of temperature. In good solvent conditions, the polymers become larger (have bigger R_g) compared to when they are in theta solvents. This expansion behaviour can also be seen when the polymers are heated from their theta temperature. A similar expansion from when the polymers are in theta solvents where $R_g \sim N^{1/2}$, to good solvent conditions where $R_g \sim N^{3/5}$ (here N is the number of monomers in the chain [230]) is expected in terms of temperature. The effect of temperature on the radius of gyration is shown in Fig. 6.3. The increasing size of the

polymers has some effect on the strength and range of interactions in the colloid polymer system. First, the colloid-polymer size ratio q increases and the polymer volume fraction ϕ_{PS} also increases. The increasing polymer volume fraction leads to a stronger attractive interaction (similar effect as quenching). Thus, we may say that heating effectively cools the system and cooling effectively heats the system. This paradoxical effects have been used to instigate phase transitions in colloidal rods and polymer mixtures [231] where melting was induced from cooling.

The self-assembly process requires a balance between a thermodynamic drive towards assembly of the ordered equilibrium state and kinetic accessibility of experimental time. The former indicates that the ordered equilibrium state requires strong attractive interaction between the assembling units. This factor is accommodated by low effective temperature and strong bonds. Meanwhile, the second factor requires that the equilibrium ordered state is accessible within experimental timescale which favours high effective temperature and weak bonds. The two requirements for effective self-assembly have been studied using fluctuation dissipation ratios (FDR). These ratios measure how effective is the equilibrium fluctuation dissipation theorem (FDT) in nonequilibrium systems. Using the above mentioned measurements, it can be predicted which systems will undergo effective self-assembly and which systems will fail. This prediction has been made using viral capsids and sticky disks [104].

More recently, the prediction has been used in model colloid systems [39]. More interestingly, this prediction was employed in tuning the interaction strength of a model colloid systems with short range attractive potentials [1, 183]. In their work, the attractive interaction strength was changed based on a feedback system using the FDR measurements. Starting from interaction strengths where no self-assembly took place or system will get kinetically trapped, they employ a feedback scheme which measures how far the system forms a good self-assembly and then tuned the interaction strength until good self-assembly is obtained.

In this chapter, we employed the colloid polymer system because of the polymer response to temperature enabled us to emulate the tuning interaction strengths as in the systems studied with feedback scheme [1, 183]. By lowering the effective temperature close to T^{θ}, the polymer R_{g} is decreased. In turn, the deeply quenched system is 'warmed-up' bringing it to a more shallow quenched region. Similar to what is proposed in the feedback scheme and discussed in previous Chapter 2, structural rearrangement is expected in the shallow quenched system due to bond reversibility, and eventual better self-assembly will takes place when the interaction strength is brought back to the original temperature. The effective structural rearrangement in such systems were presented in both Chapters 4 and 5. The results of

changing the temperature are shown in the following sections.

6.1 Method

6.1.1 Temperature stage setup

The temperature change investigations were carried out using a temperature stage fitted to a confocal microscope. The temperature stage consists of a Peltier cooling chip and water cooled heatsink, is shown in Fig. 6.1. Thermoelectric cooling is based on the Peltier effect that creates a heat flow at a junction between two different types of materials. A thermal ribbon sensor is attached on the heat dissipating surface of the Peltier chip in order to follow the temperature changes during the experiment. The cooled surface of the Peltier chip is placed on the water cooled heatsink with a small layer of thermal compound to enhance thermal conductivity. The heatsink is connected to a water refrigated circulator from which temperature of the water supplied is controlled.

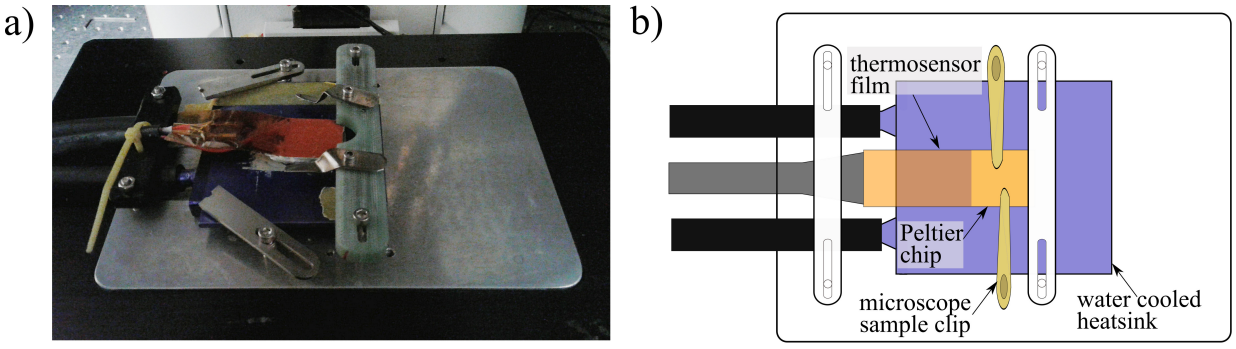

FIGURE 6.1. A photo and a sketch of Peltier chip and water cooled heatsink used in the temperature stage setup.

6.1.2 Experimental details

The experimental system is sterically stabilised polymethylmethacrylate (PMMA) with a diameter σ=1.08 μm. For this work only cis decalin was used as solvent. The colloidal polydispersity is approximately 4.6% as determined with scanning electron microscopy (SEM). A colloidal gel was obtained by adding nonadsorbing polystyrene polymer with molecular weight $M_w = 8.5 \times 10^6$ g/mol, leading to a polymer-colloid size ratio of $q = 2R_g/\sigma = 0.307$, where $R_g = 166$ nm is the estimated polymer radius of gyration at room temperature (25°C) and corresponds to $R_g^\theta = 95$ nm under θ conditions [232]. The overlap concentration at room temperature is

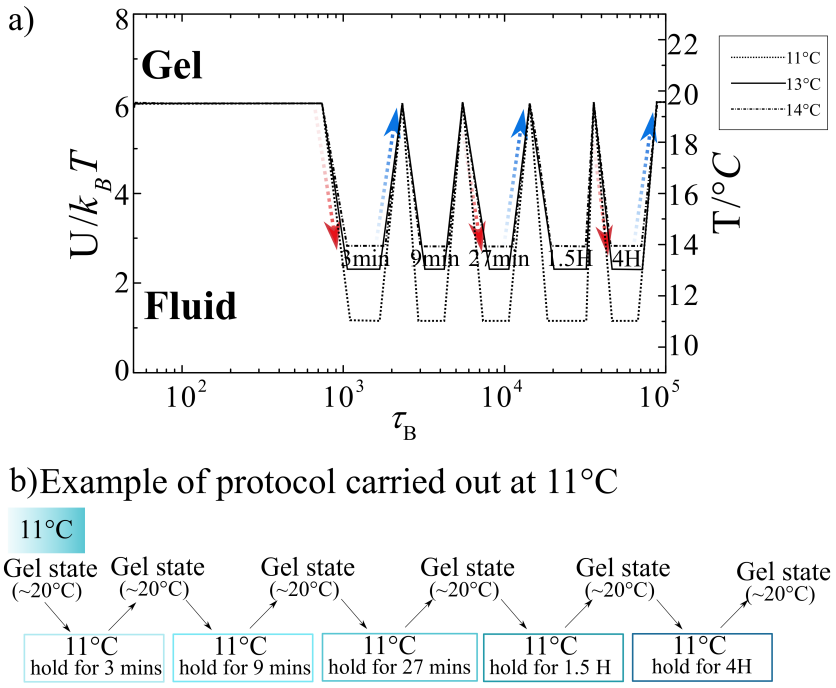

FIGURE 6.2. A sketch (a) showing the temperature cycling protocol carried out at 11°C, 13° and 14°C, and (b) gives an example of protocol details at 11°C. Note that the images are obtained when samples are in the gel state point.

determined to be at 2.41 g/L. The T^{θ} of polystyrene in cis decalin is measured to be at 10° [151]. The images were obtained using Leica SP5 confocal microscope.

In this work, the Brownian time $\tau_B$which was defined previously as the time scale for a particle to diffuse its own diameter is used as the unit of time. For the parameters in this work the Brownian time is $\tau_B = \sigma^2/24D = 0.41$s, where $D = k_B T/(3\pi\eta\sigma)$ is the Stokes-Einsten diffusion constant where η is the solvent viscosity.

Each sample is then transferred into cells as described in Chapter 3 subsection 3.4.2. Once the sample is in the cell, the openings are sealed with epoxy resin. We started the time measurement from when the sample is sealed inside the cell. The images of the colloidal gel were attained with a size of 28μm in x and 28μm in y axes. After recording several images of the gel sample at around 20 °C, the sample is then cooled close to the theta temperature T^{θ}. Then, the sample is maintained at the low temperature for 3 minutes and then the temperature is raised back to the starting temperature. We recorded the images after the first cooling and cooled down the sample again and held it there for 9 minutes. The temperature is increased back to the starting temperature and the images after the second cooling are obtained. The longest time duration where the gel is held close to the $T^{\theta}$is 4

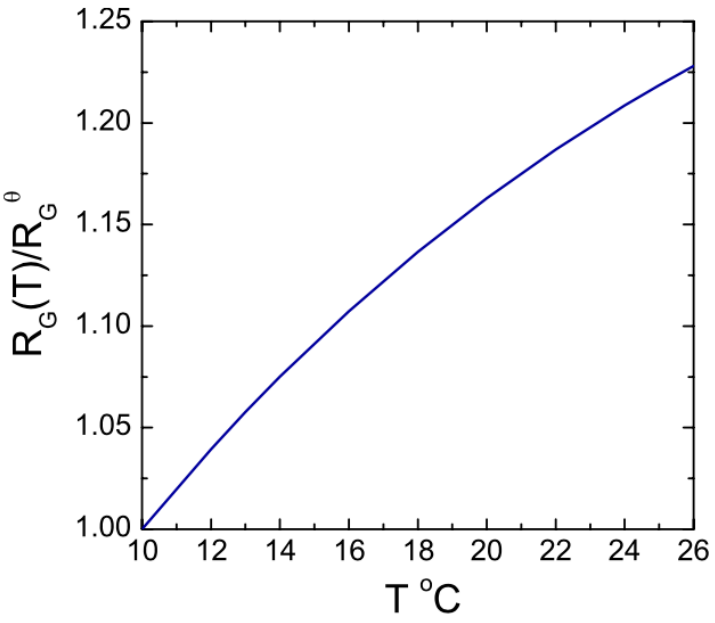

FIGURE 6.3. The effects of temperature to the radius of gyration of polystyrene. This is fit of equation 6.1 to experimental data [151]. This is adopted from [95]

hours. The details of the temperature cycling protocol is shown in Fig. 6.2(a). We ran the protocol at 3 different temperatures: 11°C, 13 °C and 14 °C, where the size ratios are $q = 0.188, 0.211$ and 0.221 respectively. Every time the sample is cooled, it is maintained at the above mentioned temperatures. As an example, the protocol performed at 11°C is illustrated in Fig. 6.2(b). In order to compare the effect of temperature on gelling systems, we have also observed the structural changes of a sample without temperature cycling protocol as control.

From the images, we obtained the 2d coordinates from particle tracking and analyse the degree of crystallinity in the system using the bond order parameter ψ_6. The details of this measurement has been discussed in Chapter 3 under subsection 3.7.4. The results of the structural analysis is presented following the summary of the phase diagram of the colloid polymer system used in this work.

The polymer R_g changes induced by changing the temperature is shown in Fig. 6.3 [95]. They fitted Eq. 6.1 to experimental data [151]. In the equation, $\tau = 20°$ C.

$$R_g(T) = R_g^{\theta}\left[\sqrt{2}\left(1 - \exp\left(\frac{T^{\theta} - T}{\tau}\right)\right) + 1\right] \tag{6.1}$$

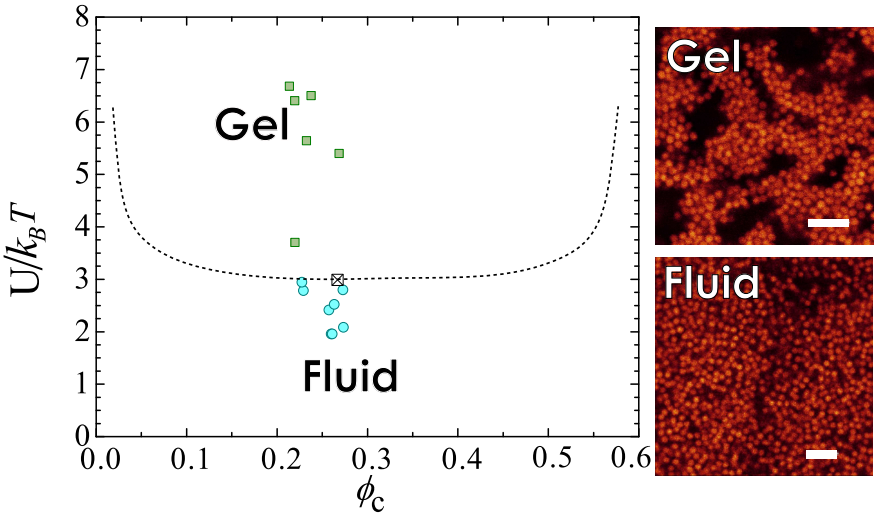

FIGURE 6.4. Phase diagram at room temperature in colloid volume fraction ϕ_c and minimum depth of attractive interaction based on AO model U. Symbols showing experimental data; blue circles are fluid and green squares are gels. The ⊠ is the AO critical point based on second virial coefficient B_2^{*AHS}. The dashed line is a guide to the eye for the spinodal line. The scale bars represent 5.0 μm.

6.2 Results and discussion

Figure 6.4 shows the state of the colloid polymer system used in this work at room temperature. The phases shown correspond to phase diagrams for colloid polymer system with $q = 0.307$ at room temperature 25°C, where the spinodal line is relatively flat. The liquid-vapor critical point is determined from the extended law of corresponding states [123] at $B_2^* = -1.5$. The critical point is estimated to be at ϕ_c=0.27 with interaction strength $u(\sigma) \simeq 3\ k_B T$ estimated from [95, 195, 196]. From the phase diagram, we used gel sample that is close to the criticality to perform temperature cycling protocol. The images at each phase are also shown in Fig. 6.4.

6.2.1 Structural analysis

The degree of crystallinity in the colloid polymer system is measured using the local bond order orientation ψ_6. The details of this measurement are given in Chapter 3 subsection 3.7.4. The ψ_6 value ranges between 0-1 where 1 represents a perfect crystalline ordering while lower values represent weaker magnitude of local crystalline ordering (higher degree of disorder).

Figure 6.5 shows the ψ_6 results after temperature cycling protocols and also for control. The (normalised) histograms of ψ_6 is used for comparison purposes. Based

on the figure, indeed local ordering increases as time progress. This is evident for all systems particularly for control; where no temperature changes occurred. The amount of disordered arrangement that was evident before temperature cycling protocol showed a decrease at the end of the protocol. Limiting our observation to the individual ψ_6 distribution after temperature cycling protocol presents a promising pattern that crystallinity indeed increases. This is based on the assumption that structural rearrangement occurs at the low temperature when gel sample is brought close to criticality. At this temperature range, 11-14 °C the interaction strength $u(\sigma)$ is closer to the $u(\sigma)$ reported in Chapter 4 where crystallinity increases with time. Based on previous studies, in short ranged attractive systems with intermediate $u(\sigma)$ bonding reversibility is possible leading towards crystallinity. Therefore, a higher degree of ordering is expected after every protocol compared to control. However, this is not the case. From Fig. 6.6, it is clear the ψ_6 number after temperature cycling protocol shows no significant improvement compared to control. The amount of crystallinity is higher in the control sample at room temperature rather than in the samples that underwent temperature cycling protocol. Interestingly, samples that underwent the temperature cycling protocol at 14°C gives about the same degree of crystallinity as control. Several factors can be suggested contributing to this effect.

One of the reasons may be the temperature cycling protocol is too short to allow the gel network obtaining long range order evident in crystals. However, the same time duration was also used for the control, so this could not be a strong factor. Another possibility is the temperature cycling protocol disrupts the gel sample in its pathway towards local ordering. The protocol in fact, forces the gel sample towards disordered arrangement thus hindering crystallinity.

6.2.2 Experiments with mixtures of solvents systems to overcome sedimentation and image quality

One of the challenge in obtaining images from this work is sedimentation. If we carry out the experiment using cis-decalin and cyclohexane bromide the solvent mixture typically used to match the density of the colloids, the T^{θ} needs to be below 80° C which is impossible to reach using current experimental setup. However, in our attempt in preventing rapid sedimentation and also better imaging quality, we have tried using other solvent mixture: cis-decalin/tetralin/tetrachloroethylene of 18/22/60 (w/w) ratio.

Using this solvent mixture, the colloid-polymer system remained as arrested network until the temperature reached 0.1° C. Even at this low temperature the gel branches did not diffuse to liquid state completely, instead 2 states were evident which is known as polymer thermophoresis. This is shown in Fig. 6.7. The

temperature-dependent osmotic pressure gradient was observed in the solvent layer surrounding the polymer's monomer units. The polymer-solvent interactions led to the slight changes in the concentration of solvent molecules. In previous work, these interactions had shown clear significant role in polymer thermophoresis [233]. The interaction constant of polystyrene has been calculated using its thermophoretic mobility in different solvents. Consequently, in nonpolar solvents the thermophoresis of polystyrene is greatly influenced by the London dispersion forces. These dispersion forces play a major role over the dipole-dipole interactions which are insufficient to produce the required interaction energy. The issue in replicating this experimental result was the time duration to reach 0.1° C took about 3 hours and an attempt to reheat the sample back to room temperature took about 40 minutes. This rendered the temperature cycling as a trivial effort in order to improve self-assembly since a single cycle of this suspension is about the same time for a system to self-assemble based on the results in Chapter 4.

Additionally, the solvent mixture of cis-decalin and cyclohexane bromide (CHB) in various ratio was also tested in order to prevent rapid sedimentation and improving image quality simultaneously. However, all of the arrested network of colloid-polymer system did not show any melting when the temperature were cooled down to T^{θ}. Fig. 6.8 gives an image of arrested gel network in 50/50 (w/w) cis decalin and CHB solvent mixture at 6°C.

After failed attempts with the solvent mixtures, we also attempted to use core shell PMMA particles for better imaging and prolonged experiment duration. The size of the PMMA particles greatly influence the sedimentation rate, Brownian time and therefore the overall experiment duration (as was discussed in Chapter 2). However, using only cis decalin as a solvent causes the images of the particles harder to capture due to the light refractions. Therefore, core shell PMMA particles are convenient in overcoming this issue. However, synthesising smaller PMMA particles (<0.8 μm) demanded a compensation in the monodispersity [234]. This leads to PMMA particles with the ideal diameter for the experiment requirements (<0.5 μm) but failed to form crystalline ordering due to its polydispersity.

6.3 Summary

We have shown temperature cycling protocol carried out at 14°C improved the ordering of the colloid-polymer system. This result is consistent with our expectation and is in line with the results reported by [1]. Indeed, the ψ_6 of the control is higher than the samples after temperature cycling protocol at 14°C, this might offer an interesting avenue to be further probed in future works.

Additionally, when the effective temperature is decreased, the expected outcome is the bonds between the particles are 'loosen' just enough that particles rearrangement might be possible. However, in this work instead of observing a rearrangement of the gel network during the 'heating', we observed that the network was broken to several pieces of clusters. Therefore, the sedimentation rate of these diffusing clusters actually increased and when it is brought back to its quenched temperature, what we have is a more compressed kinetically trapped network from the 11 and 13°C protocol.

In previous work reported in [117], the bond order parameter ψ_6 was used to show sixfold symmetry in a 3d system. Indeed ψ_6 had been shown to work well in measuring crystallinity in a 3d system to a certain degree, in our work we presume that ψ_6 might not be as susceptible to our system. The ψ_6 measurements were taken from 2d data when our system is a 3d system therefore, significant structural changes might have been overlooked in the analysis.

Other widely used measurements in detecting structural changes for example the static structure factor $S(k)$ and pair correlation functions $g(r)$ have been shown to miss some structural changes in similar models of colloid polymer systems [180]. Moreover, in Chapter 4 changes in the $g(r)$ appeared to be less significant than in local structures detected using the TCC, the higher-order structural analysis method. Therefore, it can be suggested here that 3d analysis of the system will detect the more subtle structural changes of our system.

One of the main challenges we faced in this work is sedimentation of the colloid polymer system. In order to overcome this issue we proposed two alternatives. First, the use of colloidal particles in much smaller diameter. This could reduce the sedimentation rate of the system offering longer temperature cycling period and in turn improving the particles rearrangement. Finally, the use of a novel solvent system which is susceptible for temperature cycling within the usual experimental protocol. We have shown in this work, the usual PMMA density matching solvent mixture is not feasible for the temperature cycling study. On the other hand, the use of a single solvent, cis decalin in our case, led to poor imaging in the confocal due to refraction whereby, a higher number of iterations was needed in order to capture the images. This limits the observation time thus missing any critical structural changes. A novel solvent system could also contribute in overcoming the sedimentation issue during the temperature cycling period. The idea of being able control the self-assembly by changing the interaction strengths of the system is straight forward enough to work but the complex issues in the experimental environment are limiting our effort.

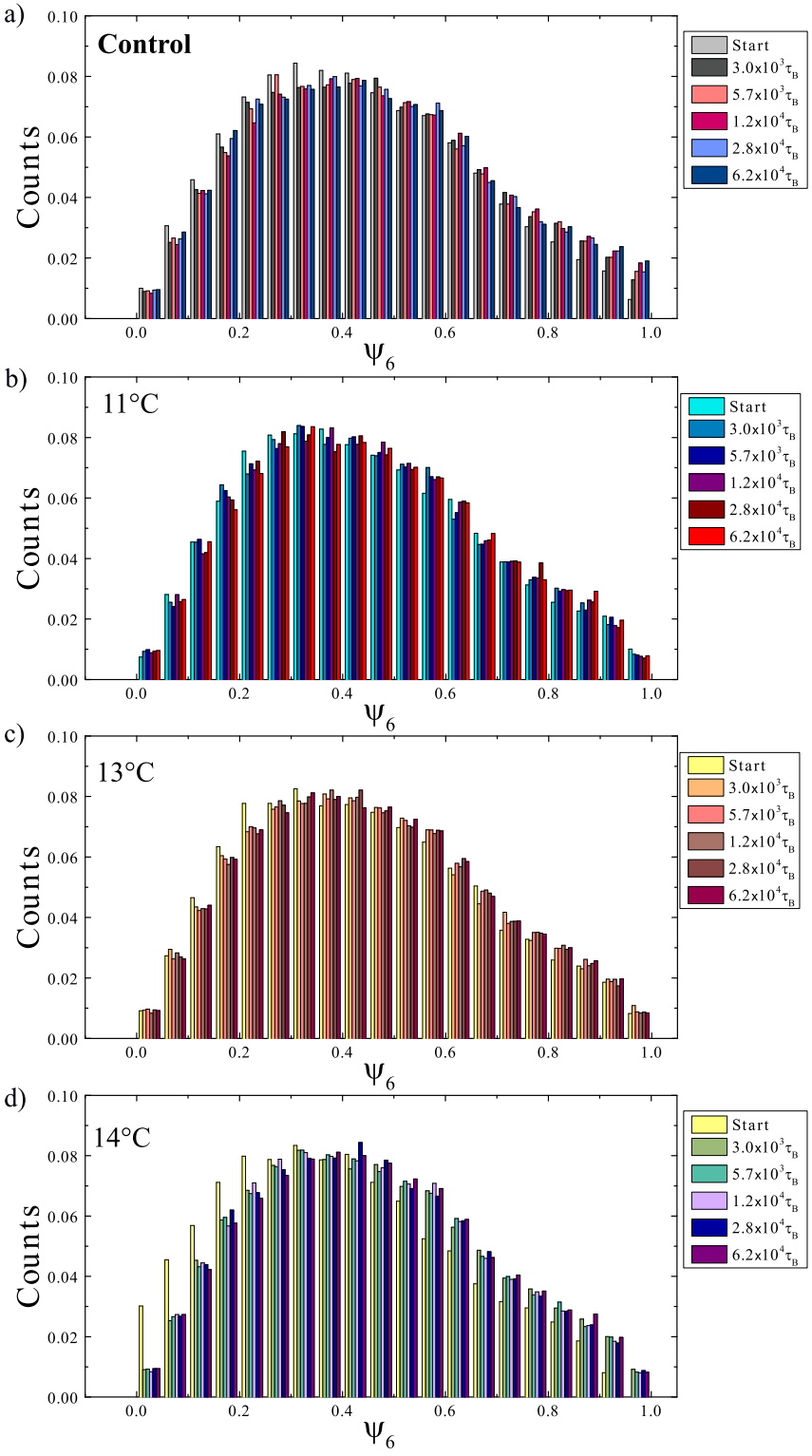

FIGURE 6.5. The ψ_6 analysis of gel sample (a) without temperature cycling (control) and (b)-(d) after protocol at indicated temperatures in figure.

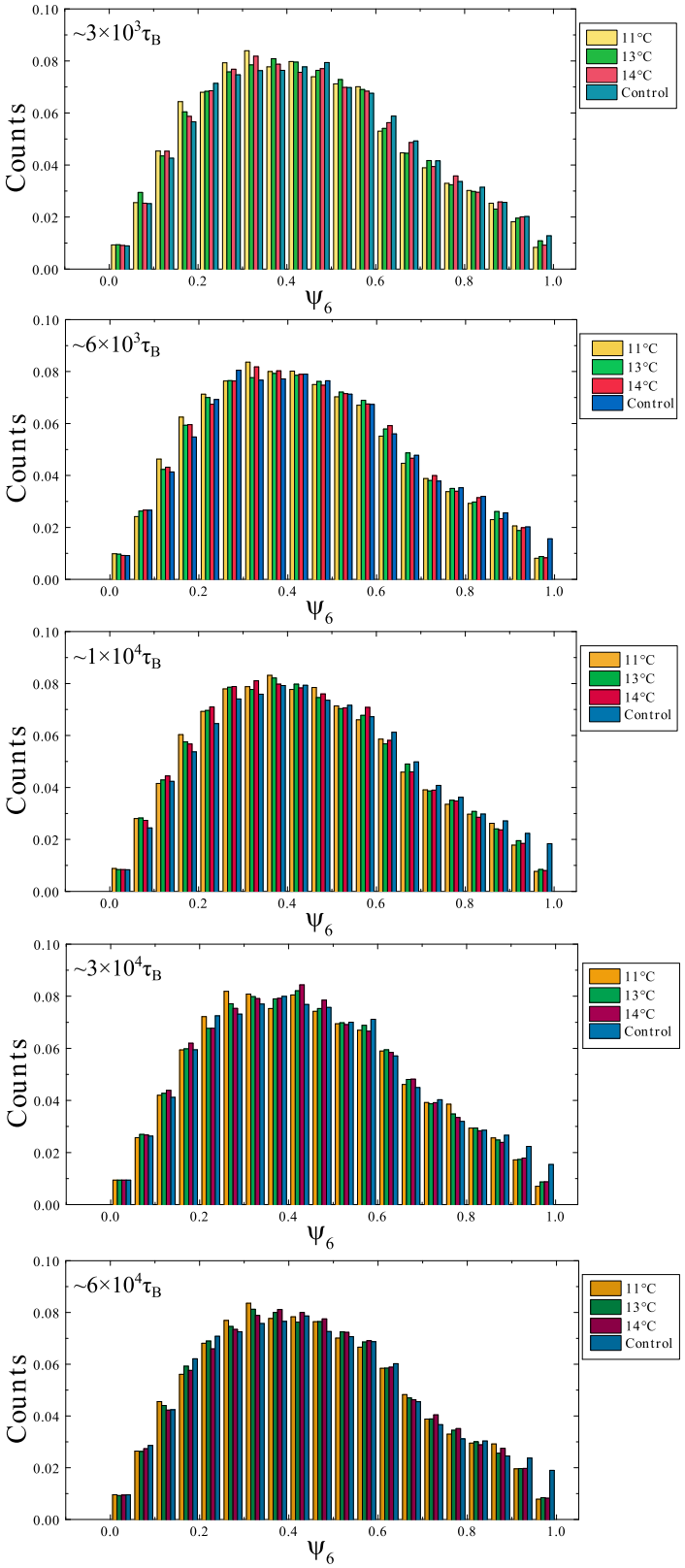

FIGURE 6.6. Comparisons of ψ_6 analysis of gel sample without temperature cycling (control) and after protocol at 11°C, 13°C and 14°C at different times.

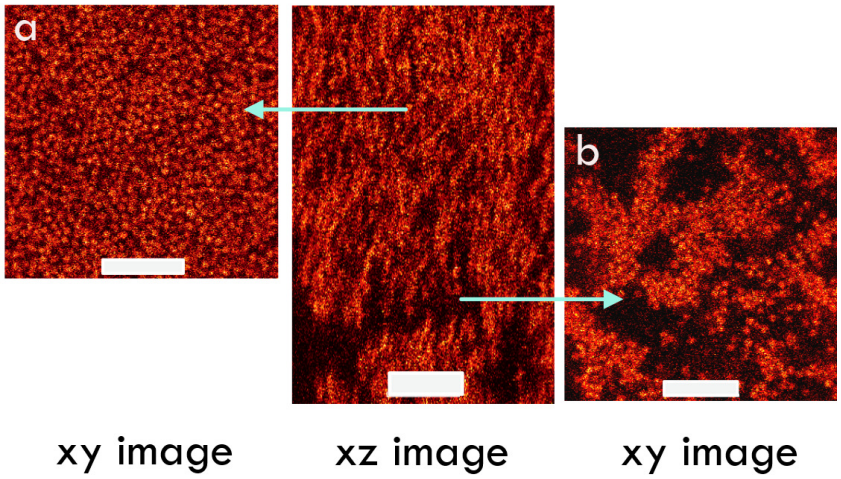

FIGURE 6.7. Figures showing the co-existence of 2 state points in gel at T = 0.1°C. The white bars in figures represent 10 μm.

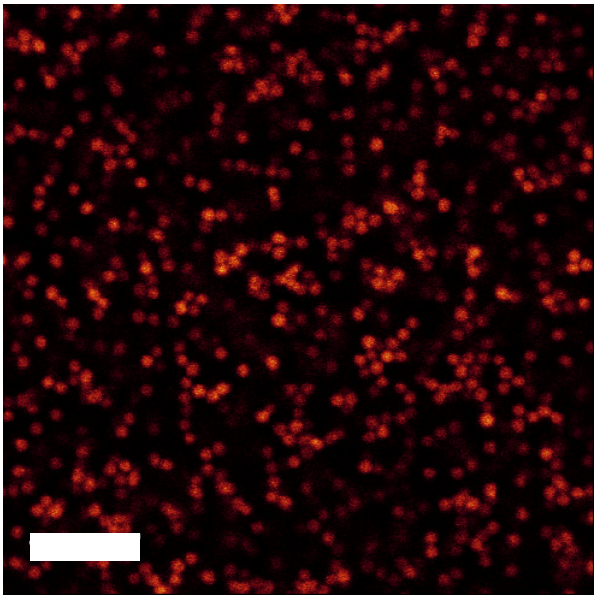

FIGURE 6.8. The arrested network remained even after surpassing the T^{θ} for cis decalin. Image was taken at 6° C.

CHAPTER 7

Conclusions

The work in this thesis describes the structural evolution of colloid polymer systems reaching equilibrium ordered states. Primarily, confocal microscopy was used throughout this work in order to investigate the local structural changes. The addition of nonadsorbing polymer induces aggregation in the colloidal dispersion by creating attractive interaction potential between the colloids. Otherwise, the colloid-colloid interactions are described by hard sphere potentials. The colloid polymer mixture can be considered as a one component system and the effective interaction is mediated by the polymer as first proposed by Asakura and Oosawa [15, 16] and later by Vrij [17]. We employed the Asakura-Oosawa model in describing the effective interaction strengths in our work. In addition, in chapters 4 and 5 we utilised Brownian dynamics simulations in examining the structural evolution of the colloid polymer systems in each chapter.

The preceding chapters discussed the structural evolution of the dynamically arrested network towards equilibrium states. In each chapter, the development of local structures towards crystallisation in the colloid polymer system was investigated. The local structures were analysed using higher-order structural analysis: the topological cluster classification (TCC) and common neighbour analysis (CNA) for chapters 4 and 5. Meanwhile bond order parameter was employed in chapter 6. In chapter 4, the colloid polymer systems were density matched, therefore the gravitational field was eliminated to a certain degree. The chapter focuses on particle-resolved analysis in detecting subtle changes in gels transforming from initial locally amorphous structure to being locally crystalline. In chapter 5, not only was there gravitational field, the confined gel displayed a behaviour that was

not previously observed in gels contained in large vessels. Finally, in chapter 6 we employed the polymer response against temperature to control the interaction strengths of our colloid polymer system in order to create better self assembly. This work is expected to obtain similar results as reported in simulation [1, 183] where changing the interaction strengths during self assembly gives better and larger crystalline clusters. However, the results obtained were not in agreement to the previous simulations work and defied our initial expectations. The changing of interactions in our work, had produced more disordered structures based from the bond order parameter ψ_6 analysis.

7.1 Crystallisation in colloidal gels: a particle-resolved analysis

In chapter 4, we have analysed the structural evolution of colloid polymer systems with different interaction strengths from experiments and simulations. Previously, it has been reported that gels can form ordered network both in experiments [181] and simulations [180]. On the way to forming locally crystalline structures, subtle changes in gels are difficult to detect in widely used pair correlation function $g(r)$ [117, 191, 192] and structural static factor $S(k)$ [180].

Crystallisation in both the simulations and experiments were characterised using the pair correlation function $g(r)$ and topological cluster classification (TCC) to investigate the changes in local structures of the gels. In dynamically arrested network with intermediate interaction strength $u(r)$ structural rearrangements within the networks were evident (both in experiments and simulations), based on the increasing number of crystalline structures and depleting number of 5-fold symmetry clusters as time progressed. This is in agreement with previous studies on self assembly of short ranged attractive systems which reported the possibility of bonding reversibility in systems with intermediate $u(r)$. Whereas, colloid polymer systems with higher $u(r)$ retained high numbers of 5-fold symmetry clusters at the end of experiments and simulations. These clusters has been reported to hinder the formation of crystalline ordered structures [75, 199–201]. Here, we have successfully shown the particle resolved investigation of local structural evolution in gels using higher-order structural analysis.

7.2 Effects of vertical confinement on gelation and sedimentation of colloids

The gravitational field effect on the colloid polymer system in chapter 4 was eliminated to a certain degree by using density matched solvents. In chapter 5, the effect of gravitational forces was present since the colloid polymer was suspended in only cis decalin. The sedimentation behaviour of our experimental systems were translated to simulations. The results from simulations were used for structural analysis using TCC and common neighbour analysis (CNA). In contrary to confined colloidal systems without attractive interactive forces, our systems had shown gelation induced sedimentation. Also, delayed collapse typically evident in sedimentation of bulk systems with attractive interactions was not observed here.

Results from the Brownian dynamics simulations gave a reasonable characterisation of the time-evolution of the experimental system even without hydrodynamic interactions in the simulations. The single major difference is sedimentation appeared to be faster in the simulated system and that networks in the experimental system are coarser with time. Incomplete mixing at the start of the experiment, finite size of the simulations and also some elemental dynamic differences between these two systems (such as the absence of hydrodynamic interactions in the simulations) could be among the contributing factors to the above mentioned differences.

The local structures of gels in the simulations were also considered in this work. Interestingly, there results showed a significant similarity to structural changes observed in quiescent gels. Based on the structural analysis, notable degree of crystallisation is found in system with intermediate $u(r)$. The crystalline order measured by the TCC appeared later in time than the crystalline pre-cursor 142 bonds measured by the CNA. We attribute this to the lower degree of local order in the 142 bonds than the 13 particles clusters (FCC or HCP) determined in the TCC analysis. Similar suppression of crystallisation in gels with stronger $u(r)$ that was observed in chapter 4 is also present in this work. Seemingly, the local structural changes in short time scale is not connected to sedimentation.

7.3 Temperature effects on gelling systems

Building on the idea from simulations where the interaction strengths $u(r)$ of the short-ranged attractive systems can be adjusted in order to attain better self assembly [1, 183] we employed colloid polymer systems suspended in cis decalin for our experiments in this chapter.

Due to the fact that the interactions between colloids in this systems are hard sphere interactions, the response of the system towards temperature is regulated by the polymer. Volume fraction of the polymer ϕ_{PS} determines the $u(r)$ of the attractive interactions in the system where the increasing ϕ_{PS} replicates similar action as quenching the system. This shows that the polymer sets the effective temperature for the system [94]. The R_{g} of the polymer expands when it is in good solvents and shrinks when immersed in theta solvent. Similar behaviour can also be expected when the polymer is above the theta temperature, T^{θ}; the R_{g} increases in size and reduces in size close to T^{θ}. Based on our measurements the T^{θ} is 10°C. We ran several temperature cycling protocol where the effective temperature was dropped close to T^{θ} and kept there for 3 mins then increase the temperature back to the starting room temperature. We repeated this cooling and heating at different time intervals at three temperatures: 11°C, 13 °C and 14 °C. At the end of the experiments, we analysed the bond order parameter ψ_6 to measure crystallinity. For evaluating purposes, we also investigated the structural changes of a sample where temperature cycling protocol was not induced.

The results were not as what we predicted and are contradictory to the results from simulations [1, 183]. The temperature cycling protocol seemed to increase the disordered structures while there was no increase in crystallinity when compared to where there was no temperature cycling protocol. The disordered structures are considered to disrupt the self assembly pathway. Comparing the results from previous chapters 4 and 5, the initial 5-fold symmetry structures are detected in the amorphous systems and the decreasing number of 5-fold symmetry corresponded with the increasing 6-fold symmetry populations. The duration of the experiments were probably too short for the crystallisation to occur in the samples underwent temperature cycling protocol.

The bond order parameter ψ_6 was previously shown to be able to detect crystallinity in 3d systems [117]. However, based on the results in chapter 4, we have demonstrated that some subtle changes might be missed from structural changes based on 2d information of 3d systems. Therefore, a 3d analysis for this work might be required in order to pick up subtle changes in the gels.

7.4 Further work

Extending the depletion attractive mechanism to anisotropic particles could offer novel phase behaviour and route in understanding self assembly of components other than spheres. A noteworthy work in studying the self assembly of aspherical colloids using the depletion mechanism is reported in [99]. Using a monolayer of

indented colloids on a planar wall, the depletion attractive interaction drove the colloids to form plastic crystals in simulations. However, this was not observed in experiments.

Tetrahedra are the simplest polyhedra among the platonic solids. Interestingly, the understanding of their packing properties only seen a rapid development in the last decade [235]. Work from simulations shows that tetrahedra can pack more densely than spheres [236] and random packings were observed when tetrahedra are filled into large container [237]. In other simulation work, high density packing of tetrahedra shaped particles resulted to quasicrystal that can be compressed to a packing fraction ϕ of 85% [53]. In their work, the transition from simple fluid of the tetrahedra was driven by entropy that form a percolating network at the transition and the resulting quasicrystal was the first reported constructed from aspherical particles. It would be interesting to employ the depletion mechanism to the aspherical particles and observed the resulting phases which can be the stepping stones for developing new materials.

Bibliography

[1] D. Klotsa and R. L. Jack, "Controlling crystal self-assembly using a real-time feedback scheme," *J. Chem. Phys.*, vol. 138, p. 094502, 2013.

[2] A. Razali, C. J. Fullerton, F. Turci, J. Hallet, R. L. Jack, and C. P. Royall, "Effects of vertical confinement on gelation and sedimentation of colloids," *Soft Matter*, vol. 13, pp. 3230–3239, 2017.

[3] P. Pusey and W. van Megen, "Phase behaviour of concentrated suspensions of nearly hard colloidal spheres," *Nature*, vol. 320, p. 340, 1986.

[4] D. Frenkel, "Playing tricks with "designer atoms"," *Science*, vol. 296, pp. 65–66, 2002.

[5] M. Minsky, "Microscopy apparatus," *US patent*, p. 3013467, 1957.

[6] V. Prasad, D. Semwogerere, and E. R. Weeks, "Confocal microscopy of colloids," *J. Phys.: Condens. Matter*, vol. 19, p. 113102, 2007.

[7] U. Gasser, E. R. Weeks, A. Schofield, P. N. Pusey, and D. A. Weitz, "Real-space imaging of nucleation and growth in colloidal crystallization," *Science*, vol. 292, pp. 258–262, 2001.

[8] A. Dinsmore and D. Weitz, "Direct imaging of three-dimensional structure and topology of colloidal gels," *J. Phys.: Condens. Matter*, vol. 14, pp. 7581–7597, 2002.

[9] Y. Gao and M. Kilfoil, "Direct imaging of dynamical heterogeneities near the colloid-gel transition," *Phys. Rev. Lett.*, vol. 99, p. 078301, 2007.

[10] A. Malins, S. R. Williams, J. Eggers, and C. P. Royall, "Identification of structure in condensed matter with the topological cluster classification," *J. Chem. Phys.*, vol. 139, p. 234506, 2013.

[11] J. Taffs, A. Malins, S. R. Williams, and C. P. Royall, "The effect of attractions on the local structure of liquids and colloidal fluids," *J. Chem. Phys.*, vol. 133, p. 244901, 2010.

[12] J. Taffs, A. Malins, S. R. Williams, and C. P. Royall, "A structural comparison of models of colloid-polymer mixtures," *J. Phys.: Condens. Matter*, vol. 22, p. 104119, 2010.

[13] G. A. Vliegenthart and H. N. W. Lekkerkerker, "Predicting the gas-liquid critical point from the second virial coefficient," *J. Chem. Phys.*, vol. 112, pp. 5364–5369, 2000.

[14] M. Kilfoil, E. Pashkovski, J. Masters, and D. A. Weitz, "Dynamics of weakly aggregated colloidal particles," *Philosophical Transactions: Mathematical, Physical and Engineering Sciences*, vol. 361, no. 1805, pp. 753–766, 2003.

[15] S. Asakura and F. Oosawa, "On interaction between 2 bodies immersed in a solution of macromolecules," *J. Chem. Phys.*, vol. 22, no. 7, pp. 1255–1256, 1954.

[16] S. Asakura and F. Oosawa, "Interaction between particles suspended in solutions of macromolecules," *J. Poly. Sci.*, vol. 33, pp. 183–192, 1958.

[17] A. Vrij, "Polymers at interfaces and interactions in colloidal dispersions," *Pure Appl. Chem.*, vol. 48, no. 4, pp. 471–483, 1976.

[18] S. M. Ilett, A. Orrock, W. C. K. Poon, and P. N. Pusey, "Phase behaviour of a model colloid-polymer mixture," *Phys. Rev. E.*, vol. 52, pp. 1344–1352, 1995.

[19] W. C. K. Poon, J. S. Selfe, M. B. Robertson, S. M. Ilett, A. D. Pirie, and P. N. Pusey, "An experimental study of a model colloid-polymer mixture," *J. Phys. II (France)*, vol. 3, no. 7, pp. 1075–1086, 1993.

[20] J. Bergenholtz, P. W. C. K., and M. Fuchs, "Gelation in model colloid-polymer mixtures," *Lan*, vol. 19, pp. 4493–4503, 2003.

[21] W. C. K. Poon, A. D. Pirie, and P. N. Pusey, "Gelation in colloid-polymer mixtures," *Faraday Discuss*, vol. 101, pp. 65 – 76, 1995.

[22] N. A. M. Verhaegh, D. Asnaghi, H. N. W. Lekkerkerker, M. Giglio, and L. Cipelletti, "Transient gelation by spinodal decomposition in colloid-polymer mixtures," *Physica A*, vol. 242, pp. 104–118, 1997.

[23] V. Prasad, V. Trappe, A. D. Dinsmore, P. N. Segre, C. L., and W. D. A., "Universal features of the fluid to solid transition for attractive colloidal particles," *Faraday Discuss.*, vol. 123, pp. 1–12, 2003.

[24] P. Bartlett, L. J. Teece, and M. A. Faers, "Sudden collapse of a colloidal gel," *Phys Rev E.*, vol. 85, no. 2, p. 021404, 2012.

[25] P. R. Ten Wolde, M. J. Ruizmontero, and D. Frenkel, "Numerical evidence for bcc ordering at the surface of a critical fcc nucleus," *Phys. Rev. Lett.*, vol. 75, pp. 2714–2717, Oct. 1995.

[26] D. Rosenbaum, P. Zamora, and C. F. Zukoski, "Phase behaviour of small attractive colloidal particles," *Phys Rev. Lett.*, vol. 76, no. 1, pp. 150–153, 1996.

[27] R. P. Sear, "Nucleation: theory and applications to protein solutions and colloidal suspensions," *J. Phys.: Condens. Matter*, vol. 19, p. 033101, 2007.

[28] S. Manley, J. M. Skotheim, L. Mahadevan, and D. A. Weitz, "Gravitational collapse of colloidal gels," *Phys Rev Lett*, vol. 94, no. 21, p. 218302, 2005.

[29] R. MacBean, *Packaging and the Shelf Life of Yogurt*, pp. 143–156. CRC Press, 2016/12/17 2009.

[30] M. Rubinstein and A. Dobrynin, "Associations leading to formation of reversible networks and gels," *Current Opinion in Colloid and Interface Science*, vol. 4, pp. 83–87, 1999.

[31] W. Russel, D. Saville, and W. Schowalter, *Colloidal Dispersions*. Cambridge Univ. Press, Cambridge, 1989.

[32] W. C. K. Poon, "The physics of a model colloid-polymer mixture," *J. Phys.: Condens. Matter*, vol. 14, pp. R859–R880, Aug. 2002.

[33] H. N. W. Lekkerkerker, W. C. K. Poon, P. N. Pusey, A. Stroobants, and P. B. Warren, "Phase-behavior of colloid plus polymer mixtures," *Europhys. Lett.*, vol. 20, pp. 559–564, Nov. 1992.

[34] K. N. Pham, A. M. Puertas, J. Bergenholtz, S. Egelhaaf, A. Moussaïd, P. N. Pusey, A. B. Schofield, M. E. Cates, and P. W. C. K., "Multiple glassy states in a simple model system," *Science*, vol. 296, pp. 104–106, 2002.

[35] A. P. Gast, C. K. Hall, and W. B. Russel, "Polymer-induced phase separations in nonaqueous colloidal suspensions," *J. Coll. Interf. Sci.*, vol. 96, pp. 251–267, 1983.

[36] S. C. Glotzer and M. J. Solomon, "Anisotropy of building blocks and their assembly into complex structures," *Nature Materials*, vol. 6, pp. 557–562, 2007.

[37] D. C. Rapaport, "Role of reversibility in viral capsid growth: A paradigm for self-assembly," *Phys. Rev. Lett.*, vol. 101, p. 186101, 2008.

[38] M. E. Leunissen, C. G. Christova, A.-P. Hyninnen, C. P. Royall, A. I. Campbell, A. Imhof, M. Dijkstra, R. van Roij, and A. van Blaaderen, "Ionic colloidal crystals of oppositely charged particles," *Nature*, vol. 437, pp. 235–240, 2005.

[39] D. Klotsa and R. L. Jack, "Predicting the self-assembly of a model colloidal crystal," *Soft Matter*, vol. 7, pp. 6294–6303, 2011.

[40] A.-P. Hynninen, J. Thijssen, E. Vermolen, M. Dijkstra, and A. van Blaaderen, "Self-assembly route for photonic crystals with a bandgap in the visible region," *Nature Mater.*, vol. 6, pp. 202–205, 2007.

[41] Y. Wang, Y. Wang, D. R. Breed, V. N. Manoharan, L. Feng, A. D. Hollingsworth, M. Weck, and D. J. Pine, "Colloids with valence and specific directional bonding," *Nature*, vol. 491, pp. 51–56, 2012.

[42] G. M. Whitesides and D. Lipomi, "Soft nanotechnology: "structure" vs. "function"," *Faraday Discuss.*, vol. 143, pp. 373–384, 2009.

[43] R. Langer and D. Tirrell, "Designing materials for biology and medicin," *Nature*, vol. 428, p. 487, 4 2004.

[44] S. Stupp, "Self-assembly and biomaterials," *NanoLett.*, vol. 10, pp. 4783–4786, 2010.

[45] L. Hong, A. Cacciuto, E. Luijten, and S. Granick, "Clusters of charged janus spheres," *NanoLett.*, vol. 6, pp. 2510–2514, 2006.

[46] S. Jiang, C. Qian, M. Tripathy, E. Luitjen, K. S. Schweizer, and S. Granick, "Janus particle synthesis and assembly," *Adv. Mater.*, vol. 22, pp. 1060–1071, 2010.

[47] S. Sacanna, M. Korpics, K. Rodriguez, L. Colon-Melendez, S. Kim, D. J. Pine, and G. Yi, "Shaping colloids for self-assembly," *Nature Comm.*, vol. 4, no. 1688, 2013.

[48] D. Nykypanchuk, M. M. Maye, D. van der Lelie, and O. Gang, "Dna-guided crystallisation of colloidal nanoparticles," *Nature*, vol. 451, pp. 549–552, 2008.

[49] C. Chen, O. Cook, C. E. Nicholson, and S. J. Cooper, "Leapfrogging ostwald's rule of stages: Crystallization of stable g-glycine directly from microemulsions," *Crystal Growth and Design*, vol. 11, pp. 2228–2237, 2011.

[50] A. B. Pawar and I. Kretzschmar, "Fabrication, assembly, and application of patchy particles," *Macromol. Rapid Commun.*, vol. 31, pp. 150–168, 2010.

[51] F. Romano and F. Sciortino, "Colloidal self-assembly: Patchy from the bottom up," *Nature Materials*, vol. 10, pp. 171–173, 2011.

[52] A. W. Wilber, J. P. K. Doye, A. A. Louis, and A. C. F. Lewis, "Monodisperse self-assembly in a model with protein-like interactions," *J. Chem. Phys.*, vol. 131, p. 175102, 2009.

[53] A. Haji-Akbari, M. Engel, A. S. Keys, X. Zheng, R. Petschek, P. Palffy-Muhoray, and S. C. Glotzer, "Disordered, quasicrystalline and crystalline phases of densely packed tetrahedra," *Nature*, vol. 462, pp. 773–777, 2009.

[54] F. J. Martinez-Veracoechea, B. M. Mladek, A. Tkachenko, and F. D., "Design rule for colloidal crystals of dna-functionalized particles," *Phys Rev Lett.*, vol. 107, no. 045902, 2011.

[55] E. Jankowski and S. C. Glotzer, "Screening and designing patchy particles for optimized self-assembly propensity through assembly pathway engineering," *Soft Matter*, vol. 8, p. 2852, 2012.

[56] A. J. Bray, "Theory of phase-ordering kinetics," *Advances in Physics*, vol. 43, no. 3, pp. 357–459, 1994.

[57] P. J. Lu, J. C. Conrad, H. M. Wyss, A. B. Schofield, and D. A. Weitz, "Fluids of clusters in attractive colloids," *Phys. Rev. Lett.*, vol. 96, Jan. 2006.

[58] S. Whitelam and R. L. Jack, "The statistical mechanics of dynamic pathways to self-assembly," *Annu. Rev. Phys. Chem.*, vol. 66, pp. 143–63, 2015.

[59] E. Zaccarelli, "Colloidal gels: equilibrium and non-equilibrium routes," *J Phys.: Condens Matter*, vol. 19, no. 32, 2007.

[60] J. Perrin, *Les Atomes.*
Felix Alcan, 1913.

[61] A. Einstein, *Investigations on the Theory of the Brownian Movement.*
Dover, New York, 1926.

[62] D. Levesque, J.-P. Hansen, and J. Zinn-Justin, eds., *Liquids, Freezing and Glass Transition*, vol. Les Houches Session L1.
Elsevier, Amsterdam, 1991.

[63] P. Lidner and T. Zemb, eds., *Neutron, X-rays and Light. Scattering Methods Applied to Soft Condensed Matter*.
Elsevier, Amsterdam, 1st ed., 2002.

[64] V. Trappe, V. Prasad, P. Cipelletti, L. Segre, and D. Weitz, "Jamming phase diagram for attractive particles," *Nature*, vol. 411, pp. 772–775, 2001.

[65] V. Carrier and G. Petekidis, "Nonlinear rheology of colloidal glasses of soft thermosensitive microgel particles," *J. Rheol.*, vol. 53, pp. 245–274, 2009.

[66] A. Nicolas and J. L. Barrat, "A mesoscopic model for the rheology of soft amorphous solids, with application to microchannel flows," *Faraday Discuss.*, vol. 167, pp. 567–600, 2013.

[67] N. Koumakis, A. Panvouxoglou, A. S. Poulos, and G. Petekidis, "Direct comparison of the rheology of model hard and soft particle glasses," *Soft Matter*, vol. 8, pp. 4272–4284, 2012.

[68] P. Habdas and E. R. Weeks, "Video microscopy of colloidal suspensions and colloidal crystals," *Current Opinion in Colloid and Interface Science*, vol. 7, pp. 196–203, 2002.

[69] J. Zhu, R. Rogers, W. Meyer, R. H. Ottewill, W. B. Russel, and P. Chaikin, "Crystallization of hard-sphere colloids in microgravity," *Nature*, vol. 387, pp. 883–885, 1997.

[70] Z. Cheng, J. Zhu, W. B. Russel, W. Meyer, and P. M. Chaikin, "Colloidal hard-sphere crystallization kinetics in microgravity and normal gravity," *Appl. Opt.*, vol. 40, no. 24, pp. 4146–4151, 2001.

[71] R. C. P., R. van Roij, and A. van Blaaderen, "Extended sedimentation profiles in charged colloids: the gravitational length, entropy, and electrostatics," *J Phys.: Condens Matter*, vol. 17, pp. 2315–2326, 2005.

[72] N. Simeonova and W. K. Kegel, "Gravity-induced aging in glasses of colloidal hard spheres," *Phys Rev Lett*, vol. 93, no. 3, 2004.

[73] A. Ivlev, H. Loewen, G. E. Morfill, and C. P. Royall, *Complex Plasmas and Colloidal Dispersions: Particle-resolved Studies of Classical Liquids and Solids*.
World Scientific Publishing Co., Singapore Scientific, 2012.

[74] P. N. Pusey, W. van Megen, P. Bartlett, B. J. Ackerson, J. G. Rarity, and S. M. Underwood, "Structure of crystals of hard colloidal spheres," *Phys Rev. Lett.*, vol. 63, no. 25, 1989.

[75] A. van Blaaderen and P. Wiltzius, "Real-space structure of colloidal hard-sphere glasses," *Science*, vol. 270, pp. 1177–1179, 1995.

[76] P. C. Hiemenz and R. Rajagopalan, *Principles of Colloid and Surface Chemistry*. CRC Press, 3rd ed., 1997.

[77] J. Israelachvili, *Intermolecular and Surface Forces*. Elsevier Publishing Company, Amsterdam, 2nd ed., 1991.

[78] B. Alder and T. Wainwright, "Phase transition for a hard sphere system," *J. Phys. Chem.*, vol. 27, pp. 1208–1209, 1957.

[79] W. G. Hoover and F. Ree, "Melting transition and communal entropy for hard spheres," *J. Chem. Phys.*, vol. 49, pp. 3609–3617, 1968.

[80] N. J. A. Sloane, "Kepler's conjecture confirmed," *Nature*, vol. 395, pp. 435–436, October 1998.

[81] T. C. Hales, "Sphere packings 1," *Discrete Computational Geom.*, vol. 17, pp. 1–51, 1997.

[82] T. C. Hales, "Sphere packings 2," *Discrete Computational Geom.*, vol. 18, pp. 135–149, 1997.

[83] T. C. Hales, "Sphere packings, iv. detailed bounds," *Discrete Comput. Geom.*, vol. 36, pp. 111–166, 2006.

[84] G. Brambilla, D. El Masri, M. Pierno, L. Berthier, L. Cipelletti, G. Petekidis, and A. B. Schofield, "Probing the equilibrium dynamics of colloidal hard spheres above the mode-coupling glass transition," *Phys. Rev. Lett.*, vol. 102, p. 085703, 2009.

[85] F. H. Stillinger and P. G. Debenedetti, "Glass transition thermodynamics and kinetics," *Annu. Rev. Condens. Matter Phys.*, vol. 4, pp. 263–285, 2013.

[86] R. C. P., A. Malins, A. J. Dunleavy, and R. Pinney, "Strong geometric frustration in model glassformers," *J. Non-Cryst. Solids*, vol. 407, pp. 34–43, 2015.

[87] C. A. Angell, "Formation of glasses from liquids and biopolymers," *Science*, vol. 267, pp. 1924–1935, 1995.

[88] L. Antl, J. W. Goodwin, R. D. Hill, R. H. Ottewill, S. M. Owens, S. Papworth, and J. A. Waters, "The preparation of poly(methyl methacrylate) lattices in nonaqueous media," *Colloids and surfaces*, vol. 17, pp. 67–78, 1986.

[89] A. I. Campbell and P. Bartlett, "Fluorescent hard-sphere colloids for confocal microscopy.," *J. Coll. Interf. Sci.*, vol. 256, pp. 325–330, 2002.

[90] B. Vincent, P. A. Luckham, and F. Waite, "The effect of free polymer on the stability of sterically stabilized dispersions," *J. Coll. Interf. Sci*, vol. 73, pp. 508–521, 1980.

[91] D. G. A. L. Aarts, R. Tuinier, and H. N. W. Lekerkerker, "Phase behaviour of mixtures of colloidal spheres and excluded-volume polymer chains," *J. Phys.: Condens. Matter*, vol. 14, pp. 7551–7561, 2002.

[92] G. Fleer and R. Tuinier, "Analytical phase diagrams for colloids and nonadsorbing polymer," *Adv. Coll. Interf. Sci.*, vol. 143, pp. 1–47, 2008.

[93] H. N. W. Lekkerkerker and R. Tuinier, *Colloids and the Depletion Interaction*, vol. 833 of *Lecture Notes in Physics*.
Berlin: Springer, 2011.

[94] C. P. Royall, A. A. Louis, and H. Tanaka, "Measuring colloidal interactions with confocal microscopy," *J. Chem. Phys.*, vol. 127, no. 4, p. 044507, 2007.

[95] S. Taylor, R. Evans, and C. P. Royall, "Temperature as an external field for colloid-polymer mixtures: "quenching" by heating and "melting" by cooling," *J. Phys.: Condens. Matter*, vol. 24, p. 464128, 2012.

[96] G. M. Whitesides and M. Boncheva, "Beyond molecules: Self-assembly of mesoscopic and macroscopic components," *Proc. Nat. Acad. Sci.*, vol. 99, pp. 4769–4774, 2002.

[97] D. J. Kraft, J. Groenewold, and W. K. Kegel, "Colloidal molecules with well-controlled bond angles," *Soft Matter*, vol. 5, pp. 3823–3826, 2009.

[98] Q. Chen, J. K. Whitmer, S. Jiang, S. C. Bae, E. Luijten, and S. Granick, "Supracolloidal reaction kinetics of janus spheres," *Science*, vol. 199-202, p. 331, 2011.

[99] D. Ashton, S. Ivell, R. P. A. Dullens, R. L. Jack, N. B. Wilding, and D. G. A. L. Aarts, "Self assembly and crystallisation of indented colloids at a planar wall," *Soft Matter*, vol. 11, pp. 6089–6098, 2015.

[100] G. M. Whitesides, "The once and future nanomachine," *Sci. Am.*, vol. 285, no. 3, pp. 78–83, 2001.

[101] Y. Xia, B. Gates, Y. Yin, and Y. Lu, "Monodispersed colloidal spheres: Old materials with new applications," *Adv. Mater.*, vol. 12, pp. 693–713, 2000.

[102] Y. Vlasov, X. Bo, J. Sturm, and D. Norris, "On-chip natural assembly of silicon photonic bandgap," *Nature*, vol. 414, pp. 289–293, November 2001.

[103] J. Joannopoulos, "Photonics: Self assembly lights up," *Nature*, vol. 414, pp. 257–258, November 2001.

[104] R. L. Jack, M. F. Hagan, and D. Chandler, "Fluctuation-dissipation ratios in the dynamics of self-assembly," *Phys. Rev. E.*, vol. 76, p. 021119, 2007.

[105] S. Whitelam, E. Feng, M. F. Hagan, and P. Geissler, "The role of collective motion in examples of coarsening and self-assembly," *Soft Matter*, vol. 5, pp. 1251–1262, 2009.

[106] S. Auer and D. Frenkel, "Prediction of absolute crystal nucleation rate in hard-sphere colloids," *Nature*, vol. 409, pp. 1020–1023, 2001.

[107] J. S. van Duijneveldt and F. D., "Computer simulation study of free energy barriers in crystal nucleation," *J. Chem. Phys*, vol. 96, pp. 4655–4668, 1992.

[108] S. Auer and D. Frenkel, "Quantitative prediction of crystal-nucleation rates for spherical colloids: A computational approach," *Annu. Rev. Phys. Chem.*, vol. 55, pp. 333–61, 2004.

[109] D. W. Oxtoby, "Nucleation of first-order phase transitions," *Acc. Chem. Res.*, vol. 31, pp. 91–97, 1998.

[110] P. G. Debenedetti, *Metastable Liquids Concepts and Principles*. Princeton: Princeton University Press, 1996.

[111] R. P. Sear, "On the interpretation of quantitative experimental data on nucleation rates using classical nucleation theory," *J. Phys. Chem. B.*, vol. 110, pp. 21944–21949, 2006.

[112] M. Dijkstra, J. M. Brader, and R. Evans, "Phase behaviour and structure of model colloid-polymer mixtures," *J. Phys.: Condens. Matter*, vol. 11, pp. 10079–10106, 1999.

[113] M. Dijkstra, R. van Roij, and R. Evans, "Effective interactions, structure, and isothermal compressibility of colloidal suspensions," *J. Chem. Phys*, vol. 113, pp. 4799–4807, 2000.

[114] E. K. Hobbie, "Metastability and depletion-driven aggregation," *Phys. Rev. Lett.*, vol. 89, pp. 3996–4001, 1998.

[115] C. Allain and M. Wafra, "Aggregation and sedimentation in colloidal suspensions," *Phys. Rev. Lett.*, vol. 74, pp. 1478–1481, 1995.

[116] L. Cipelletti, S. Manley, R. C. Ball, and D. A. Weitz, "Universal aging features in the restructuring of fractal colloidal gels," *Phys Rev Lett*, vol. 84, no. 10, pp. 2275 LP – 2278, 2000.

[117] C. Royall, S. Williams, T. Ohtsuka, and H. Tanaka, "Direct observation of a local structural mechanism for dynamic arrest," *Nature Materials*, vol. 7, p. 556, 2008.

[118] S. Griffiths, F. Turci, and C. P. Royall, "Local structure of percolating gels at very low volume fractions," *accepted by J. Chem. Phys.*, vol. 146, 2017.

[119] L. Starrs, W. C. K. Poon, D. J. Hibberd, and M. M. Robins, "Collapse of transient gels in colloid-polymer mixtures," *J Phys.: Condens Matter*, vol. 14, no. 10, p. 2485, 2002.

[120] S. Buzzaccaro, E. Secchi, G. Brambilla, R. Piazza, and C. L., "Equilibrium concentration profiles and sedimentation kinetics of colloidal gels under gravitational stress," *J Phys.: Condens Matter*, vol. 24, no. 28, p. 284103, 2012.

[121] M. D. Haw, M. Sievwright, W. C. K. Poon, and P. N. Pusey, "Cluster-cluster gelation with finite bond energy," *Adv Colloid Interface Sci*, vol. 62, no. 1, pp. 1–16, 1995.

[122] R. P. Sear, "Phase behavior of a simple model of globular proteins," *J. Chem. Phys.*, vol. 111, pp. 4800–4806, 1999.

[123] M. G. Noro and D. Frenkel, "Extended corresponding-states behavior for particles with variable range attractions," *J. Chem. Phys.*, vol. 113, pp. 2941–2944, 2000.

[124] M. Ediger, "Spatially heterogeneous dynamics in supercooled liquids," *Annu. Rev. Phys. Chem.*, vol. 51, pp. 99–128, 2000.

[125] E. R. Weeks, J. C. Crocker, A. C. Levitt, and W. D. A., "Three-dimensional direct imaging of structural relaxation near the colloidal glass transition," *Science*, vol. 287, pp. 627–631, 2000.

[126] F. Sciortino, "Disordered materials: One liquid, two glasses," *Nature Materials*, vol. 1, pp. 145 – 146, 2002.

[127] G. Foffi, C. D. Michele, F. Sciortino, and P. Tartaglia, "Scaling of dynamics with the range of interaction in short-range attractive colloids," *Phys. Rev. Lett.*, vol. 94, p. 078301, Feb 2005.

[128] C. L. Klix, C. P. Royall, and H. Tanaka, "Structural and dynamical features of multiple metastable glassy states in a colloidal system with competing interactions," *Phys. Rev. Lett.*, vol. 104, p. 165702, 2010.

[129] T. van de Laar, R. Higler, K. Schroën, and J. Sprakel, "Discontinuous nature of the repulsive-to-attractive colloidal glass transition," *Scientific Reports*, vol. 6, pp. 22725 EP –, 03 2016.

[130] D. R. Nelson, *Defects and Geometry in Condensed Matter Physics*. Cambridge University Press, 2002.

[131] P. J. Steinhardt, D. R. Nelson, and M. Ronchetti, "Bond-orientational order in liquids and glasses," *Phys. Rev. B*, vol. 28, no. 2, pp. 784–805, 1983.

[132] V. de Villeneuve, R. P. A. Dullens, D. Aarts, E. Groeneveld, J. Scherff, W. K. Kegel, and H. Lekkerkerker, "Colloidal hard-sphere crystal growth frustrated by large spherical impurities," *Science*, vol. 309, pp. 1231–1233, 2005.

[133] R. P. A. Dullens, D. G. A. L. Aarts, and W. K. Kegel, "Dynamic broadening of the crystal-fluid interface of colloidal hard spheres," *Phys. Rev. Lett.*, vol. 97, p. 228301, 2006.

[134] P. Schall, I. Cohen, W. D. A., and F. Spaepen, "Visualization of dislocation dynamics in colloidal crystals," *Science*, pp. 1944–1948, Sept 2004 2004.

[135] P. Schall, I. Cohen, W. D. A., and F. Spaepen, "Visualizing dislocation nucleation by indenting colloidal crystals," *Nature*, vol. 440, pp. 319–323, 2006.

[136] K. Lin, J. C. Crocker, V. Prasad, A. Schofield, W. D. A., T. Lubensky, and A. G. Yodh, "Entropically driven colloidal crystallization on patterned surfaces," *Phys Rev. Lett.*, vol. 85, no. 8, pp. 1770–1773, 2000.

[137] C. P. Royall, J. Dzubiella, M. Schmidt, and A. van Blaaderen, "Nonequilibrium sedimentation of colloids on the particle scale," *Phys. Rev. Lett.*, vol. 98, p. 188304, 2007.

[138] M. Schmidt, M. Dijkstra, and J. Hansen, "Competition between sedimentation and phase coexistence of colloidal dispersions under gravity," *J. Phys.: Condens. Matter*, vol. 16, pp. S4185–S4194, 2004.

[139] R. Piazza, T. Bellini, and V. Degiorgio, "Equilibrium sedimentation profiles of screened charged colloids: A test of the hard sphere equation ofstate," *Phys. Rev. Lett.*, vol. 25, pp. 4267–4270, 1993.

[140] R. Piazza, "Settled and unsettled issues in particle settling," *Rep. Prog. Phys.*, vol. 77, no. 5, p. 056602, 2014.

[141] A. Moncho Jorda, A. A. Louis, and J. T. Padding, "Effects of inter-particle attractions on colloidal sedimentation," *Phys Rev Lett*, vol. 104, p. 068301, 2010.

[142] V. Gopalakrishnan, K. S. Schweizer, and C. F. Zukoski, "Linking single particle rearrangements to delayed collapse times in transient depletion gels," *J. Phys. Condens. Matt.*, vol. 18, pp. 11531–11550, 2006.

[143] C. Derec, D. Senis, L. Talini, and C. Allain, "Rapid settling of a colloidal gel," *Phys Rev E*, vol. 67, 2003.

[144] A. S. Michaels and J. C. Bolger, "Settling rates and sediment volumes of flocculated kaolin suspensions," *Industrial & Engineering Chemistry Fundamentals*, vol. 1, pp. 24–33, 1962.

[145] R. M. L. Evans and L. Starrs, "Emergence of a stress transmission length-scale in transient gels," *J Phys.: Condens Matter*, vol. 14, no. 10, p. 2507, 2002.

[146] R. Buscall and L. White, "The consolidation of concentrated suspensions," *J. Chem. Soc., Faraday Trans. 1*, vol. 83, pp. 873–891, 1987.

[147] J. J. Lietor-Santos, C. Kim, P. J. Lu, A. Fernandez-Nieves, and W. D. A., "Gravitational compression of colloidal gels," *Eur. Phys. J. E*, vol. 28, pp. 159–164, 2009.

[148] P. Pusey, A. Pirie, and W. Poon, "Dynamics of colloid-polymer mixtures," *Physica A: Statistical Mechanics and its Applications*, vol. 201, no. 1-3, pp. 322–331, 1993.

[149] P. Pusey and W. van Megen, "Observation of a glass transition in suspensions of spherical colloidal particles," *Physical Review Letters*, vol. 59, no. 18, pp. 2083–2086, 1987.

[150] I. Zhang, C. P. Royall, M. A. Faers, and P. Bartlett, "Phase separation dynamics in colloid-polymer mixtures: the effect of interaction range," *Soft Matter*, vol. 9, pp. 2076–2084, 2013.

[151] G. Berry, "Thermodynamic and conformational properties of polystyrene. i. light-scattering studies on dilute solutions of linear polystyrenes," *J. Chem. Phys.*, vol. 44, pp. 4550–4564, 1966.

[152] S. Torquato, T. M. Truskett, and P. G. Debenedetti, "Is random close packing of spheres well defined?," *Phys. Rev. Lett.*, vol. 84, pp. 2064–2067, Mar. 2000.

[153] A. van Blaaderen and P. Wiltzius, "Real-space structure of colloidal hard-sphere glasses," *Science*, vol. 270, pp. 1177–1179, Nov. 1995.

[154] W. C. K. Poon, E. R. Weeks, and C. P. Royall, "On measuring colloidal volume fractions," *Soft Matter*, vol. 8, pp. 21–30, 2012.

[155] C. J. R. Sheppard and D. M. Shotton, *Confocal laser scannig microscopy*. BIOS Scientific Publishers, Oxford, England., 1997.

[156] T. Corle and G. Kino, *Confocal scanning optical microscopy and related imaging systems*. Academic Press, 1996.

[157] J. Pawley, *Handbook of Biological Confocal Microscopy*. Springer, New York., 2006.

[158] S. Inoue and K. Spring, *Video Microscopy the Fundamentals*, ch. Microscope image formation. Plenum Press: New York, 1997.

[159] D. Semwogerere and E. R. Weeks, *Encyclopedia of Biomaterials and Biomedical Engineering*, ch. Confocal microscopy. Taylor & Francis, 2005.

[160] O. Johari and A. Samudra, *Characterization of Solid Surfaces*, ch. 5: Scanning electron microscopy, pp. 107–131. Springer, US, 1974.

[161] M. C. Jenkins and S. U. Egelhaaf, "Confocal microscopy of colloidal particles: Towards reliable, optimum coordinates," *J. Coll. Interf. Sci.*, vol. 136, pp. 65–92, 2008.

[162] J. C. Crocker and D. G. Grier, "Methods of digital video microscopy for colloidal studies," *J. Coll. Interf. Sci.*, vol. 179, pp. 298–310, 1995.

[163] P. J. Lu, P. A. Sims, H. Oki, J. B. Macarthur, and D. A. Weitz, "Target-locking acquisition with real-time confocal (tarc) microscopy," *Optics Express*, vol. 15, pp. 8702–8712, 2007.

[164] "http://lammps.sandia.gov."

[165] J.-P. Hansen and I. Macdonald, *Theory of Simple Liquids*. Academic, London, 1976.

[166] A. Thorneywork, R. Roth, D. G. A. L. Aarts, and R. P. A. Dullens, "Communication: Radial distribution functions in two-dimensional binary colloidal hard sphere system," *J. Chem. Phys.*, vol. 140, p. 161106, 2014.

[167] F. C. Frank, "Supercooling of liquids," *Proc. R. Soc. Lond. A.*, vol. 215, no. 1120, pp. 43–46, 1952.

[168] S. Mossa and G. Tarjus, "Locally preferred structure in simple atomic liquids," *J. Chem. Phys.*, vol. 119, pp. 8069–8074, 2003.

[169] J. P. K. Doye, D. J. Wales, and R. S. Berry, "The effect of the range of the potential on the structures of clusters," *J. Chem. Phys.*, vol. 103, pp. 4234–4249, Sept. 1995.

[170] D. S. Franzblau, "Computation of ring statistics for network models of solids," *Phys. Rev. B*, vol. 44, pp. 4925–4930, Sept. 1991.

[171] S. R. Williams, "Topological Classification of Clusters in Condensed Phases," *ArXiV:0705.0203*, May 2007.

[172] A. Malins, *A Structural Approach to Glassy Systems*. PhD thesis, University of Bristol, 2013.

[173] P. J. Lu, E. Zaccarelli, F. Ciulla, A. B. Schofield, F. Sciortino, and D. A. Weitz, "Gelation of particles with short-range attraction," *Nature*, vol. 435, pp. 499–504, 2008.

[174] J. D. Honeycutt and H. C. Andersen, "Molecular dynamics study of melting and freezing of small lennard-jones clusters," *J. Phys. Chem.*, vol. 91, pp. 4950–4963, 1987.

[175] P. J. Steinhardt, D. R. Nelson, and M. Ronchetti, "Icosahedral bond orientational order in supercooled liquids," *Phys. Rev. Lett.*, vol. 47, pp. 1297–1300, Nov 1981.

[176] M. Heni and H. Lowen, "Do liquids exhibit local fivefold symmetry at interfaces?," *Phys. Rev. E*, vol. 65, p. 021501, 2002.

[177] C. Chakravarty, "Bond orientational order in atomic cluster," *Molecular Physics*, vol. 100, pp. 3777–3780, 2002.

[178] T. Palberg, "Crystallisation kinetics of colloidal model suspensions: recent acheivements and new perspectives," *J. Phys. Condens. Matt.*, vol. 26, p. 333101, 2014.

[179] E. H. A. de Hoog, W. K. Kegel, A. van Blaaderen, and H. N. W. Lekkerkerker, "Direct observation of crystalisation and aggregation in a phase-separating colloid-polymer suspension.," *Phys. Rev. E.*, vol. 64, p. 021407, 2001.

[180] C. P. Royall and A. Malins, "The role of quench rate in colloidal gels," *Faraday Discuss.*, vol. 158, pp. 301–311, 2012.

[181] F. Zhang, R. Roth, M. Wolf, F. Roosen-Runge, M. W. A. Skoda, R. M. J. Jacobs, M. Stzuckie, and F. Schreiber, "Charge-controlled metastable liquid-liquid phase separation in protein solutions as a universal pathway towards crystallization," *Soft Matter*, vol. 8, p. 1313, 2012.

[182] J. Taffs, S. R. Williams, H. Tanaka, and C. P. Royall, "Structure and kinetics in the freezing of nearly hard spheres," *Soft Matter*, vol. 9, pp. 297–305, 2013.

[183] C. J. Fullerton and R. L. Jack, "Optimising self-assembly through time-dependent interactions," *J. Chem. Phys.*, vol. 145, no. 24, p. 244505, 2016.

[184] L. Cipelletti and L. Ramos, "Slow dynamics in glassy soft matter," *Journal of Physics: Condensed Matter*, vol. 17, no. 6, pp. R253–R285, 2005.

[185] H. Tanaka, "Two-order-parameter description of liquids. 1. a general model of glass transition covering its strong to fragile limit," *J. Chem. Phys.*, vol. 111, pp. 3163–3174, Aug. 1999.

[186] E. Zaccarelli, P. J. Lu, F. Ciulla, D. A. Weitz, and F. Sciortino, "Gelation as arrested phase separation in short-ranged attractive colloid-polymer mixtures," *J Phys.: Condens Matter*, vol. 20, no. 49, p. 494242, 2008.

[187] B. Ruzicka, E. Zaccarelli, L. Zulian, R. Angelini, M. Sztucki, A. Moussaid, T. Narayanan, and F. Sciortino, "Observation of empty liquids and equilibrium gels in a colloidal clay," *Nature Materials*, vol. 10, pp. 56–60, 2010.

[188] H. Tanaka, "Importance of many-body orientational correlations in the physical description of liquids," *Faraday Discuss*, vol. 167, pp. 9–76, 2013.

[189] A. Fortini, E. Sanz, and M. Dijkstra, "Crystallization and gelation in colloidal systems with short-ranged attractive interactions," *Phys. Rev. E*, vol. 78, p. 041402, 2008.

[190] C. P. Royall and S. R. Williams, "The role of local structure in dynamical arrest," *Phys. Rep.*, vol. 560, p. 1, 2015.

[191] C. P. Royall, S. R. Williams, T. Ohtsuka, and T. H., "Direct observation low-energy clusters in a colloidal gels," *American Institute of Physics Conference Proceedings*, vol. 982, p. 97, 2008.

[192] C. P. Royall, S. R. Williams, and H. Tanaka, "The nature of the glass and gel transitions in sticky spheres," *ArXiV*, p. 1409.5469, 2014.

[193] J. A. Long, D. W. J. Osmond, and B. Vincent, "The equlibrium aspect of weak flocculation," *Journal of Colloid and Interface Science*, vol. 42, no. 3, pp. 545–553, 1973.

[194] M. Leocmach, J. Russo, and T. H., "Importance of many-body correlations in glass transition: An example from polydispere hard spheres," *J. Chem. Phys.*, vol. 138, p. 12A515, 2013.

[195] F. Lo Verso, R. L. C. Vink, D. Pini, and L. Reatto, "Critical behavior in colloid-polymer mixtures: Theory and simulation," *Phys. Rev. E*, vol. 73, p. 061407, 2006.

[196] C. P. Royall, D. G. A. L. Aarts, and H. Tanaka, "Bridging length scales in colloidal liquids and interfaces from near-critical divergence to single particles," *Nature Physics*, vol. 3, pp. 636–640, 2007.

[197] R. C. P., D. G. A. L. Aarts, and H. Tanaka, "Fluid structure in colloid-polymer mixtures: the competition between electrostatics and depletion," *J. Phys. Condens. Matt.*, vol. 17, no. 45, 2005.

[198] T. M. Truskett, S. Torquato, S. Sastry, P. G. Debenedetti, and F. H. Stillinger, "Structural precursor to freezing in the hard-disk and hard-sphere systems," *Phys. Rev. E*, vol. 58, pp. 3083–3088, Sept. 1998.

[199] U. Gasser, A. Schofield, and D. Weitz, "Local order in a supercooled colloidal fluid observed by confocal microscopy," *J. Phys.: Condens. Matter*, vol. 15, pp. S375–S380, 2003.

[200] N. C. Karayiannis, R. Malshe, J. J. de Pablo, and M. Laso, "Fivefold symmetry as an inhibitor to hard-sphere crystallization," *Phys. Rev. E*, vol. 83, p. 061505, Jun 2011.

[201] N. Karayiannis, R. Malshe, M. Kröger, J. J. de Pablo, and M. Laso, "Evolution of fivefold local symmetry during crystal nucleation and growth in dense hard-sphere packings," *Soft Matter*, vol. 8, no. 3, pp. 844–858, 2012.

[202] A. I. Campbell, V. Anderson, J. S. van Duijneveldt, and P. Bartlett, "Dynamical arrest in attractive colloids: The effect of long-range repulsion," *Phy. Rev. Lett.*, vol. 94, no. 208301, 2005.

[203] C. P. Royall and S. R. Williams, "C60: the first one-component gel?," *J. Phys. Chem. B*, vol. 115, pp. 7288–7293, 2011.
arXiv:1102.2959 (2011).

[204] R. Piazza, S. Buzzaccaro, and E. Secchi, "The unbearable heaviness of colloids: facts, surprises, and puzzles in sedimentation," *J Phys.: Condens Matter*, vol. 24, p. 284109, 2012.

[205] S. Buzzaccaro, R. Rusconi, and R. Piazza, ""sticky" hard spheres: Equation of state, phase diagram, and metastable gels," *Phys. Rev. Lett.*, vol. 99, p. 098301, 2007.

[206] M. Leocmach, R. C. P., and H. Tanaka, "Novel zone formation due to interplay between sedimentation and phase ordering," *EuroPhys. Lett.*, vol. 89, p. 38006, 2010.

[207] P. Segre, H. E., and P. Chaikin, "Long-range correlations in sedimentation," *Phys. Rev. Lett.*, vol. 79, pp. 2574–2577, 1997.

[208] P. N. Segre, F. Liu, P. Umbanhowar, and D. A. Weitz, "An effective gravitational temperature for sedimentation," *Nature*, vol. 409, pp. 594–597, 2001.

[209] J. T. Padding and A. A. Louis, "Hydrodynamic and brownian fluctuations in sedimenting suspensions," *Phys. Rev. Lett.*, vol. 93, p. 220601, 2004.

[210] A. Wysocki, C. P. Royall, R. Winkler, G. Gompper, H. Tanaka, A. van Blaaderen, and H. Lowen, "Direct observation of hydrodynamic instabilities in driven non-uniform colloidal dispersions," *Soft Matter*, vol. 5, pp. 1340–1344, 2009.

[211] C. Wysocki, A. Rath, A. V. Ivlev, K. R. Sutterlin, H. M. Thomas, S. Khrapak, S. Zhdanov, V. E. Fortov, A. M. Lipaev, V. I. Molotkov, O. F. Petrov, H. Lowen, and G. E. Morfill, "Kinetics of fluid demixing in complex plasmas: Role of two-scale interactions," *Phy. Rev. Lett.*, vol. 105, p. 045001, 2010.

[212] H. Tanaka, "Viscoelastic model of phase separation in colloidal suspensions and emulsions," *Phys. Rev. E*, vol. 59, no. 6, p. 6842, 1999.

[213] S. Manley, H. Wyss, K. Miyazaki, J. Conrad, V. Trappe, L. Kaufman, D. Reichman, and D. Weitz, "Glasslike arrest in spinodal decomposition as a route to colloidal gelation," *Phys. Rev. Lett.*, vol. 95, p. 238302, 2005.

[214] V. Testard, L. Berthier, and W. Kob, "Influence of the glass transition on the liquid-gas spinodal decomposition," *Phys. Rev. Lett.*, vol. 106, p. 125702, 2011.

[215] P. Chaudhuri and L. Berthier, "Ultra-long-range dynamic correlations in a microscopic model for aging gels," *ArXiV*, p. 1605.09770, 2016.

[216] C. Likos, M. Schmidt, H. Löwen, M. Ballauff, D. Pötschke, and P. Lindner, "Soft interaction between dissolved flexible dendrimers: theory and experiment," *Macromolecules*, vol. 34, no. 9, pp. 2914–2920, 2001.

[217] R. Zia, B. Landrum, and W. B. Russel, "A micro-mechanical study of coarsening and rheology of colloidal gels: Cage building, cage hopping, and smoluchowski's ratchet," *J. Rheol.*, vol. 58, pp. 1121–1157, September/October 2014.

[218] A. A Coniglio, L. De Arcangelis, E. Del Gado, A. Fierro, and N. Sator, "Percolation, gelation and dynamical behaviour in colloids," *J. Phys.: Condens. Matter*, vol. 16, no. 42, p. S4831, 2004.

[219] H. Tanaka, "Importance of many-body orientational correlations in the physical description of liquids," *Faraday Discuss*, vol. 167, pp. 9–76, 2013.

[220] S. Buzzaccaro, E. Secchi, G. Brambilla, R. Piazza, and C. L., "Equilibrium concentration profiles and sedimentation kinetics of colloidal gels under gravitational stress," *J. Phys.: Condens. Matter*, vol. 24, no. 28, p. 284103, 2012.

[221] M. Schmidt, C. P. Royall, J. Dzubiella, and A. van Blaaderen, "Non-equilibrium sedimentation of colloids: Confocal microscopy and brownian dynamics simulations," *J. Phys.: Condens. Matter*, vol. 20, p. 494222, 2008.

[222] C. Perez, A. , Moncho-Jorda, R. Hidalgo-Alvarez, and H. Casanova, "A comparative study on the effect of hydrodynamic interactions in the non-sequential deposition of concentrated colloidal dispersions: stochastic rotation dynamics and brownian dynamics simulations," *Molecular Physics*, vol. 113, no. 22, pp. 2857–3597, 2015.

[223] A. Furukawa and H. Tanaka, "Key role of hydrodynamic interactions in colloidal gelation," *Phys. Rev. Lett.*, vol. 104, p. 245702, 2010.

[224] C. P. Royall, J. Eggers, A. Furukawa, and H. Tanaka, "Probing colloidal gels at multiple length scales: The role of hydrodynamics," *Phys. Rev. Lett.*, vol. 114, p. 258302, 2015.

[225] R. Harich, T. Blythe, M. Hermes, E. Zaccarelli, A. Sederman, L. F. Gladden, and W. Poon, "Gravitational collapse of depletion-induced colloidal gels," *Soft matter*, vol. 12, no. 19, pp. 4300–4308, 2016.

[226] E. Zaccarelli and Poon, "Colloidal glasses and gels: The interplay of bonding and caging," *Proc. Nat. Acad. Sci.*, vol. 106, pp. 15203–15208, 2009.

[227] E. Secchi, S. Buzzaccaro, and R. Piazza, "Time-evolution scenarios for short-range depletion gels subjected to the gravitational stress," *Soft Matter*, vol. 10, pp. 5296–5310, 2014.

[228] V. Testard, L. Berthier, and W. Kob, "Intermittent dynamics and logarithmic domain growth during the spinodal decomposition of a glass-forming liquid," *J. Chem. Phys*, vol. 140, p. 164502, 2014.
doi: 10.1063/1.4871624.

[229] L. J. Teece, M. A. Faers, and P. Bartlett, "Ageing and collapse in gels with long-range attractions," *Soft Matter*, vol. 7, pp. 1341–1351, 2011.

[230] P. G. de Gennes, *Scaling Concepts in Polymer Physics*.
Cornell University Press, Ithaca and London, 1979.

[231] A. Alsayed, Z. Dogic, and A. Yodh, "Melting of lamellar phases in temperature sensitive colloid-polymer suspensions," *Phys. Rev. Lett.*, vol. 93, p. 057801, 2004.

[232] B. Vincent, "The calculation of depletion layer thickness as a function of bulk polymer concentration.," *Colloids and Surfaces*, vol. 50, pp. 241–249, 1990.

[233] M. E. Schimpf and J. C. Giddings, "Characterization of thermal diffusion in polymer solutions by thermal field-flow fractionation: effects of molecular weight and branching," *Macromolecules*, vol. 20, pp. 1561–1563, 07 1987.

[234] B. Peng, E. van der Wee, A. Imhof, and A. van Blaaderen, "Synthesis of monodisperse, highly cross-linked, fluorescent pmma particles by dispersion polymerization," *Langmuir*, vol. 28, pp. 6776–6785, 05 2012.

[235] F. D., "The tetrahedral dice are cast ... and pack densely," *Physics*, vol. 3, no. 37, 2010.

[236] E. Chen, "A dense packing of regular tetrahedra.," *Discrete Comput. Geom.*, vol. 40, pp. 214–240, 2008.

[237] A. Jaoshvili, A. Esakia, M. Massimo, Porrati, and P. M. Chaikin, "Experiments on the random packing of tetrahedral dice," *Phys Rev. Lett.*, vol. 104, no. 185501, 2010.